Theses and Dissertations

2011

Back-scattering Interferometry: A robust tool for the analysis of intermolecular interactions

Esther Pesciotta
Lehigh University

Follow this and additional works at: http://preserve.lehigh.edu/etd

Back-scattering Interferometry:

A robust tool for the analysis of intermolecular interactions

by

Esther N. Pesciotta

A Dissertation

Presented to the Graduate and Research Committee

of Lehigh University

in Candidacy for the Degree of

Doctor of Philosophy

in

Chemistry

Lehigh University

March 31, 2011

Approved and recommended for acceptance as a dissertation in partial fulfillment of the requirements for the degree of Doctor of Philosophy.

"Back-scattering Interferometry: A robust tool for the analysis of intermolecular interactions"

Esther N. Pesciotta

_____March 31, 2011_____

Defense Date

_____

Robert A. Flowers II, Ph. D.

Dissertation Director

_____

Accepted Date

Committee Members

_____

Kerney J. Glover, Ph. D.

_____

Dmitri Vezenov, Ph. D.

_____

Lynne Cassimeris, Ph. D.

for their insightful discussions and camaraderie. My sincere appreciation goes to Brian, Jimmy, and Rajni for all of their helpful suggestions in writing this dissertation. Extra thanks goes to Rajni, for keeping my sanity in check during my graduate studies and for the many deep conversations and good laughs. I could not imagine graduate school without you. I would also like to extend my thanks to all of the faculty and staff in the Department of Chemistry at Lehigh University and all of my teachers and professors who have taught and encouraged me to pursue higher education in chemistry.

Finally, I would like to thank those whom I could always count on for emotional support and guidance- my friends and family. To my dear friends Alex Milspaw, Becca Simone, Bonnie Belvin, Erin Schwartz, and Lindsay Bonanno thanks for providing me with some great distractions and always lending an ear when I needed it. To my parents, Mary & Gregg Pesciotta, I am so thankful for all of your love, encouragement, and all of the hard work you put in to raise and support me. To my siblings, Shana, Josh, Regina, Joe, and Beatrice, you all are the best; I can always count on you guys to put a smile on my face. Grandma Trudy Maran, you have been a major source of inspiration for me, thanks for always being there to cheer me on. I would like to express my utmost gratitude to my husband, Doug Miller. You have been here for me through all of this: the years of never-ending studying, countless hours spent traveling to see me, and sitting through numerous practice talks. Your love and devotion mean so much to me. Lastly, thanks to God for His strength and guidance; at times when I did not know where I was going he helped show me the way.

Table of Contents

List of Tables

List of Figures

List of Abbreviations

BSI	Back-scattering interferometry
CaM	Calmodulin
CaN	Calcineurin
CCD	Charge-coupled device
CD	Circular dichroism
Cy3	Cyanine-3
DL	Detection Limit
DLS	Dynamic light scattering
DMSO	Dimethyl sulfoxide
DNPTU	1,3-bis(p-nitrophenyl)thiourea
DNPU	1,3-bis(p-nitrophenyl)urea
DPTU	1,3-diphenylthiourea
DPU	1,3- diphenyl urea
dsDNA	Double–stranded DNA
DSP	Digital signal processing
FFT	Fast Fourier transform
FITC	Fluorescein isothiocyanate
GMBS	N-(γ-maleimidobutyryloxy)succinimide ester
HeNe	Helium Neon
HEPES	4-(2-hydroxyethyl)piperazine-1-ethanesulfonic acid

ITC	Isothermal titration calorimetry
K_D	Dissociation constant
LBA	Laser beam analyzer
M13	Myosin light chain kinase peptide
MeCN	Acetonitrile
MEPTES	3-mercaptopropyltriethoxysilane
$MQ-H_2O$	Milli-Q water
PDMS	Polydimethylsiloxane
PEEK	Polyetheretherketone
P_s	Probe strand
R_h	Hydrodynamic radii
RI	Refractive index
SNP	Single nucleotide polymorphism
SPR	Surface plasmon resonance
ssDNA	Single-stranded DNA
Tfp	Trifluoperazine-dihydrochloride
T_m	Melting temperature
TMAB	Tetramethylammonium benzoate
TMAS	Tetramethylammonium p-toluene sulfonate
UV	Ultraviolet
VASE	Variable angle spectroscopic ellipsometer

List of Chapter Annotations

Chapter 2: Benchmarking BSI through analysis of Calmodulin-ligand interactions

- ITC experiments were carried out by E. N. Pesciotta and BSI experiments were performed by collaborators in Dr. Darryl Bornhop's group at Vanderbilt University.

Chapter 3: Comparison of free-solution versus surface-immobilized oligonucleotide hybridization using BSI

- **E. N. Pesciotta**, D. J. Bornhop, R. A. Flowers II, "Back-scattering interferometry: A versatile platform for the study of free-solution vs. surface-immobilized hybridization" *Chemistry-an Asian Journal*, 6, 70-73, (2011).

- D. J. Bornhop, R. A Flowers II, **E. N. Pesciotta** "Methods, systems, and compositions for DNA analysis and sequence mismatch detection using back-scattering interferometry", U.S. Patent Application No. 61392890, October 2010.

Chapter 4: A novel approach to the study of small molecule, hydrogen-bonding interactions using BSI

- **E. N. Pesciotta**, D. J. Bornhop, R. A. Flowers II, "Back-scattering interferometry: an alternative approach for the study of hydrogen bonding interactions in organic solvents" *Organic Letters,* manuscript in press.

Abstract

Scientists are constantly working to improve analytical instrumentation in order to quantify intermolecular interactions in a fast, reliable, inexpensive, and physiologically relevant manner. Current techniques utilize a variety of detection schemes including fluorescence-based assays, surface-interrogating methodologies, and intrinsic changes such as heat transfer or refractive index shifts.[1] This dissertation focuses on the latter, using the back-scattering interferometer (BSI) to analyze a wide variety of interactions ranging from biomolecules to small organic compounds. During a typical BSI experiment, the introduction of two binding partners creates a change in refractive index, causing a spatial shift in the fringe pattern with respect to the reference. The magnitude of this shift depends on the precise fringes analyzed, the concentration of the binding partners, conformational changes initiated upon binding, changes in solvation, and binding affinity.[2-4] The work described in this dissertation utilizes BSI for the steady-state analysis of protein interactions, oligonucleotide hybridization, and hydrogen bonding of small organic molecules in non-aqueous solvents.

Initial experiments employed isothermal titration calorimetry (ITC) to benchmark BSI. The interactions of calmodulin (CaM) with Ca^{2+}, a small drug molecule, trifluoperazine dihydrochloride (Tfp), M13 peptide, and calcinuerin (CaN) were investigated to determine the advantages and disadvantages of each approach. Experiments carried out with calmodulin binding to Ca^{2+} and Tfp show a clear advantage for ITC, in that it provides the stoichiometry and a complete thermodynamic profile for the interaction. On the other hand, BSI proves to be a superior technique for studying the

interaction of CaM with an M13 peptide and CaN, highlighting the importance of studying such interactions at low concentrations. The high concentrations required to generate sufficient heat for the ITC experiments resulted in peptide aggregates that lead to erroneous thermodynamic data.

Next, oligonucleotide hybridization experiments were designed to analyze the impact of fluorophore-attachment, mismatched base pairs, and surface-immobilization on duplex formation. Interestingly, the addition of a Cy3 or FITC probe onto the 5' end of the oligonucleotide slightly stabilized the duplex as seen by ITC, BSI, and temperature melting studies. The influence of a terminal two-base-pair mismatch was modest whereas the internal mismatch significantly destabilized the duplex. The detection of mismatch base pairs, specifically single nucleotide polymorphisms, are critical in biochemical and medical research. Therefore, the ability of BSI to detect mismatch base pairs provides an alternative method for the detection of genetic mutations. For the first time, a direct comparison of surface-immobilized and free-solution methodologies was carried out using the same sensing platform. Results from these hybridization experiments show a clear perturbation due to immobilization, with K_D values nearly 50% higher than free-solution experiments. While the K_D values for the surface-immobilized experiments were higher than free-solution, both data sets exhibited the same trends.[5]

Finally, the hydrogen bonding of small molecules was investigated using BSI with acetonitrile as the solvent. In organic chemistry, hydrogen bonding partners have been utilized as the basis for approaches used to drive crystal formation, molecular recognition and catalysis.[6] Given the synthetic effort required to produce the components for the study of systems that utilize hydrogen bonds for recognition and catalysis, it is

desirable to be able to study interactions using small quantities of substrates. Up to this point, BSI has only been used to study interactions in aqueous media. To determine if this technique can be extended to studies in organic solvents, we examined the complexation of tetramethylammonium benzoate (TMAB) with 1,3-diphenyl urea (DPU), 1,3-diphenylthiourea (DPTU), 1,3-bis(p-nitrophenyl)urea (DNPU), and 1,3-bis(p-nitrophenyl)thiourea (DNPTU) in MeCN. Results from this study show that BSI is able to recognize the formation of just two hydrogen bonds and distinguish between TMAB complexation with DPU/DPTU and DNPU/DNPTU with an affinity difference of more than one order of magnitude. These experiments helped to elucidate the lower limits of BSI as an analytical tool for screening small molecule interactions.

The key features of BSI that make it appealing for the study of intermolecular interactions are small sample sizes (pL to μL range), low concentrations (nM to μM), and the ability to carry out experiments without pre-functionalization or surface immobilization of one of the binding partners. The change in refractive index that occurs when two molecules interact is an intrinsic characteristic that can arise from changes in molecular structure,[7] dipole moment, polarizability,[8] conformation, and solvation state.[9] The studies discussed herein exemplify the straightforward, user-friendly design of BSI to examine a wide variety of interactions.

References

(1) Ince, R.; Narayanaswamy, R. *Analytica Chimica Acta* **2006**, *569*, 1-20.

(2) Bornhop, D. J.; Latham, J. C.; Kussrow, A.; Markov, D. A.; Jones, R. D.; Sorensen, H. S. *Science* **2007**, *317*, 1732-1736.

(3) Kussrow, A.; Kaltgrad, E.; Wolfenden, M. L.; Cloninger, M. J.; Finn, M. G.; Bornhop, D. J. *Anal. Chem.* **2009**, *81*, 4889-4897.

(4) Latham, J. C.; Stein, R. A.; Bornhop, D. J.; McHaourab, H. S. *Anal. Chem.* **2009**, *81*, 1865-1871.

(5) Pesciotta, E. N.; Bornhop, D. J.; Flowers, R. A., II *Chem. Asian J.* **2011**, *6*, 70-73.

(6) Hunter, C. A. *Angew. Chem. Int. Ed Engl.* **2004**, *43*, 5310-5324.

(7) Elkashef, H. *Opt. Mater.* **1997**, *8*, 175-183.

(8) Maroulis, G.; Xenides, D.; Hohm, U.; Loose, A. *J. Chem. Phys.* **2001**, *115*, 7957-7967.

(9) Sota, H.; Hasegawa, Y.; Iwakura, M. *Anal. Chem.* **1998**, *70*, 2019-2024.

Chapter 1

Introduction

Intermolecular interactions are at the heart of chemistry. From the simplest form of interacting molecules, hydrogen bonds in water, to the more complex associations of proteins and DNA, these binding events form the basis of life. Furthermore, the conformational structure and stability of biomolecules are governed by intra- and intermolecular interactions.

When two molecules interact there are several driving forces including electrostatic, London dispersion, hydrogen bonding, and hydrophobic.[1] Electrostatic forces vary in strength from strong ionic interactions, moderate ion-dipole (10-50 kJ/mol), and weak dipole-dipole interactions (3-4 kJ/mol). London dispersion forces occur between nonpolar molecules and arise from transient dipole moments. Although dispersion forces are weak (1-10 kJ/mol), numerous interactions can have a cumulative effect on a structure.[2] Hydrogen bonding between electropositive hydrogen atoms and electronegative O and N are strong (5-40 kJ/mol). Hydrogen bonding plays a huge role in biomolecular interactions. Hydrophobic interactions can be equally important in biochemical systems. Hydrophobic interactions occur between nonpolar molecules and involve the exclusion of polar molecules. All of these forces act separately or in concert to influence how small molecules, large macromolecules, and biomolecules interact with one another.

Not only are these interactions critical for sustaining life but the relative strength of these interactions are vital. For example, cyanide is lethal because it has a higher

binding affinity for hemoglobin than oxygen and carbon dioxide, quickly leading to asphyxiation. Additionally, the quantification of binding events is crucial for understanding cellular processes in biological systems and of utmost importance in diagnostics and drug development. The study of intermolecular interactions is continuously progressing as instrumentation improves and expands.

1.1 Current approaches to the study of intermolecular interactions

Current analytical methods used to study intermolecular interactions fall into three general categories: fluorescence-based, surface-immobilized, and free-solution. These categories are based on the method of signal generation. Fluorescence-based assays typically require a fluorescently labeled probe that provides the signal for emission or quenching, which is then used to study binding interactions. These types of assays are advantageous because they are relatively simple, have low detection limits, are highly specific, and can be used to simultaneously analyze multiple analytes.[3] However, these assays can have time-consuming and expensive labeling procedures. In addition, the attachment of a fluorophore can interfere with the binding mechanism.[4] Surface-immobilizing techniques require the substrate to be bound to a modified surface for signal generation. Surface plasmon resonance (SPR) is the most widely utilized surface-immobilizing technique. Additionally, diffraction, interferometry, wave guiding, nanowire sensing, and microcantilever sensing have been utilized.[4] These techniques are useful because they are label-free and highly sensitive, but they also require time-consuming surface preparation that can perturb binding. Unlike the previous two techniques, free-solution methodologies utilize intrinsic changes for signal generation

such as heat given off during binding (e.g. isothermal titration calorimetry, ITC) or shifts in refractive index (RI) (e.g. back-scattering interferometry, BSI). Free-solution techniques are advantageous in studying binding interactions because labels and surface-attachment are not required. However they often require high concentrations, large volumes (200 μL and higher), and provide low throughput.

In practice, researchers utilize all of these techniques to obtain a thorough understanding of different intermolecular interactions. Thus, it is important to know the strengths and limitations of the available techniques. In the age of nanotechnology, scientists are continuously working to miniaturize instrumental analysis with aims of developing technology that is sensitive for low-volume and concentration measurements with high-throughput capabilities. This work was motivated by the need for a universal technique that is relevant to nano-scale chemistry but does not require fluorescence or surface tethering for signal generation. The following two sections in this chapter will provide background on a widely used and accepted technique (ITC) as well as a recently developed microfluidic device (BSI).[5]

1.2 Isothermal Titration Calorimetry (ITC)

1.2.1 Background of ITC

ITC is a thermodynamic technique that measures the heat evolved or absorbed between a sample and reference cell during the mixing of two substances by titration. This method is often used to analyze biochemical interactions because a single experiment can provide a complete thermodynamic profile consisting of the reaction stoichiometry (n), binding constant of association (K_a), change in enthalpy (ΔH), and

change in entropy (ΔS).[6] These thermodynamic data provide insight into the driving force of an interaction. The stoichiometry of an interaction characterizes the relationship between the analyte and ligand, assigning the number of binding or active sites. K_a describes the affinity of the interaction at equilibrium, to quantify the strength of a binding interaction. ΔH provides the enthalpy of a system and reveals whether an interaction is exothermic or endothermic. ΔS describes the amount of disorder present in the system, with a positive ΔS indicating an increase in disorder. During an intermolecular binding event, a positive entropy value often indicates the displacement of solvent, causing an increase in disorder. Taken together, ΔH and ΔS determine whether or not an interaction is spontaneous and energetically favorable, defined by Gibbs free energy (ΔG) (eqn 1).

$$\Delta G = \Delta H - T\Delta S \tag{1}$$

The evolution of heat during an interaction is an intrinsic property of the system of interest. ITC is advantageous because it does not require chemical modification or immobilization to a solid support to generate the binding signal. In the past two decades ITC has revolutionized the study of intermolecular interactions. While originally developed to study biochemical interactions,[6, 7] today other applications have been developed for small molecule (drug) binding,[8] protein folding,[9] interactions with metals,[10] solvation,[11] and thermodynamic parameters of structural details.[12] With all of these applications and breadth of information provided by an ITC experiment, ITC has become an essential technique to the scientific community.[13]

1.2.2 ITC Experimentation & Analysis

The macromolecule-containing sample cell of the calorimeter is kept at a constant temperature while precise volumes of the ligand are injected from a stirring syringe (Fig. 1.1). Each ligand injection generates a change in temperature that is monitored by comparison to a reference cell. A thermostat is used to return the sample cell to its initial temperature prior to the next injection. Injections are continued until all ligand is bound by the macromolecule and only the heat of dilution is observed.[14] These data are integrated to obtain the area (µcal) under each peak and plotted with kcal/mole of ligand versus the molar ratio of the ligand/macromolecule to create a binding curve (Fig. 1.2). After a successful experiment, the ligand is injected into pure buffer to obtain a heat of dilution which is subtracted from the binding isotherm to obtain the final plot. The final plot is fit using software (i.e. Origin®) to obtain n, K_a, and ΔH. ΔS is calculated from the obtained values of K_a, and ΔH using Gibbs free energy relationship (eqn 2):

$$\Delta G^{\circ} = \Delta H^{\circ} - T\Delta S^{\circ} = -RTlnK_a \tag{2}$$

where R is the ideal gas constant and T is the temperature. The nature of the interaction can be approximated as one-site, multiple-sites, cooperative, or dissociative binding models.[6, 14] All the ITC experiments discussed within this dissertation involve either the one-site or multiple-sites binding models.
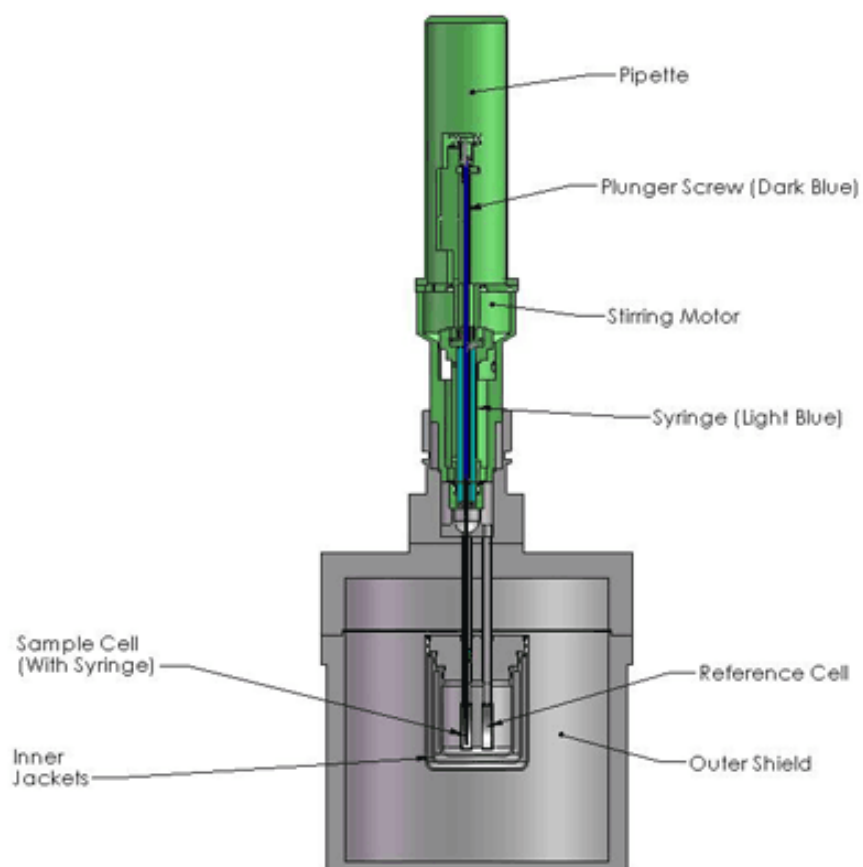
Figure 1.1 Diagram of ITC setup showing the key components of the instrument including the pipette, injection syringe, sample cell, reference cell, and thermostat.[14]
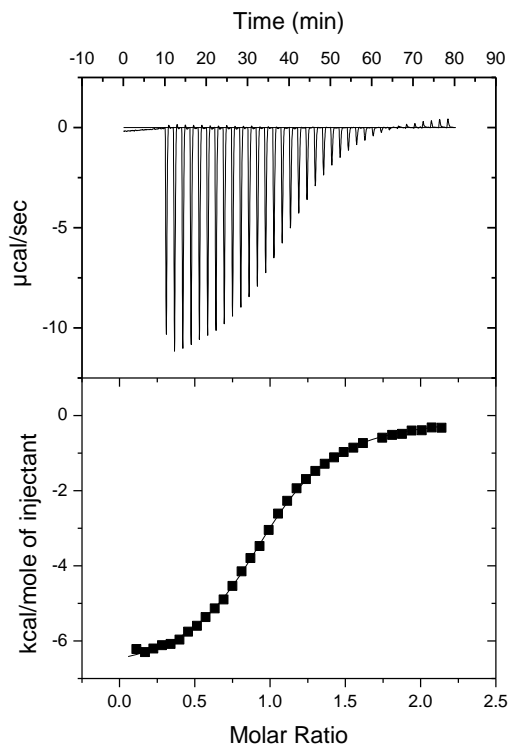
Figure 1.2 Representative ITC data showing 35 ligand injections. The area under each injection spike is equal to the amount of heat released during that injection. This isotherm clearly shows binding saturation with a stoichiometry of ~ 1.

There are several important factors necessary for carrying out a successful ITC experiment. First of all, the concentration of both analytes must be high enough to generate measurable thermal changes and reach saturation that occurs when all of the binding sites of the analyte are occupied by the ligand. An appropriate concentration is estimated by equation 3,

$$K_a * C = 10\text{-}50 \tag{3}$$

Where K_a is the association constant and C is the concentration of the analyte in the sample cell. The concentration of the titrant is then estimated using equation 4.

$$c = 7 * n * C \tag{4}$$

11

Where c is the concentration of the ligand in the syringe and n is the expected stoichiometry of the interaction. If K_a of the interaction is unknown, the appropriate concentrations must be determined experimentally by trying various concentrations.

Another important factor for a successful ITC experiment is matched buffers or solvents. Since ITC relies on thermal changes, it is crucial that the signal is generated only from the binding interaction and heat of dilution. Many biological systems involve large macromolecules with ionizable side-chains that can participate in hydrogen transfers resulting in small pH changes. Slight variations in pH between the sample cell and syringe can significantly alter the ITC data and interfere with the results. It is often necessary to dialyze samples prior to the experiment to ensure perfectly matched buffers.

The remaining experimental parameters that need to be considered include the experimental temperature, injection size, and reference power. Typically, the temperature is maintained at 25 ºC but can vary depending on the experiment. The injection size can also range between 3-10 µL depending on the concentration range and the number of injections. Ideally, the ITC experiment is carried out so that there are several data points in the binding region of the isotherm. However, this is often difficult to achieve for high affinity interactions in which the transition occurs over a small range. Subsequently, there is a balance between keeping the injection size and concentration range as small as possible while still detecting measurable binding events. The reference power is the power supplied to the reference cell used to keep the temperature constant throughout the experiment. This value is entered into the program prior to the experiment, ranging from 0-91.8 µCal/sec. The reference power can be set high or low depending on whether the interaction is endo- or exothermic. A highly exothermic

interaction requires a high reference power (~ 30 μCal/sec), whereas an endothermic interaction needs a lower reference power (~2 μCal/sec).[14]

1.3 Back-scattering Interferometry (BSI)

1.3.1 Background of Interferometry

Interferometry relies on constructive and destructive interference of waves to extract spectral information.[15] The constructive and destructive interference of a wave depends on the frequency, amplitude, and phase (Fig. 1.3). Figure 1.4 provides a visual representation of interference that occurs between waves when they are added together. Constructive interference occurs when two waves of the same frequency, amplitude, and phase combine to create a wave with the same frequency and phase but with double the amplitude. Destructive interference occurs from the addition of two waves with the same frequency and amplitude but with opposite phases, which cancels out the two signals.[16]
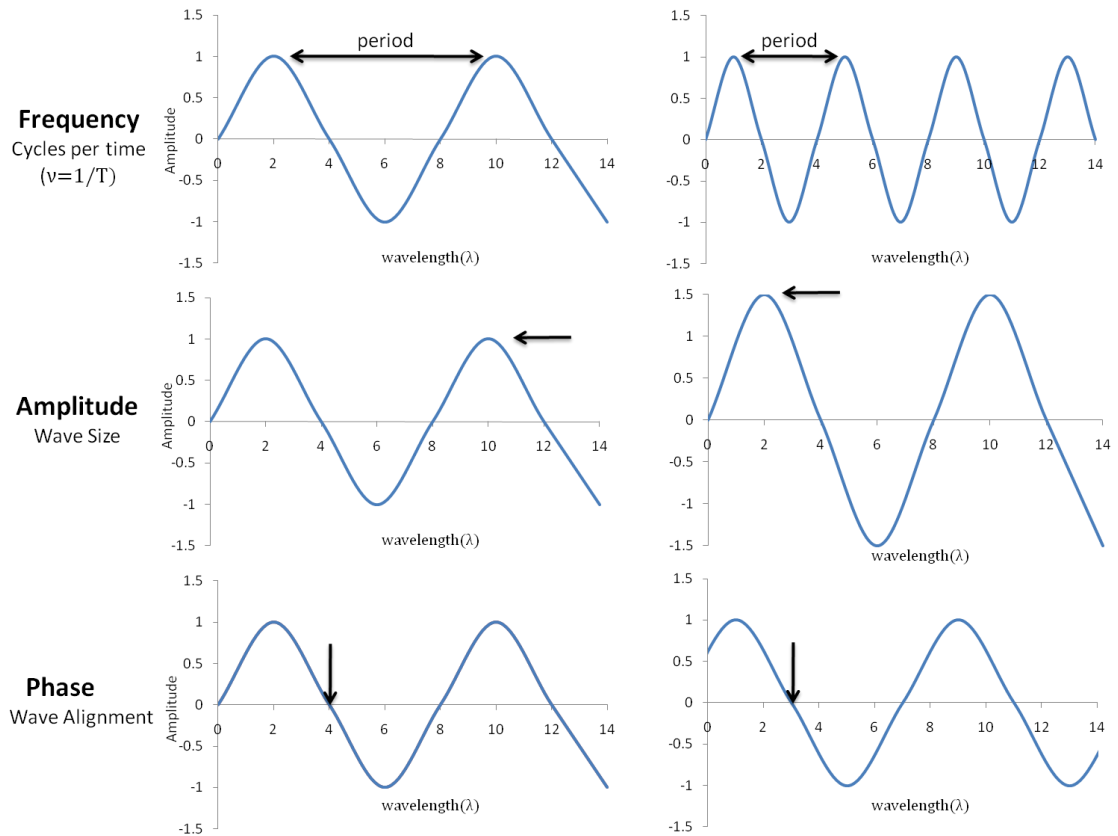
Figure 1.3 Characteristics of a wave including frequency, amplitude, and phase.
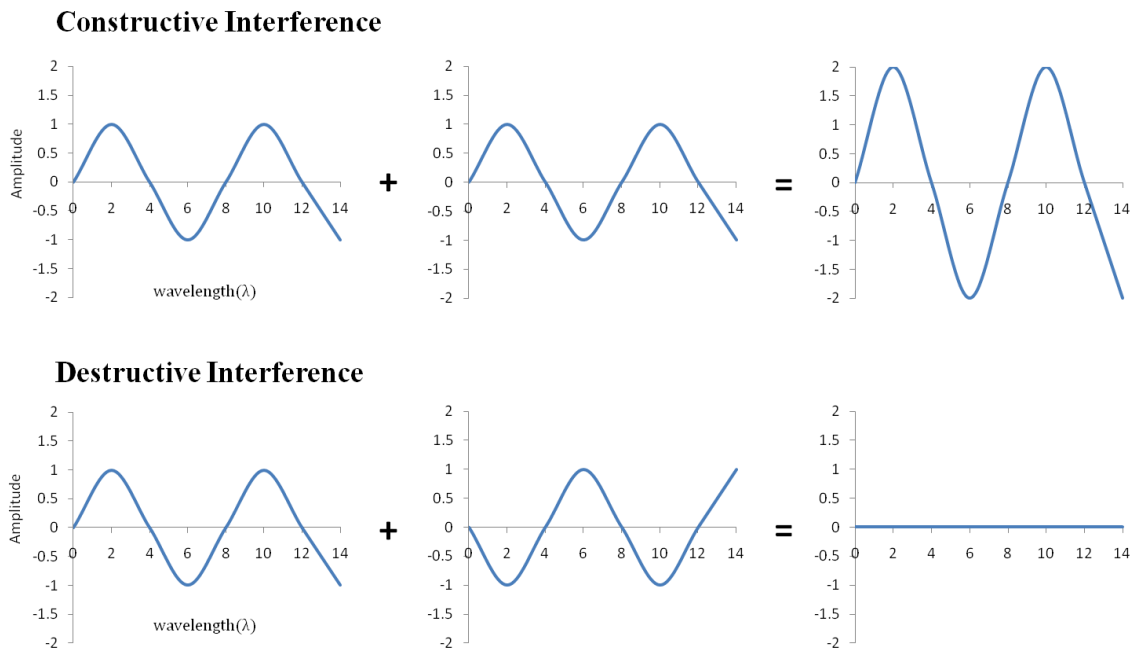
Figure 1.4 Constructive and destructive interference.

14

One of the first interferometers originated from Young's double slit experiment in the 1800's.[17] Young found that the diffraction of light through two pin holes in a screen formed an interference fringe pattern (Fig. 1.5).   This classic experiment not only characterized light as a wave but also provided the basis for optical interference. While Young's experiment required the diffraction of light to produce an interferogram, a similar effect can be obtained by the refraction of light that occurs when light passes through media with different RI.

$$\eta = \frac{c}{v} = \sqrt{\frac{\varepsilon\mu}{\varepsilon_0\mu_0}} \tag{5}$$

The absolute index of refraction (η) is the ratio of the speed to light in a vacuum (c) to the speed of light within a substance (v) which is directly related to the electric permittivity (ε) and permeability (μ) of that media relative to the permittivity (ε_0) and permeability (μ_0) in a vacuum (eqn 5).[18]

$$K_d = \frac{\varepsilon}{\varepsilon_0} \tag{6}$$

The dielectric constant of a medium (K_d) relates the electric permittivity of a medium (ε) to that of a vacuum (ε_0) (eqn 6).

$$K_m = \frac{\mu}{\mu_0} \tag{7}$$

Additionally, the relative permeability of a substance (K_m) is related to that of free space by equation 7. Therefore the index of refraction is directly linked to K_d and K_m (eqn 8).

$$\eta = \sqrt{K_d K_m} \tag{8}$$
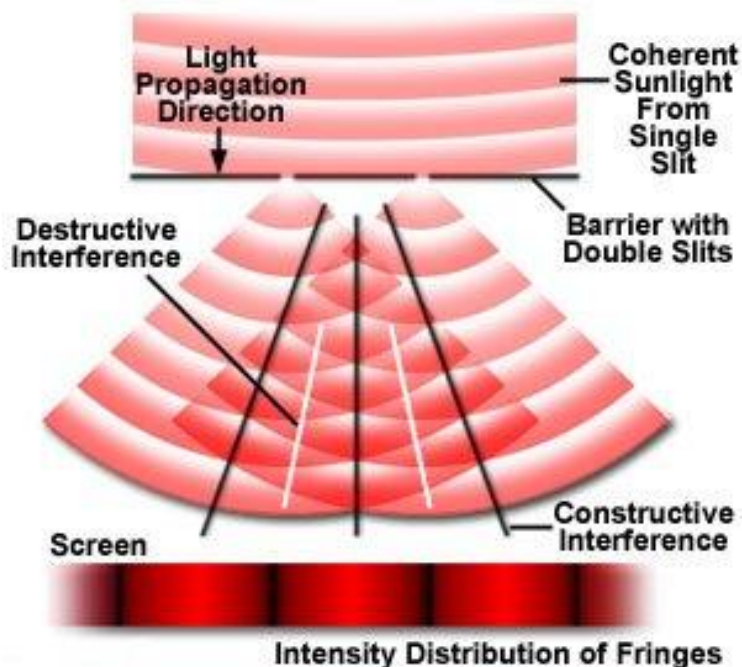
Figure 1.5 Young's double slit experiment.[19]

Today, researchers still use variations of Young's double slit interferometer to measure RI changes in N_2 and CO_2 gases[20] and glucose solutions[21] with a resolution of 10^{-5} and 10^{-7}, respectively. Another analytical tool based on the Young interferometer is the Farfield sensor, which provides a sensing and reference path by splitting the light source into two waveguides instead of using two slits (Fig 1.6). In this dual polarization interferometer, analytes are immobilized onto the sensor, subsequently modifying the RI and altering the interference pattern.[22] The Mach-Zehnder interferometer is similar to the Farfield sensor but uses a beam splitter and mirrors to direct the light beam to a sample and reference path.[23]   This concept was modified to include a chip with microfluidic channels to detect and monitor binding interactions[24].   In this proof of concept experiment, biotin was immobilized to the channel surface while its binding partner,

streptavidin, was injected into the system. The binding of streptavidin increases the thickness of the surface, inducing a phase change in the interference pattern to detect molecular association. There is an extensive list of interferometers used by scientists in the past decade for biosensing. These instruments include spinning disc,[25, 26] waveguide,[27] and photonic crystal waveguide.[28]
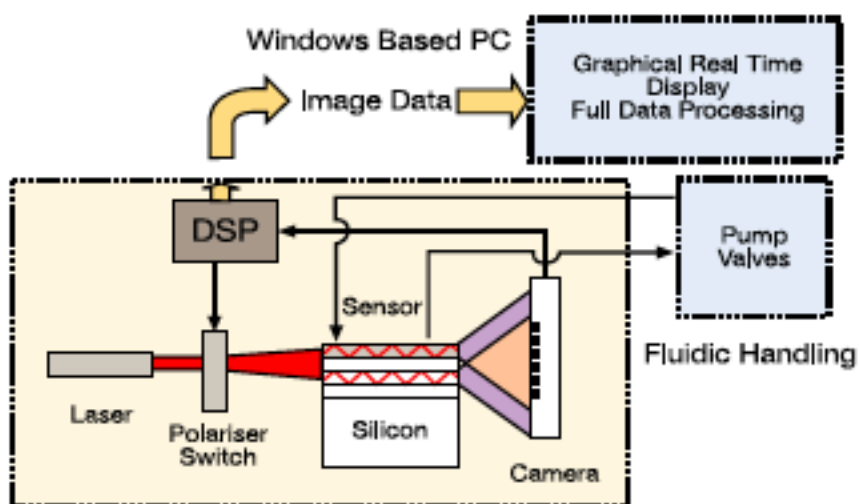
Figure 1.6 Schematic of the Farfield dual polarization interferometer, where DSP stands for digital signal processing.[29]

1.3.2 Overview of BSI

Back-scattering interferometry is a technique that monitors a change in RI to detect molecular interactions by impinging monochromatic light directly onto a microfluidic channel. The underlying principle behind BSI is the detection of a change in RI that occurs when two molecules interact.[30] This shift in RI is a result of changes in molecular structure,[31] dipole moment, polarizability,[32] conformation, and solvation [33] that occur during an interaction through the formation of new species. Thus BSI can be used

detect a wide array of interactions because it can measure the small changes in RI that occur when species bind.

Figure 1.7 depicts the general schematic of BSI with a fiber-coupled helium neon (HeNe) laser focused onto the channel to generate an interference fringe pattern. The fringe pattern arises due to the refraction of light traveling through the glass walls of the channel ($\eta_D = 1.52$) and then into solvent with a different RI (eg. $\eta_{D(MeCN)} = 1.34$).[34] The change in RI results in the separation of the original light source into two separate beams which recombine constructively or destructively to create an interference fringe pattern. The fringe pattern is scattered backwards into a mirror that is angled to direct the light into a high-resolution linear charge-coupled device (CCD) detector. A neutral density filter is necessary to protect the CCD camera from over exposure by reducing the laser intensity.

Fringe Pattern in MeCN

Mirror

CCD Array

Neutral Density Filter

HeNe Laser

Microfludic Glass Chip on Temperature-Controlled Stage
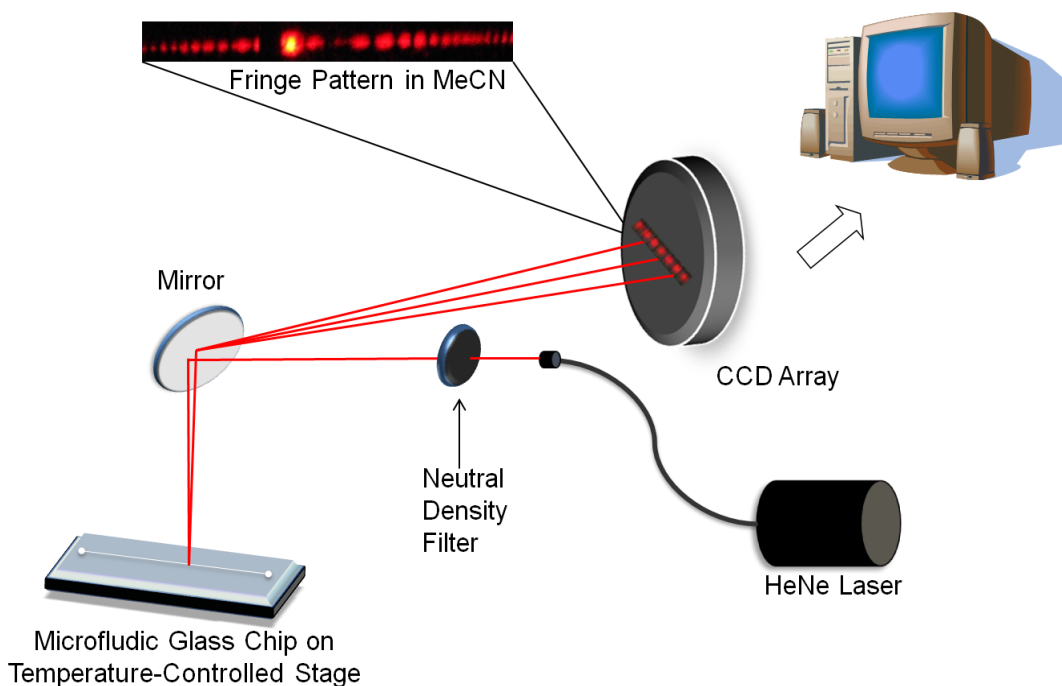
Figure 1.7 Schematic of BSI with representative fringe pattern in acetonitrile (MeCN).

1.3.3 Data Acquisition

Several detection platforms were previously investigated including a bicell,[35] slit-photodetector with a reference,[36] a CCD connected to a laser beam analyzer (LBA),[37] a CCD array with minimum tracking, and a CCD array with Fourier transform phase detection.[38] These methods were analyzed and ranked according to their detection limits, ranging from $5x10^{-5}$ to $7x10^{-8}$ RI units. The most sensitive of all of the detection methods was detection with a CCD array and fast Fourier transform (FFT) analysis with the lowest detection limit of $7x10^{-8}$ RIU. The other techniques were inadequate because they were only able to analyze a single fringe.[38]

Once detected by the CCD camera, the fringe pattern is analyzed by utilizing a FFT to deconvolute the data and speed up data acquisition. The FFT method requires a sigmoidal fringe curve to generate a single frequency function as seen in Figure 1.8. The fringe pattern and Fourier shift depend on the species present in the channel and its concentration. This FFT method is preferred for BSI because it allows the computer to obtain real-time measurements.[39] Computer software enables proper instrument alignment by simultaneously providing images of the fringe pattern and Fourier transform. Accordingly, the chip is mounted onto translation stages for channel alignment through small, controlled movements to create a high intensity single-frequency Fourier transform that is used to obtain the specific phase corresponding to the fringe pattern.
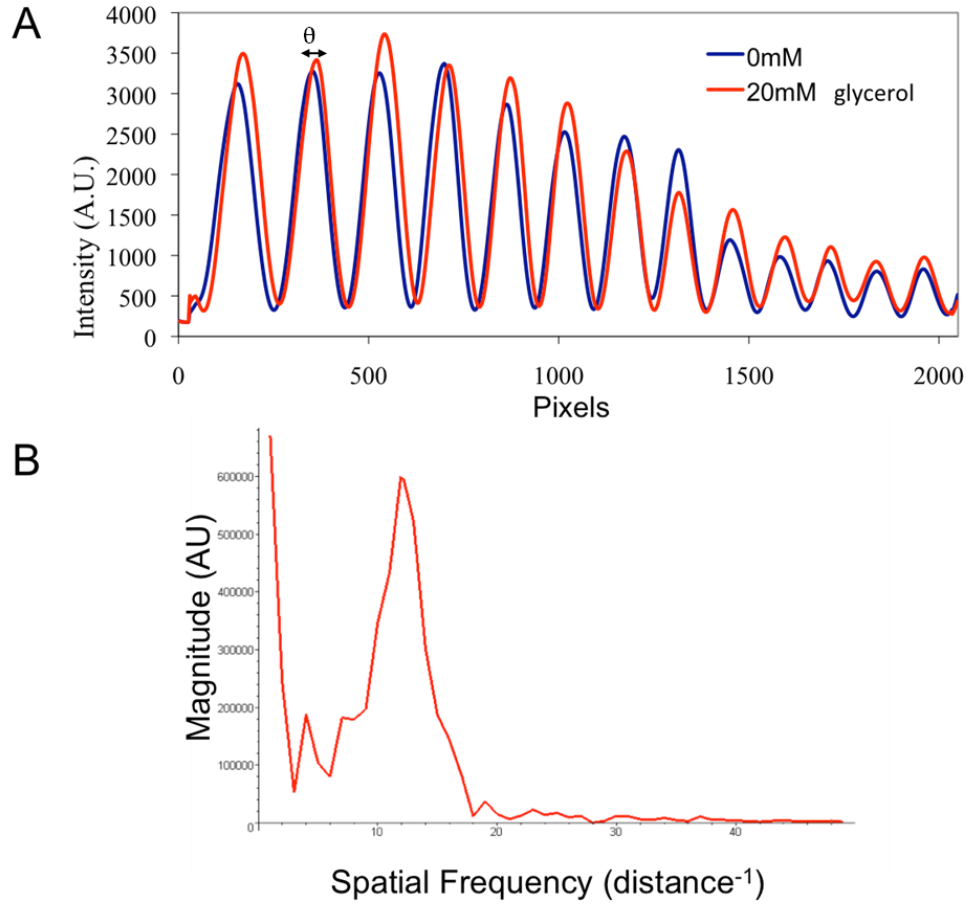
Figure 1.8 (a) Sigmoidal curve showing a fringe pattern shift from a RI change that occurs when 20 mM of glycerol is added to water. (b) Fourier transform of the fringe pattern shows a single frequency function that does not change upon addition of 20 mM glycerol. This Fourier function is used to determine the shift in phase (θ) that occurs when the RI changes. The phase reading is not shown.

1.3.4 Limit of Detection

The unique nature of the BSI setup allows for very low limits of detection due to a multi-pass configuration.[40] Figure 1.9 shows an optical ray trace model of a 100 μm channel illuminated from a curved surface with 9 initial based rays each accompanied by 8 parabasal rays. The dimensions of an etched channel contain four optical interfaces, including one curved surface, that subsequently forces the incoming rays to deviate from

their original path.[41]   Therefore, while the channel is only 100 µm wide, the effective

pathlength is much larger because the light passes through the sample multiple times

before reaching the detector.[41]   The microfluidic channel used in these BSI experiments

has a cross-sectional area of 3600 µm^2 that, when interrogated by a 100 µm diameter

laser, provides an optical probe volume of ca. 360 pL.   Therefore, the BSI configuration

allows for the detection of very small changes in RI (10^{-5} to 10^{-6} units) with only ~360 pL

of sample.
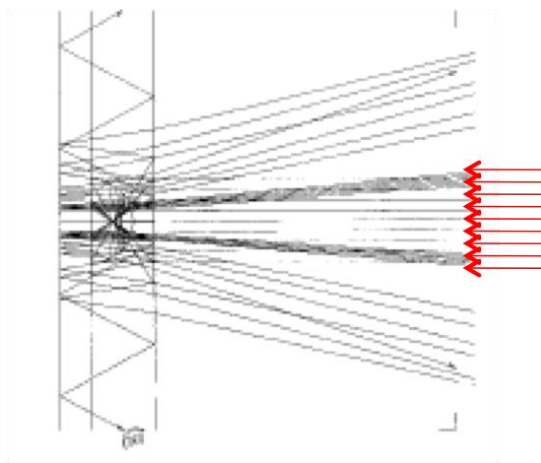
Figure 1.9 Optical ray trace model shows light passing through a fused silica channel
several times before leaving, increasing the pathlength and hence lowering the detection
limit.[41]

Determination of the detection limit (DL) of the instrument is important to

calculate the minimum detectable signal. The DL can be determined by measurements of

a control sample (i.e. glycerol) to obtain a calibration curve.[30] The calibration is carried

out by varying glycerol concentrations from 0-30 mM and plotting the change in signal

versus concentration (Fig. 1.10).   Each concentration is recorded for several trials to

ensure an accurate average and the standard deviations are used to calculate the DL. 3σ

statistics is used to ensure a 99% confidence in the DL using equation 9

$$DL_\eta = \frac{3\cdot\sigma}{|\alpha|} \cdot \frac{d\eta}{dC_{gly}} \tag{9}$$

where σ is the standard deviation, α is the slope of the calibration curve, and $d\eta/dC_{gly}$ is

the change in RI with a change in glycerol concentration[34] (0.0000106). A typical DL

for BSI as configured is on the range of low 10^{-5} to high 10^{-6} RI units.

y = -0.0054x + 1.351
R² = 0.99495
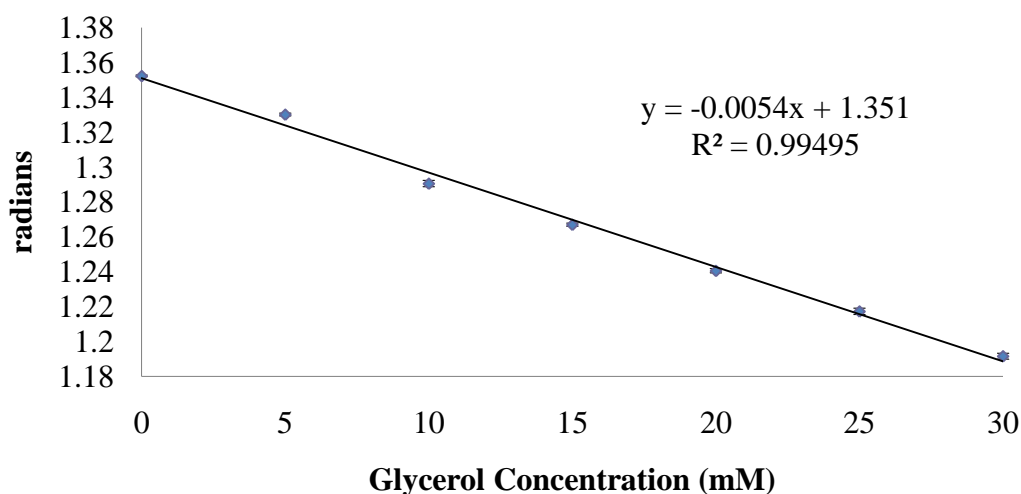
Figure 1.10 A calibration curve shows a linear response with increasing concentration of glycerol. The slope of the line is directly related to the instrument sensitivity. Standard deviation of three trials provides the noise (σ). Therefore with 3σ statistics the average detection limit is 9.07×10^{-6}.

1.3.5 Data Analysis

If a binding event occurs, the signal change is dramatic due to changes in RI

from complex formation. This technique can be used to calculate the dissociation

constant (K_D) of an analyte-ligand pair by holding the analyte at a constant concentration

and varying the concentration of the ligand. The ligand is held in excess to the analyte in

order to simplify data analysis. Depending on the experimental setup and binding pair being analyzed, the data can be obtained in a kinetic or steady-state manner.[30]

The K_D can be determined from kinetic binding curves generated in real time. For this type of experiment, a y-shaped chip is used with a serpentine mixer and a squeeze immediately following the mixer. Each substrate is simultaneously added into separate wells, and drawn into the channels with vacuum. Release of the vacuum stops the flow of the substrates so that binding can occur (Fig 1.11).

Samples mixed
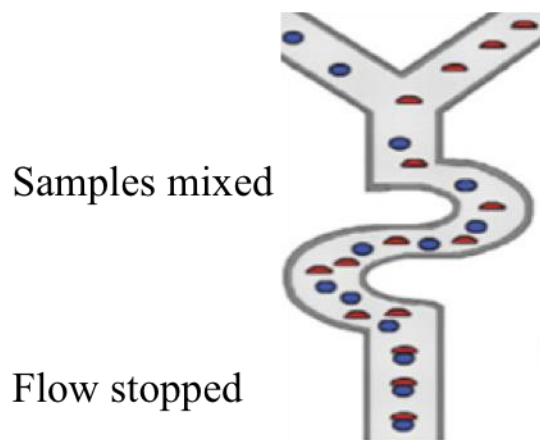
Flow stopped

Figure 1.11 Illustration of stopped-flow binding in BSI chip with serpentine mixer.[30]

For any receptor-ligand binding reaction (eqn 10) there is an association rate, k_1, and dissociation rate, k_2, with a net reaction rate shown in equation 11.

$$[R] + [L] \underset{k_2}{\overset{k_1}{\rightleftarrows}} [R \bullet L] \tag{10}$$

$$\frac{d[R \bullet L]}{dt} = -k_2 \cdot [R \bullet L]_t + k_1 \cdot [R]_t \cdot [L]_t \tag{11}$$

Where $[R]_t$, $[L]_t$, and $[R \bullet L]_t$ and are equal to the concentration of receptor and ligand and complex at a given time, t. Given the relationship in equation 10, $[R]_t$ and $[L]_t$ are related

to $[R \bullet L]_t$ and initial concentration of the receptor and ligand, $[R]_0$ and $[L]_0$, respectively (eqn 12).

$$[R]_t = [R]_0 - [R \bullet L]_t \quad \& \quad [L]_t = [L]_0 - [R \bullet L]_t \tag{12}$$

Therefore, equation 11 can be re-written as follows:

$$\frac{d[R \bullet L]}{dt} = -k_2 \cdot [R \bullet L]_t + k_1 \cdot \{[R]_0 - [R \bullet L]_t\} \cdot \{[L]_0 - [R \bullet L]_t\} \tag{13}$$

In order to find a solution to equation 13, $[L]_0 \gg [R \bullet L]_t$ so that the ligand concentration is essentially constant throughout the reaction. As a result, $[L]_t = \{[L]_0 - [R \bullet L]_t\} \approx [L]_0$ and equation 13 is simplified to equation 14.

$$\frac{d[R \bullet L]}{dt} + (k_1 \cdot [L]_0 + k_2) \cdot [R \bullet L]_t = k_1 \cdot [R]_0 \cdot [L]_0 \tag{14}$$

Equation 14 represents an ordinary differential equation that can be re-written as

$$f'(t) + A \cdot f(t) = B \tag{15}$$

where $A = k_1 \cdot [L]_0 + k_2$ and $B = k_1 \cdot [R]_0 \cdot [L]_0$. This simplified equation can be rearranged and integrated to yield the following:

$$\ln(f) = -A \cdot t + C \Rightarrow f(t) = C \cdot e^{-A \cdot t} \tag{16}$$

where C is an arbitrary constant. A solution to this function exists at equilibrium ($t = \infty$) where the complex has reached its maximum state ($[R \bullet L]_{eq} = [R \bullet L]_\infty = [R \bullet L]_{max}$). Therefore, the net reaction rate is zero and $f'(\infty) = 0$. Inserting this solution into equation 15 shows that $f(\infty) = B/A$ to yield the general equation (eqn 17).

24

$$f(t) = C \cdot e^{-A \cdot t} + \frac{B}{A} \tag{17}$$

Finally, at the initial starting point ($t = 0$), no complex exists so that $[R \bullet L]_0 = 0 = f(0)$ and

since $e^0 = 1$, $C = -B/A$ and equation 17 can be rewritten

$$f(t) = \frac{B}{A}(1 - e^{-A \cdot t}) \tag{18}$$

By inserting the original values for A and B into equation 18, this function becomes:

$$[R \bullet L]_t = \frac{k_1 \cdot [R]_0 \cdot [L]_0}{k_1 \cdot [L]_0 + k_2} \cdot \{1 - e^{-(k \cdot [L]_0 + k_2) \cdot t}\} \qquad \text{or} \tag{19}$$

$$[R \bullet L]_t = [R \bullet L]_{max} \cdot \{1 - e^{-k_{obs} \cdot t}\}$$

where the observed rate constant, k_{obs}, is equal to $k_1 \cdot [L]_0 + k_2$. Equation 19 is in the same

form as the common exponential rise to max equation that can be used to determine k_{obs}

using routine fitting software. Plotting the k_{obs} with varied ligand concentrations yields a

linear plot (Fig 1.12) with the equation $k_{obs} = k_1 \cdot [L]_0 + k_2$. Since K_D is equal to k_2/k_1, this

method can be directly applied to determine K_D by dividing the y-intercept by the slope

of the best-fit line.
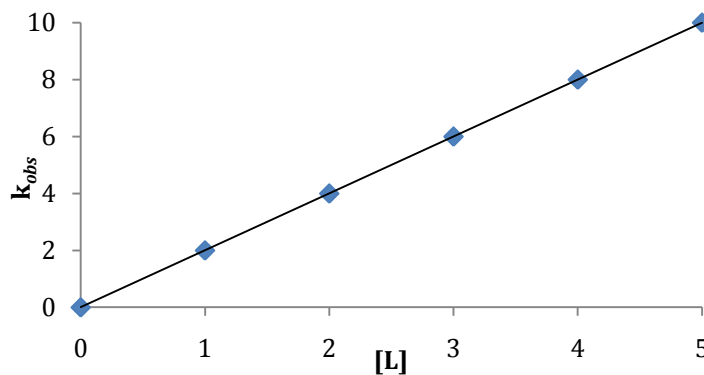
Figure 1.12 Expected linear relationship of k_{obs} versus [L] for kinetic BSI experiments.

End-point or steady-state determination of K_D is more facile than kinetic analysis because measurements are taken after the binding complex is formed. According to the law of mass action, the following is true at equilibrium:

$$[R \bullet L]_{\infty} = \frac{[R]_0 \cdot [L]_0}{[L]_0 + K_D} \qquad (20)$$

This equation can be fit using the one site binding hyperbola function to directly find K_D from a plot of signal vs. ligand concentration (Fig 1.13). The reciprocal relationship between K_a and K_D can then be used to directly compare ITC and BSI results.
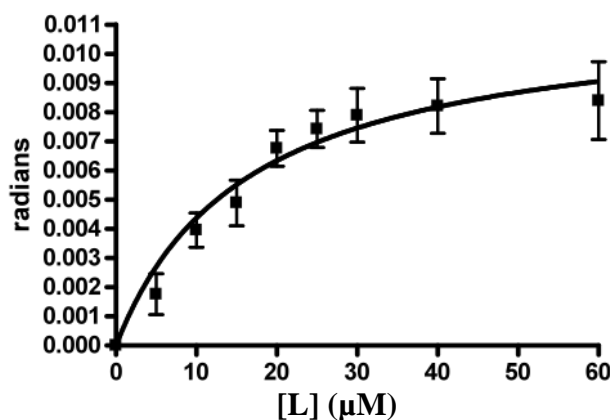
Figure 1.13 Representative binding data from steady-state BSI analysis.

26

1.4 Overview of Doctoral Research

To aid in the development and enhancement of BSI applications, several different molecular interactions were investigated and described in this dissertation. The first goal was to build the instrument in our laboratory and achieve accurate and reproducible results as described in Chapter 2. Chapter 3 describes free-solution BSI experiments, carried out with Dr. Bornhop's group at Vanderbilt University, which were benchmarked with ITC experiments (performed at Lehigh). Calmodulin (CaM), a Ca^{2+} binding protein, was chosen as the model system for benchmarking because it has a wide range of binding partners that vary greatly in affinity.[42] To examine the scope of interactions observable by BSI, CaM binding were measured with Ca^{2+} (an ion), Trifluoperazine-dihydrochloride (Tfp), (a small molecule), myosin light chain kinase peptide (M13), and the protein Calcineurin (CaN). These interactions were investigated to benchmark BSI and determine the advantages and disadvantages of each approach.

The application of BSI was then expanded to oligonucleotide hybridization. The work described in Chapter 4 contains oligonucleotide hybridization of a 30-base oligonucleotide probe strand (P_s) with a complementary strand, a complementary 5'-labeled strand tagged with either cyanine-3 (Cy3) or fluorescein isothiocyanate (FITC), a terminal CA/AC mismatch strand, and an internal AG/GT mismatch strand. BSI hybridization experiments of all five strands were carried out in both a free-solution and surface-immobilized format to directly evaluate the impact of surface tethering on duplex affinity. UV hyperchromicity melting studies were also carried out to compare BSI results with a commonly employed technique and correlate the melting temperature to the

duplex binding affinity. ITC experiments were employed to further benchmark BSI results.

The scope of BSI was expanded to interactions in non-aquoues media. Chapter 5 reports the complexation of tetramethylammonium benzoate (TMAB) with 1,3- diphenyl urea (DPU), 1,3-diphenylthiourea (DPTU), 1,3-bis(p-nitrophenyl)urea (DNPU), and 1,3-bis(p-nitrophenyl)thiourea (DNPTU) in MeCN.   Urea and thiourea have been widely studied in molecular recognition because of their ability to form strong hydrogen bonds.[43] Chapter 5 discusses the following questions: 1) Can BSI be used to study hydrogen bonding in non-aqueous media? 2) What are the limits of detection in a non-aqueous environment when the binding partners are small molecules? 3) Can BSI be used to distinguish between similar hydrogen bonding partners? In additon to carrying out BSI experiments in MeCN, ITC was used as a benchmark and variable angle spectroscopic ellipsometry was utilized to measure the RI of DPU-TMAB complexes to correlate the RI shift with BSI data.

Finally, Chapter 6 includes concluding remarks regarding the work described within this dissertation.   The ability of BSI to detect molecular interactions of biomolecules and small molecules is discussed.   Additionally the advantages and limitations of BSI are elaborated on and compared to other widely used techniques. Based on the results included herein, future work is proposed to extend the knowledge and breadth of BSI applications.

1.5 References

(1) Voet, D.; Voet, J. G. In *Biochemistry;* John Wiley & Sons, Inc.: United States of America, **2004**, pp 1591.

(2) McMurray, J.; Fay, R. C. In *Chemistry;* Corey, P. F., Ed.; Prentice-Hall, Inc.: Englewood Cliffs, New Jersey USA, **1995**.

(3) Schultz, E.; Galland, R.; Du Bouetiez, D.; Flahaut, T.; Planat-Chretien, A.; Lesbre, F.; Hoang, A.; Volland, H.; Perraut, F. *Biosens. Bioelectron.* **2008***, 23*, 987-994.

(4) Ince, R.; Narayanaswamy, R. *Analytica Chimica Acta* **2006***, 569*, 1-20.

(5) Bornhop, D. J. *Appl. Opt.* **1995***, 34*, 3234-3239.

(6) Wiseman, T.; Williston, S.; Brandts, J. F.; Lin, L. N. *Anal. Biochem.* **1989***, 179*, 131-137.

(7) McKinnon, I. R.; Fall, L.; Parody-Morreale, A.; Gill, S. J. *Anal. Biochem.* **1984***, 139*, 134-139.

(8) Carbonell, T.; Freire, E. *Biochemistry* **2005***, 44*, 11741-11748.

(9) Liang, Y. *Acta Biochim. Biophys. Sin. (Shanghai)* **2008***, 40*, 565-576.

(10) Pigga, J. M.; Teprovich, J. A.,Jr; Flowers, R. A.,2nd; Antonio, M. R.; Liu, T. *Langmuir* **2010***, 26*, 9449-9456.

(11) Ladbury, J. E. *Chem. Biol.* **1996***, 3*, 973-980.

(12) Ababou, A.; Ladbury, J. E. *J. Mol. Recognit.* **2007***, 20*, 4-14.

(13) Campoy, A. V.; Freire, E. *Biophs Chem* **2005***, 115*, 115-124.

(14) MicroCal, Inc. *www.microcal.com* **2008**.

(15) Elmore, W. C.; Heald, M. A. In *Physics of Waves;* Courier Dover Publications: New York, **1985**, pp 477.

(16) Born, M.; Wolf, E. In *Principles of Optics: electromagnetic theory of propagation, interference and diffraction of light;* Cambridge University Press: Cambridge, **1999**, pp 952.

(17) Young, T. Philos. *T. R. Soc. Lond.* **1804**, *94*.

(18) Ingle, J. D.; Crouch, S. R. In *Spectrochemical Analysis;* Prentice-Hall, Inc.: Englewood Cliffs, New Jersey, **1988**, pp 590.

(19) Darling, D. The Internet Encyclopedia of Science; Light. http://www.daviddarling.info/encyclopedia/L/light.html. **2011**.

(20) Brandenburg, A.; Henninger, R. *Appl. Opt.* **1994**, *3*3, 5941-5947.

(21) Ymeti, A.; Kanger, J. S.; Greve, J.; Lambeck, P. V.; Wijn, R.; Heideman, R. G. *Appl. Opt.* **2003**, *4*2, 5649-5660.

(22) Farfield Group Ltd. Dual Polarisation Interferometry. http://www.farfield-group.com/technology_dpi.asp. **2011**.

(23) Heideman, R. G.; Lambeck, P. V. *Sensor Actuat B-Chem* **1999**, *6*1, 100-127.

(24) Weisser, M.; Tovar, G.; Mittler-Neher, S.; Knoll, W.; Brosinger, F.; Freimuth, H.; Lacher, M.; Ehrfeld, W. *Biosens. Bioelectron.* **1999**, *1*4, 405-411.

(25) Varma, M. M.; Inerowicz, H. D.; Regnier, F. E.; Nolte, D. D. *Biosens. Bioelectron.* **2004**, *1*9, 1371-1376.

(26) Varma, M. M.; Nolte, D. D.; Inerowicz, H. D.; Regnier, F. E. *Opt. Lett.* **2004**, *29*, 950-952.

(27) Bradshaw, J. T.; Mendes, S. B.; Saavedra, S. S. *Anal. Chem.* **2005**, *7*7, 28A-36A.

(28) Skivesen, N.; Tetu, A.; Kristensen, M.; Kjems, J.; Frandsen, L. H.; Borel, P. I. *Opt. Express* **2007**, *1*5, 3169-3176.

(29) Ronan, G. *SPIE oe magazine* **2004**, 17-20.

(30) Bornhop, D. J.; Latham, J. C.; Kussrow, A.; Markov, D. A.; Jones, R. D.; Sorensen, H. S. *Science* **2007**, *31*7, 1732-1736.

(31) Elkashef, H. *Opt. Mater.* **1997***,* 8, 175-183.

(32) Maroulis, G.; Xenides, D.; Hohm, U.; Loose, A. *J. Chem. Phys.* **2001***, 11*5, 7957-7967.

(33) Sota, H.; Hasegawa, Y.; Iwakura, M. *Anal. Chem.* **1998***, 7*0, 2019-2024.

(34) Weast, R. C., Ed.; In *Handbook of Chemistry and Physics;* CRC Press: Cleveland, Ohio, **1975**.

(35) Wang, Z.; Swinney, K.; Bornhop, D. J. *Electrophoresis* **2003***, 2*4, 865-873.

(36) Tarigan, H. J.; Neill, P.; Kenmore, C. K.; Bornhop, D. J. *Anal. Chem.* **1996***, 6*8, 1762-1770.

(37) Swinney, K.; Markov, D.; Hankins, J.; Bornhop, D. J. *Analytica Chimica Acta* **1999***, 40*0, 265-280.

(38) Markov, D.; Begari, D.; Bornhop, D. J. *Anal. Chem.* **2002***, 7*4, 5438-5441.

(39) Markov, D. A.; Swinney, K.; Norville, K.; Lu, D.; Bornhop, D. J. *Electrophoresis* **2002***, 2*3, 809-812.

(40) Swinney, K.; Bornhop, D. J. *Analyst* **2000***, 12*5, 1713-1717.

(41) Swinney, K.; Markov, D.; Bornhop, D. J. *Anal. Chem.* **2000***, 7*2, 2690-2695.

(42) Yap, K. L.; Ikura, M. *Handbook of Metalloproteins* **2004***,* 3, 447-458.

(43) Kelly, T. R.; Kim, M. K. *J. Am. Chem. Soc.* **1994***, 11*6, 7072-7080.

Chapter 2

Instrument Design

Since its development in 1995,[1] BSI has been modified and employed for numerous applications. Initially BSI was used as an RI detector using capillaries to provide microvolume detection.[2] Capillaries provided the optics for much of the early work including temperature measurements,[3,4] polarity,[5] universal detection in high-performance liquid chromatography[6] and electrophoresis.[7,8] Based on these studies, the applications of BSI were tested using channels contained within microfluidic chips made of silica (glass) or polydimethylsiloxane (PDMS).[9-13] The interferometer described below and used in subsequent experiments utilizes glass chips with microfluidic rectangular channels for sample introduction. The glass chips are made of borosilicate, which is desirable because it is inert, stable, hydrophilic (but can be modified to become hydrophobic), non-porous, translucent, and inexpensive. The BSI chips were produced by Micronit Microfluidics®, to create uniform channels with reliable optics. Through a wet etching technique, 90 μm wide channels were created (Fig. 2.1).[14]
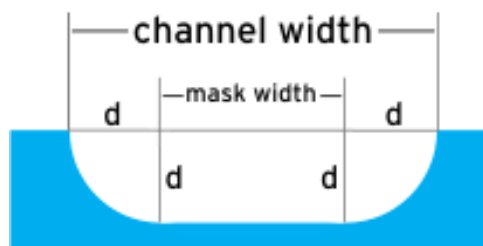
Figure 2.1 Cross-sectional view of microfluidic channels used for BSI. The channel has a cross-sectional area of 2.9 nm^2 with a depth (d) of 40 μm and a mask width of 10 μm to create an optical probe volume of ca. 290 pL.

Since this technique relies on changes in RI, it is essential to minimize variations in RI that arise from wavelength or thermal fluctuations. Monochromatic light (632.8 nm) from a HeNe laser is used to maintain a constant wavelength. This laser was fiber optically coupled to a focusing lens with a 283 mm working distance to create a spot size of 100 μm when properly aligned. The correct working distance was measured physically to ensure that parallel rays impinge the channel. The temperature is tightly regulated using a thermistor to detect and a peltier thermoelectric module to control temperature variations. With this setup, it is more accurate to keep the temperature constant by heating rather than cooling. Therefore, the room temperature is kept fairly low (21 °C) so that the temperature controller is constantly heating the instrument stage to 25 °C. However, even with this configuration, it is important to minimize the temperature variations in the laboratory. The laser source must also be kept separate from the chip holder because it generates heat that can impact the temperature of the chip. Additionally, the airflow surrounding the instrument must be addressed to keep thermal variations and vibrations to a minimum. The air vents in the laboratory were inconveniently positioned directly above the instrument, requiring a tarp to be hung from the ceiling to reduce the airflow.

The generic schematic for BSI, (recall Fig. 1.7), can be arranged with multiple configurations. The initial phase of this project involved building and developing BSI by trying out variations in the instrument design. Originally, BSI was built so that the chip was aligned horizontal to the optical breadboard. This set-up facilitates sample loading by pipetting directly into the well and vacuuming the sample through the channel (Fig 2.2).

The problem with this configuration is the requirement of a dark room because the individual elements are not enclosed. Ideally, the entire system is isolated within a box to minimize thermal variations and allow the user to perform BSI experiments in a brightly lit laboratory.
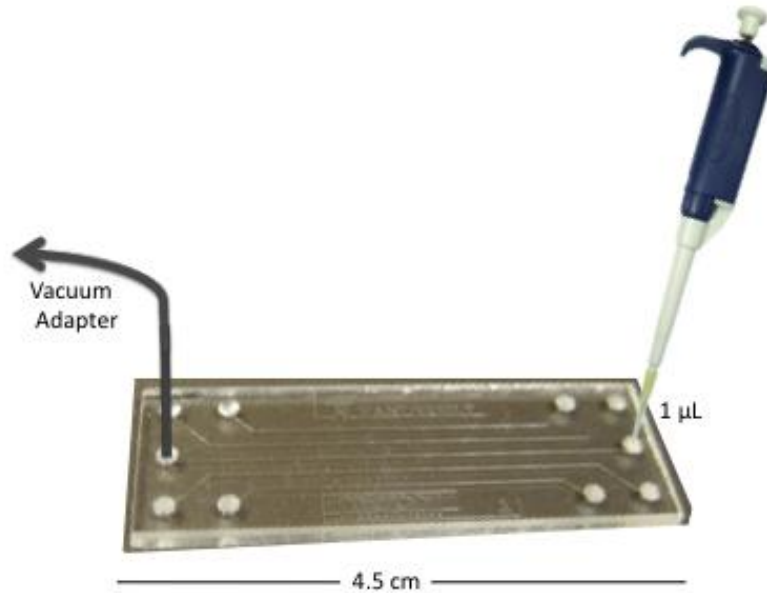
Figure 2.2 Enlarged photo of microfluidic chip used for BSI experiments showing a pipette and vacuum adapter for sample introduction.

Attempts were made to isolate the instrumental components by placing the chip perpendicular to the table and building a box around the instrument (Fig 2.3). While this may seem like a straightforward task, it was difficult to align the incoming and outgoing laser beams with the mirror, microfluidic channels, and detector while constrained within a box. To avoid thermal variations inside the box, the laser source was kept separate. Additionally, the fiber-couple was removed to ease alignment. Since the chip was vertically positioned, the incoming laser beam could hit the chip directly to generate the back-scattered fringe pattern without the need for a mirror. However, if the incoming

laser beam hit the chip at a 90° angle, the fringe pattern was directly back-scattered into the laser, generating a substantial amount of noise. Therefore, the chip was positioned at a slight angle so that the centroid of the fringe pattern hit above or below the incoming laser beam. The mirror was then positioned at a location within the box to direct the fringe pattern to the detector without interfering with the incoming laser beam.
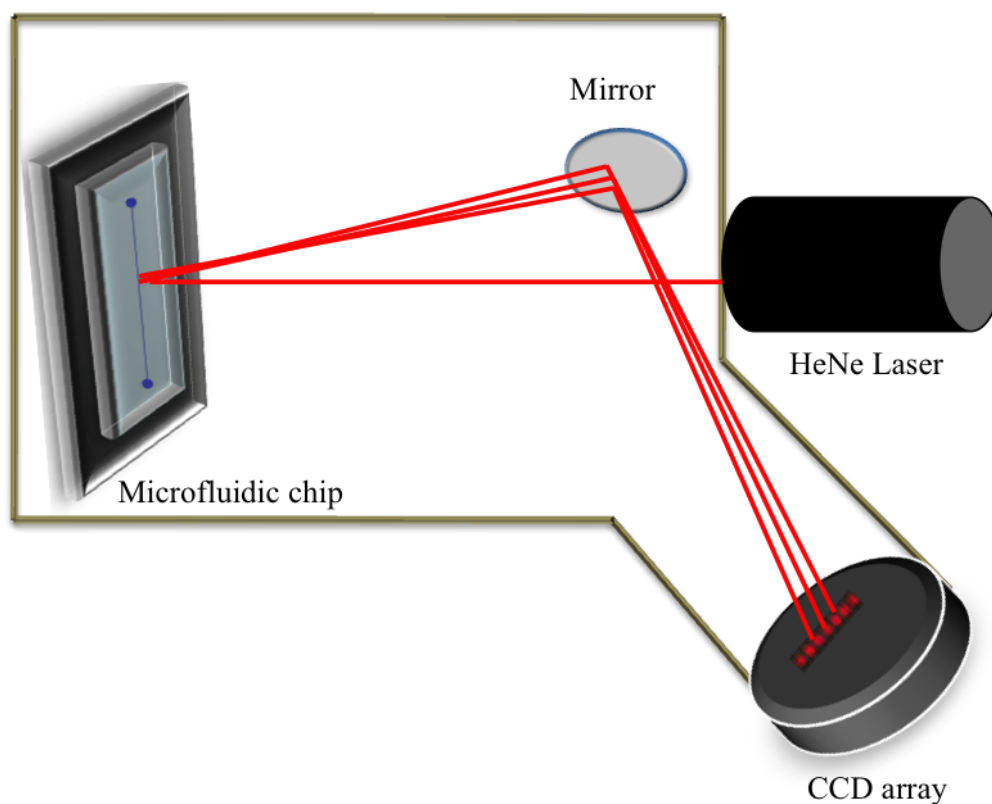
Figure 2.3 Schematic of BSI setup enclosed within a box.

By enclosing everything in a box, the sample must be introduced into the channel from an access point outside of the box. Sample introduction was accomplished by using polyetheretherketone (PEEK) tubing with adaptors to connect the tubing to the sample wells. Unfortunately, the PEEK tubing and adapters introduced void volume into the

system that caused incomplete removal of sample, interfering with subsequent experiments. The PEEK tubing was not a large problem when carrying out glycerol calibrations because the detection limits were the same or better than the horizontal chip configuration (in the 10^{-6} range). However, when attempting macromolecular binding experiments, the void volume and increased surface area due to the tubing were problematic, leading to irreproducible results.

After much time was spent working on the instrument design, we decided to move forward with experiments using the original design with the horizontal chip (Fig 2.4). Although this method required a dark workspace, the ease of sample introduction allowed for reproducible results. Additionally, at this time an independent company (Molecular Sensing, Inc.) was created to resolve the problems with instrument design and engineer a BSI prototype.
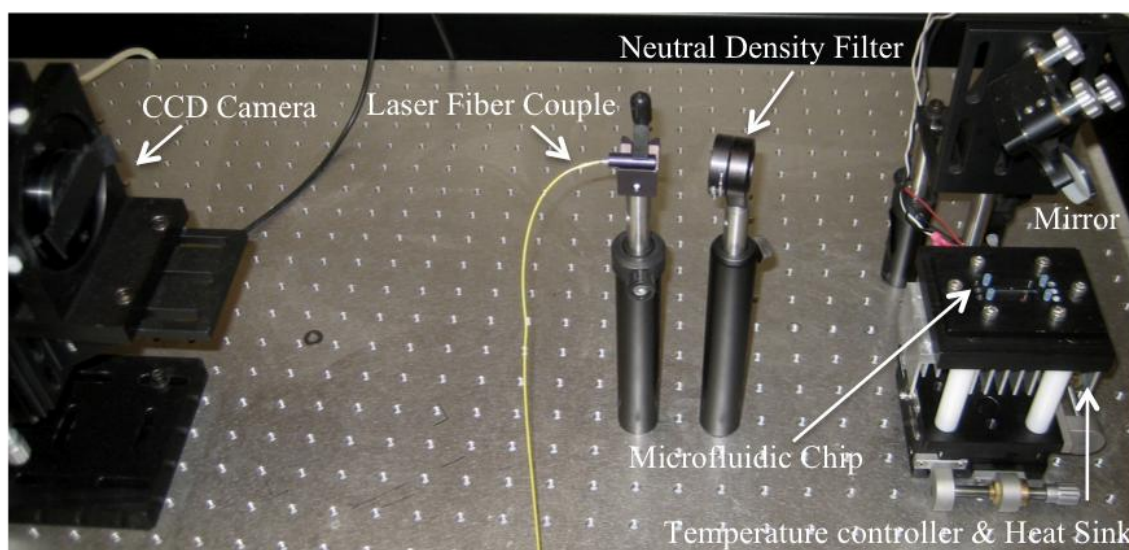
Figure 2.4 Photograph of BSI in the laboratory.

References

(1) Bornhop, D. J. *Appl. Opt.* **1995***, 34*, 3234-3239.

(2) Bornhop, D. J.; Houlne, M. P.; Kenmore, C. K.; Hankins, J. *LASER FOCUS WORLD* **1996***, 32*, 83.

(3) Tarigan, H. J.; Neill, P.; Kenmore, C. K.; Bornhop, D. J. *Anal. Chem.* **1996***, 68*, 1762-1770.

(4) Markov, D. A.; Bornhop, D. J. *Fresenius J. Anal. Chem.* **2001***, 371*, 234-237.

(5) Swinney, K.; Hankins, J.; Bornhop, D. J. *J. Capill Electrophor. Microchip Technol.* **1999***, 6*, 93-96.

(6) Kenmore, C. K.; Erskine, S. R.; Bornhop, D. J. *J. Chromatogr. A* **1997***, 762*, 219-225.

(7) Swinney, K.; Bornhop, D. J. *Electrophoresis* **2000***, 21*, 1239-1250.

(8) Swinney, K.; Pennington, J.; Bornhop, D. J. *Analyst* **1999***, 124*, 221-225.

(9) Swinney, K.; Bornhop, D. J. *Analyst* **2000***, 125*, 1713-1717.

(10) Swinney, K.; Markov, D.; Bornhop, D. J. *Anal. Chem.* **2000***, 72*, 2690-2695.

(11) Swinney, K.; Bornhop, D. J. *Electrophoresis* **2001***, 22*, 2032-2036.

(12) Wang, Z.; Swinney, K.; Bornhop, D. J. *Electrophoresis* **2003***, 24*, 865-873.

(13) Markov, D. A.; Dotson, S.; Wood, S.; Bornhop, D. J. *Electrophoresis* **2004***, 25*, 3805-3809.

(14) Williams, K. R.; Muller, R. S. *J. Microelectromech S.* **1996***, 5*, 256-269.

Chapter 3

Benchmarking BSI through analysis of calmodulin-ligand interactions

3.1 Introduction

The characterization of protein binding interactions is crucial to the understanding of biological processes and comparison of therapeutic efficacies. To evaluate the binding affinity of protein-ligand interactions, it is important to simulate *in vivo* conditions, which requires label-free detection of proteins in a free-solution system. Unfortunately, many techniques fall short of these requirements. Several surface immobilization techniques are routinely used to carry out measurements, such as surface plasmon resonance (SPR), interferometry, and acoustic wave guide.[1] While surface-immobilizing techniques have provided invaluable knowledge in the study of protein interactions, they do not reflect a physiologically relevant environment and have drawbacks including time-consuming and often expensive surface preparation, potential interference with binding energetics or kinetics, and inability to study unknown binding pairs.

Free-solution techniques are advantageous because there is substantially less preparation required and the risk of perturbing the system is significantly reduced. These techniques include affinity chromatography,[2] flow dialysis,[3] fluorescence,[1] isothermal titration calorimetry (ITC),[4] enthalpic arrays,[5] and back-scattering interferometry (BSI).[6] All of these techniques have different advantages and disadvantages including cost, efficiency, accuracy, and the type of information provided. For example, fluorescence assays are highly sensitive but typically require time-consuming fluorescent labeling that

can also interfere with structure and stability.[7] ITC has the advantage of providing a complete thermodynamic profile; however, it is low throughput and often requires high concentrations and volumes.[8] On the other hand, enthalpic arrays enable low-volume measurements but have high detection limits ($\sim 5 \times 10^{-5}$ M) and thus can only be used to study lower affinity binding interactions.[5]

When studying protein systems it is crucial to reduce sample consumption and mimic *in vivo* conditions. The development of new techniques to study interactions in free-solution, with label-free detection can provide more physiologically relevant data. BSI is capable of studying interactions in a label-free, free-solution manner, using small volumes and low concentrations, making it an advantageous alternative to the study of protein systems. This chapter describes the use of BSI with an ITC benchmark to compare the binding constants of several label-free interactions in a free-solution system by studying Calmodulin (CaM) and its interaction with various ligands.

CaM is a ubiquitous Ca^{2+} binding protein that acts as a secondary messenger for Ca^{2+}-mediated signaling.[9, 10] Four Ca^{2+}-binding sites provide the means for Ca^{2+} sensing and signal transduction. CaM is important for several biological processes including protein translation, cell cycle progression, long-term potentiation, and microtubule assembly.[9-11] Hundreds of CaM binding proteins exist that can bind to either ApoCam or Ca^{2+}-CaM. The binding of CaM to these various proteins is involved in biological processes such as inflammation, metabolism, apoptosis, muscle contraction, short- and long-term memory, nerve growth, and the immune response.[10]

Due to the large range of CaM binding proteins, the interactions and binding affinities vary depending on the structure and function of the CaM binding protein. To examine the scope of interactions that can be studied with BSI, CaM binding interactions were measured with an ion (Ca^{2+}), a small molecule (Trifluoperazine-dihydrochloride, Tfp), a peptide (myosin light chain kinase peptide, M13), and a protein (Calcineurin, CaN). For each binding partner, the results from BSI were compared to data obtained with ITC. These interactions were investigated to benchmark BSI and determine the advantages and disadvantages of each approach. Results from this study show that while ITC provides a complete thermodynamic profile, BSI is more applicable for high-throughput, cost-efficient studies due to high sensitivity and low volume requirements.

3.2 Materials and Methods

3.2.1 Sample Preparation

CaM, CaN, and Tfp were purchased from Sigma-Aldrich and Calmodulin inhibitory peptide (M13) was purchased from Calbiochem. Samples were reconstituted according to company recommendation and further diluted to the correct concentration. Ca^{2+}-free buffer consisted of 0.1 M HEPES, 0.1 M KCl, and 0.1 mM EGTA at a pH of 7.5. The Ca^{2+}-containing buffer was the same as the previous buffer, except that EGTA was replaced with 0.2 mM $CaCl_2$. ITC samples were dialyzed to obtain an identical pH. Protein and peptide concentrations were confirmed using UV absorbance.

3.2.2 ITC

Experiments were carried out using a MicroCal VP-ITC. Before each experiment, the sample cell and syringe were cleaned with Contrad-70 and rinsed with MQ-H_2O and buffer. Prior to loading, solutions were degassed using a vacuum for 15 minutes. The reference cell was filled with thoroughly degassed MQ-H_2O and changed every week. The sample cell was loaded with approximately 1.5 mL of protein solution and great care was needed to make sure no air bubbles were introduced into the cell. The injection syringe was purged and refilled several times before proceeding to ensure a uniform sample. The temperature was kept at 25ºC and the volume of injections varied from 3-8 µL to a final volume of 250 µL. After a successful experiment, the ligand was injected into buffer to obtain a heat of dilution. The heat of dilution was then subtracted from the binding isotherm to obtain the final plot. This plot was then fit to a one-site or multiple-sites binding model using Origin software to obtain n, K_a, ΔH, and ΔS.

3.2.3 BSI

The BSI results contained herein were obtained by our collaborators at Vanderbilt University. The HeNe laser and temperature controller were turned on at least an hour before the experiments were conducted to ensure equilibrium. The channels in the fluidic chips were cleaned with 1% Tween-20 and rinsed with MQ-H_2O and buffer before each run. The CaM concentration was kept constant while the ligand concentration varied depending on the number of binding sites and the change in signal generated. In the case of high-affinity binding partners, the concentrations were in the nanomolar range, while lower-affinity binding partners were studied in the micromolar range. To study binding

41

events, a vacuum was used to introduce the samples into a y-shaped channel with a serpentine mixer followed by a squeeze. This chip design provided the sample mixing necessary to obtain reliable kinetic data. Once the protein and ligand samples were both in the channel, the vacuum was released and the binding event recorded; monitored by dramatic signal changes. The binding curve was then fit to an exponential rise to max equation as derived in section Chapter 1.3.5.

3.2.4 Laser Light Scattering

A commercial Brookhaven Instruments laser light scattering (LLS) spectrometer was used for the dynamic light scattering (DLS) experiments. DLS studies provided the hydrodynamic radii (R_h) of the M13 samples at various concentrations. These experiments were carried out using a solid-state laser operating at 532 nm with a scattering angle of 90°. The R_h values of the particles are calculated from the characteristic line width from the intensity-intensity time correlation functions ($\Gamma G(\Gamma)$), analyzed with the CONTIN method.[12] Average intensities greater than 100 kcps indicate that large, supramolecular species are present in a given sample. Information on the particle distribution in solution is also provided by DLS measurements from a plot of $\Gamma G(\Gamma)$ versus R_h.

3.3 Results & Discussion

3.3.1 CaM/Ca^{2+}

The presence of four Ca^{2+} binding sites induces major conformational changes in the CaM structure (Fig. 3.1). Ca^{2+} binding leads to the exposure of hydrophobic domains that are necessary to bind a wide range of targets.[13] The BSI experiments (Fig. 3.2) were carried out with 5 μM CaM and Ca^{2+} concentrations ranging from 0-100 μM. No dialysis was required for the BSI samples because slight pH changes did not alter the signal change. The analysis of the kinetic BSI data was complicated by the presence of 4 Ca^{2+} binding sites. The large error bars associated with the kinetic K_D value are most likely due to an oversimplified kinetic fit since there are four binding sites. Multiple binding sites cannot be accounted for with the kinetic model used. Kinetic analysis using a four-site model still provides questionable fits, placing a limit on this technique when there are multiple binding sites. The error associated with the fitting model for steady-state measurements is significantly reduced with multiple trials producing K_D values ranging from 3.40 – 18.23 μM.
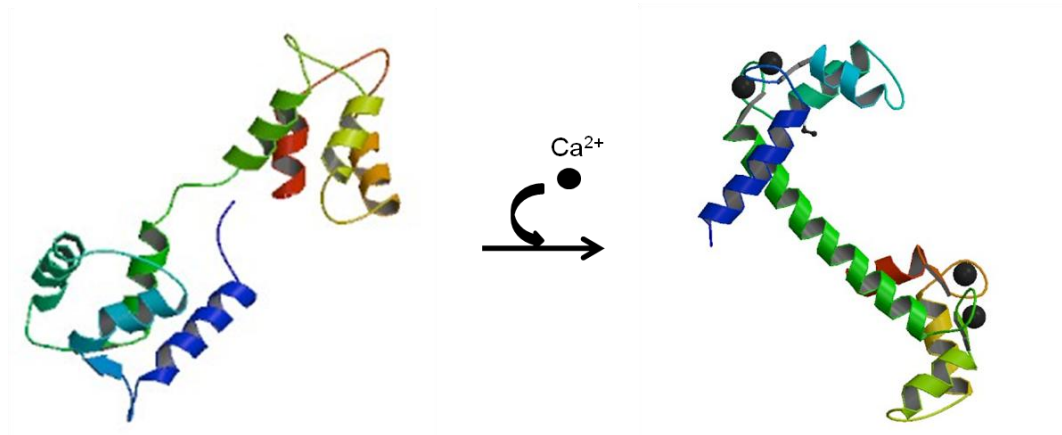
Figure 3.1 Crystal structures of apo-CaM [14] and Ca^{2+}-CaM [15] show a conformational shift to a dumbbell-like structure when 4 Ca^{2+} ions bind.
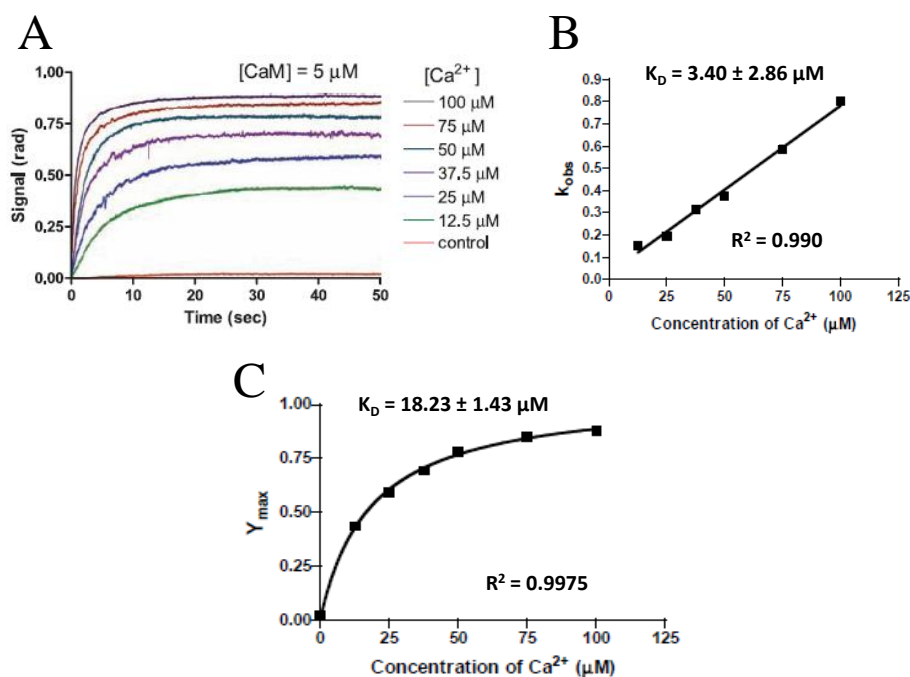
Figure 3.2 CaM-Ca^{2+} BSI data obtained from Dr. Bornhop's group.[6] A) Kinetic BSI data of CaM-Ca^{2+} binding. Signal was recorded upon sample introduction with CaM held constant at 5 μM and Ca^{2+} varied from 0-100 μM. Each binding curve was fit to obtain k_{obs}. B) Plot of k_{obs} versus Ca^{2+} concentration generated from kinetic data to obtain a K_D of 3.40 ± 2.86 μM. C) End-point BSI data from CaM-Ca^{2+}, carried out at the same concentration as the kinetic data. This curve was fit to a one-site binding hyperbola to obtain a K_D of 18.23 ± 1.43 μM.

For the CaM/Ca^{2+} ITC experiment, CaM was placed in the sample cell at 9.3 μM while 1.0 mM Ca^{2+} was added via syringe. A total of 75 three-μL injections were carried out to fully saturate the CaM-Ca^{2+} binding sites. For this experiment, it was crucial to dialyze CaM prior to the experiment because CaM is slightly acidic.[10] Even a slight change in pH can interfere with ITC results due to thermal changes from simple hydrogen transfers. The ITC results (Fig. 3.3) show that four Ca^{2+} molecules bind to one CaM molecule. Nonspecific binding also occurs as seen by the slight rise in the isotherm after CaM has already reached saturation. Due to the non-specific binding events seen in the ITC isotherm, two different curve-fits were used; a multiple binding site algorithm set to 4 or 6 binding sites. The 4-site curve fit produced K$_D$ values with relatively small error, ranging from 0.15 μM − 63.7 μM for the four specific binding sites. When the non-specific binding sites were taken into account, the curve fit had larger margins of error and produced binding constant values ranging from 0.059 − 13.24 μM for the four specific binding sites and 21.05 − 57.47 μM for the two non-specific binding sites (Table 3.1). Due to the large error associated with the 6-site model, only the 4-site model is shown below and used for comparison to BSI. However, both fits correlate with the BSI data and agree with the dissociative binding constants found using equilibrium or flow dialysis, ranging from 1-10 μM.[16, 17]
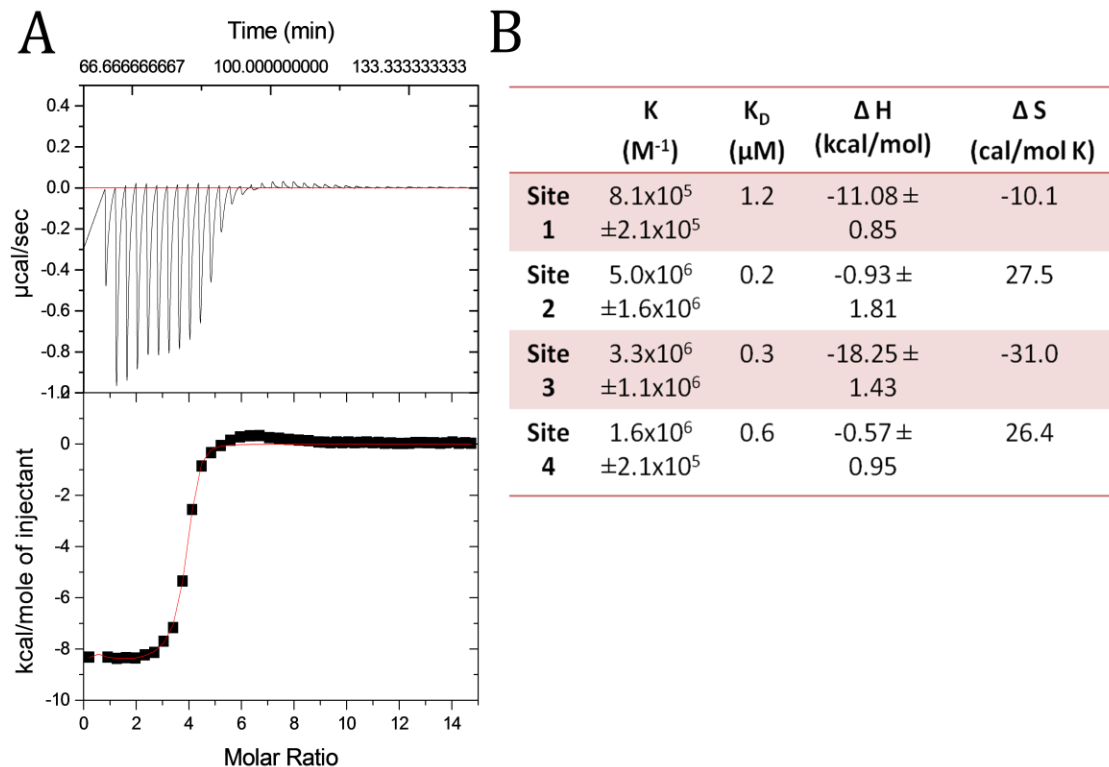
Figure 3.3 A) ITC data and integrated plot of CaM/Ca^{2+} binding. The experiment was carried out with [CaM] = 9.3 μM and 75 injections (3μL each) of 1 mM Ca^{2+}. This curve fit includes four specific Ca^{2+} binding sites but does not include the non-specific binding sites. B) Table of thermodynamic data obtained from Origin curve fitting.

	K (M^{-1})	K$_D$ (μM)	Δ H (kcal/mol)	Δ S (cal/mol K)
Site 1	8.1x10^5 ±2.1x10^5	1.2	-11.08± 0.85	-10.1
Site 2	5.0x10^6 ±1.6x10^6	0.2	-0.93± 1.81	27.5
Site 3	3.3x10^6 ±1.1x10^6	0.3	-18.25± 1.43	-31.0
Site 4	1.6x10^6 ±2.1x10^5	0.6	-0.57± 0.95	26.4

Table 3.1 Thermodynamic data obtained from CaM/Ca^{2+} ITC data fit to the 6-site binding model to include non-specific binding sites.

	K (M^{-1})	K$_D$ (μM)	ΔH (kcal/mol)	ΔS (cal/mol K)
Site 1	$7.55\times10^4 \pm 8.50\times10^4$	13.2	-13.5 ± 25.0	-23.2
Site 2	$3.43\times10^6 \pm 1.60\times10^6$	0.3	-12.1 ± 55.3	-10.8
Site 3	$1.67\times10^7 \pm 1.20\times10^7$	0.06	0.9 ± 33.2	36.4
Site 4	$1.07\times10^6 \pm 2.10\times10^5$	0.9	-10.3 ± 2.9	-6.8
Site 5	$4.75\times10^4 \pm 3.40\times10^4$	21.0	3.4 ± 1.4	32.8
Site 6	$1.74\times10^4 \pm 1.40\times10^4$	57.5	-0.5 ± 1.9	17.5

3.3.2 CaM/Tfp

Tfp is a member of the phenothiazine class of drugs that is used to bind and inactivate the calcium-bound form of CaM.[13] Four Tfp molecules can bind to Ca^{2+}-CaM to create a drastic change in the conformational structure of CaM (Fig. 3.4) to become more globular and therefore prevent interaction with normal targets.[18] CaM/Tfp interactions were carried out in the micromolar range for both BSI and ITC. CaM was reconstituted in Ca^{2+}-containing HEPES pH 7.5 buffer since previous research has shown that CaM binds Tfp best in its Ca^{2+}-bound form.[9]
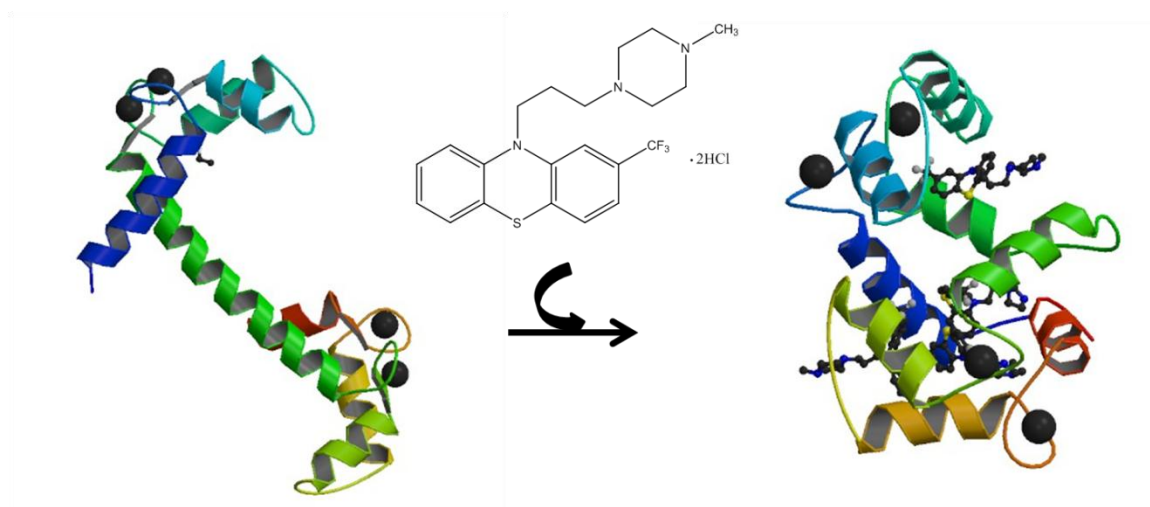
Figure 3.4 Crystal structure of Ca^{2+}-CaM[15] showing the conformational change that occurs when four Tfp molecules bind.[18]

For the BSI experiments, CaM was kept constant at 2 µM while Tfp ranged from 0 – 25 µM.[6] The binding constant found from BSI ranged from 3.59 - 5.0 µM in repeated experiments. In the ITC experiment, CaM was contained in the cell at 9.3 µM and Tfp was titrated in at 1 mM. A total of 75 three-µL injections were carried out to complete the isotherm. As seen in Figure 3.5, there are approximately four Tfp binding sites and several non-specific binding regions. The nonspecific binding seen here for Tfp is different than that for Ca^{2+}. In the case with nonspecific binding of Ca^{2+} to CaM, the nonspecific binding sites eventually reach saturation. The Tfp binding plot shows a gradual increase after the specific binding sites have been occupied. This increase signifies low-affinity binding of Tfp that can easily associate and dissociate from CaM, thus generating small thermal changes. The ITC experiment resulted in K_D values ranging from 5.95 µM – 0.146 mM. The results from both BSI and ITC are consistent

with previously reported values found using affinity chromatography, ranging from 1.72 μM – 0.151 mM.[19]
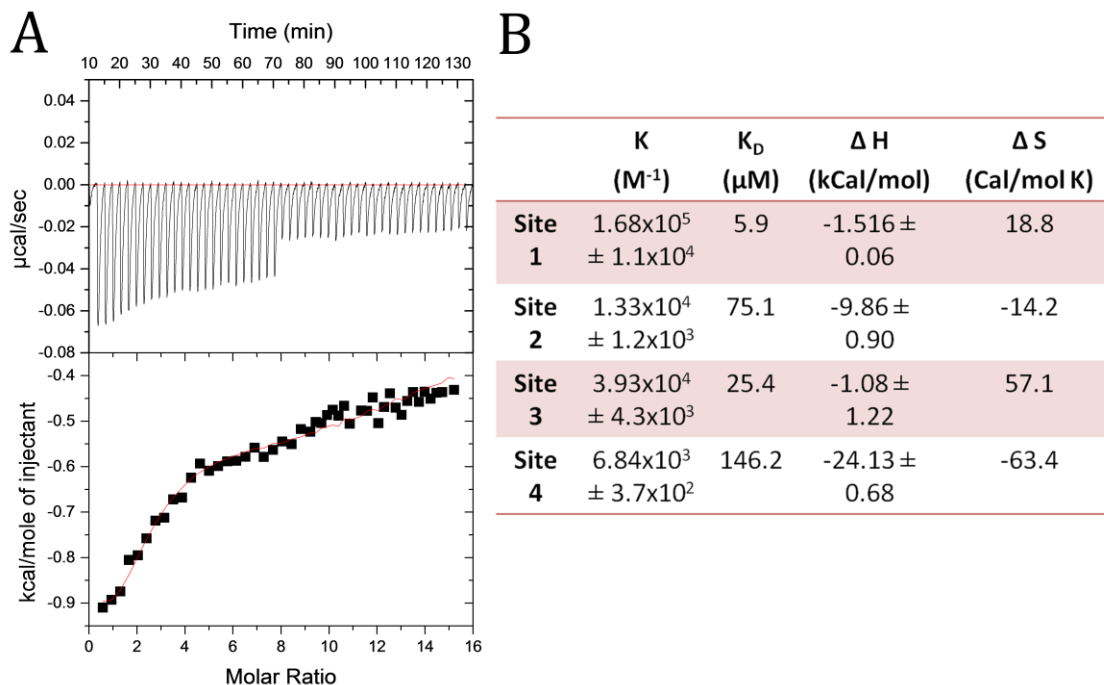
Figure 3.5 A) ITC results of CaM/Tfp binding. This experiment was run with [CaM] = 9.3 μM, and [Tfp] = 1 mM, 75 injections, 3 μL each. B) Thermodynamic data of CaM/Tfp provides and K_D ranging from 5.9 – 146.2 μM.

3.3.3 CaM/M13 peptide

The M13 peptide was derived from the CaM binding site of skeletal muscle myosin light chain kinase. This 17 residue peptide has a molecular weight of 2074.5 Da with the sequence Ac-RRKWQKTGHAVRAIGRL-NH$_2$ and binds calcium-bound CaM with high affinity in the nanomolar range.[11, 20, 21] The crystal and solution-phase structure of the interaction between M13 and Ca^{2+}-CaM have been elucidated by several groups

(Fig. 3.6).[22, 23]   These studies have shown that this binding event is driven by hydrophobic forces resulting in a drastic conformational change in the CaM structure.
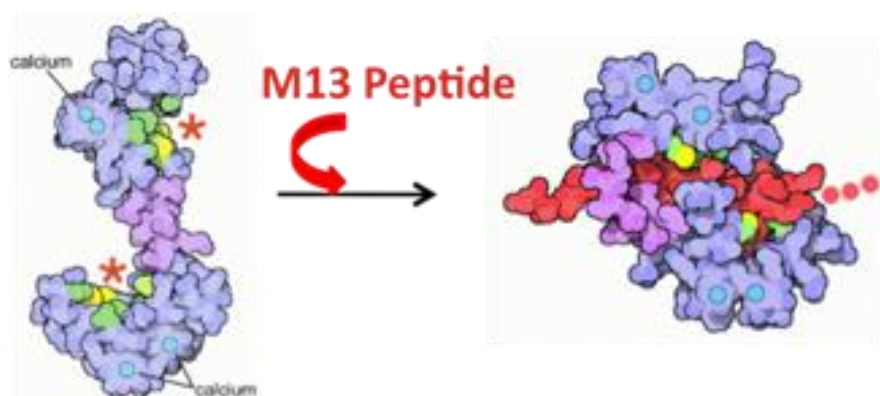
Figure 3.6 Hydrophobic forces drive the interaction between CaM and the M13 peptide with CaM folding over to bind M13.[11]

The energetics of the CaM-M13 interaction have been studied using a variety of techniques including surface plasmon resonance,[20] enzymatic inhibition assay,[24, 25] and stopped-flow fluorometry.[26]   While these techniques differed in interrogation methodologies, the binding affinities were all similar, with K_D values ranging from 3-9 nM[6, 20, 26] and inhibition constant (K_i) values ranging from 8.6 pM to 3.3 nM.[24, 25]

Since M13 binds CaM with high affinity, the BSI experiments were run at low concentrations with [CaM] equal to 5 nM and [M13] varying from 0-50 nM (Fig. 3.7). The kinetic runs were fit to obtain a K_D of 2.89 ± 0.74 nM while the end-point experiments generated a K_D value of 9.87 ± 1.12 nM.[6]   These values are in direct agreement with the published values that range from 3-9 nM.
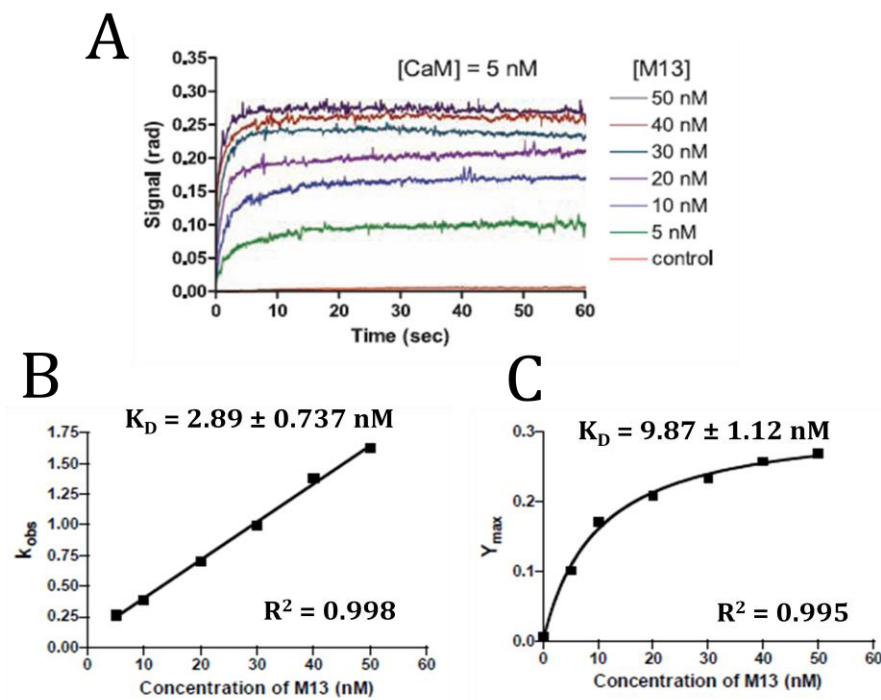
Figure 3.7 CaM-M13 BSI data obtained from Dr. Bornhop's group.[6] A) Kinetic BSI data of CaM-M13 binding with CaM held constant at 5 nM and M13 varied from 0-50 nM B) Plot of k_{obs} versus M13 concentration generated from kinetic curve fits to obtain a K_D of 2.89 ± 0.73 nM. C) End-point BSI data from CaM-M13, carried out at the same concentration as the kinetic data.

Unlike CaM/Ca^{2+} and CaM/Tfp, the CaM/M13 interaction was difficult to analyze calorimetrically. According to Wintrode and Privalov, the strong binding and the inability of ITC to detect small thermal changes at low concentrations make it difficult to accurately study CaM/M13 calorimetrically.[27] Our results are consistent with their findings and further analysis of the peptide structure shows aggregation at high concentrations, further complicating calorimetric analysis. Several ITC experiments were performed in Ca^{2+}-containing HEPES pH 7.5 buffer at varying concentrations in order to get a clean binding isotherm. These experiments were run with CaM in the

sample cell at concentrations ranging from 2 - 18 μM and the M13 peptide in the syringe ranging from 14-161 μM. The temperature was kept constant at 25 °C across all experiments and the injection size varied from 3-8 μL depending on the concentrations. Figure 3.8 shows the trends in the ITC data as the concentration of M13 is reduced from 0.161 to 0.035 mM. From this data, it can be seen that although the data becomes noisier as the M13 concentration is reduced, the molar ratio shifts closer to the accepted 1:1 stoichiometry.
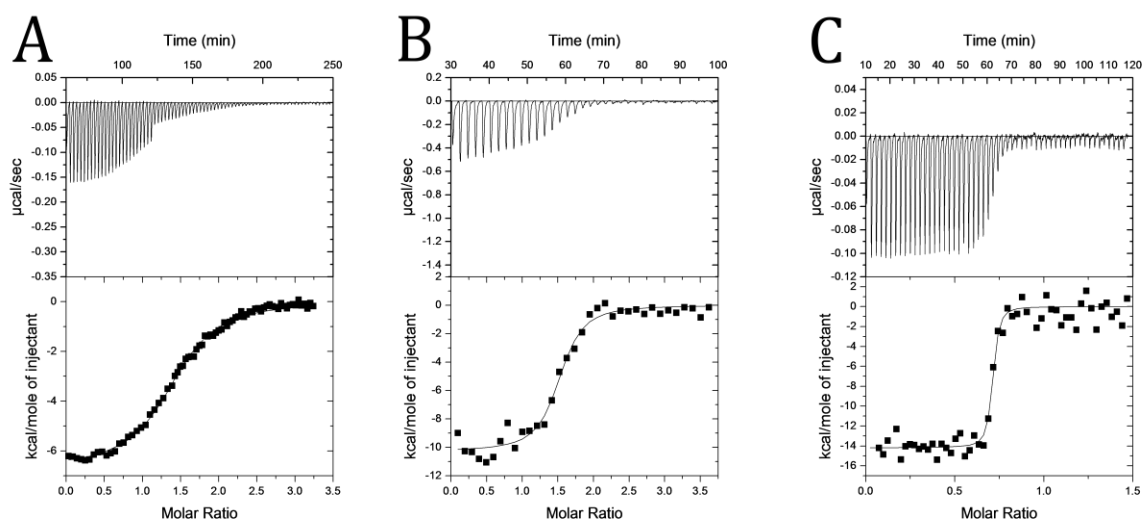
Figure 3.8 CaM-M13 ITC data from M13 peptide titrated into CaM at 25°C pH 7.5 with 0.2 mM Ca^{2+} present and run at varying concentrations of M13. A) ITC run with [CaM] = 15.5 μM and [M13] = 0.161 mM. B) ITC run with [CaM] = 15.2 μM and [M13] = 0.104 mM. C) ITC run with [CaM] = 5.0 μM and [M13] = 0.035 mM. See Table 3.2 for thermodynamic data associated with each curve fit.

Table 3.2 Thermodynamic average data from CaM-M13 ITC experiments; n = 3 for each set.

	Set 1 [CaM] = 11 μM [M13] = 108 μM	Set 2 [CaM] = 15 μM [M13] = 86 μM	Set 3 [CaM] = 4 μM [M13] = 28 μM
K (M⁻¹)	$2.51 \times 10^6 \pm 2.66 \times 10^5$	$5.87 \times 10^6 \pm 1.55 \times 10^6$	$3.51 \times 10^8 \pm 2.12 \times 10^8$
K_D (nM)	478	203	3.2
ΔH (kcal/mol)	-8.43 ± 0.11	-12.92 ± 0.35	-15.42 ± 0.45
ΔS (cal/mol K)	0.8	-12.5	-12.7

Not surprisingly, the calorimetric data of the CaM/M13 interaction showed a high dependence on protein and ligand concentrations. Table 3.2 lists the thermodynamic constants derived from ITC experiments carried out with decreasing concentrations of CaM and M13. These data indicate that as the concentration of M13 decreases, the binding affinity increases. This increase in binding strength is enthalpically driven and not entropically favorable. These data are in direct agreement with calorimetric data published by Wintrode and Privalov showing that the CaM/M13 interaction is enthalpically favorable.[16, 27]

While it is clear that the ITC values are consistent with reported values when run at low temperatures, more error existed in the data because the experiments were performed near the limits of detection. Another interesting finding in the ITC results is that the molar ratio varied between experiments. Reducing the M13 concentration from 0.161 to 0.035 mM shifted the experimental stoichiometry of the interaction from ~ 1.5 to

0.8.   Therefore, the discrepancies in the CaM/M13 ITC data are likely to be due to the high peptide concentrations required for the experiments.

To further investigate the concentration-dependent nature of the M13 peptide, dynamic light scattering (DLS) experiments were performed to observe potential peptide aggregation. These experiments were carried out with M13 concentrations ranging from 0.005 mg/mL to 0.1 mg/mL (2.41 µM to 48.2 µM). DLS studies provided the hydrodynamic radii (R_h) of the M13 aggregates at various concentrations, shown in the Table 3.3. Figure 3.9 also shows a broad particle distribution of the M13 samples; indicating a range of aggregates present in solution.

Table 3.3 Average hydrodynamic radii (R_h) of M13 samples at various concentrations.

M13 Concentration (mg/mL)	M13 Concentration (µM)	Average R_h (nm)
0.005	2.41	98.49
0.01	4.82	107.65
0.5	24.10	119.24
0.1	48.20	164.22
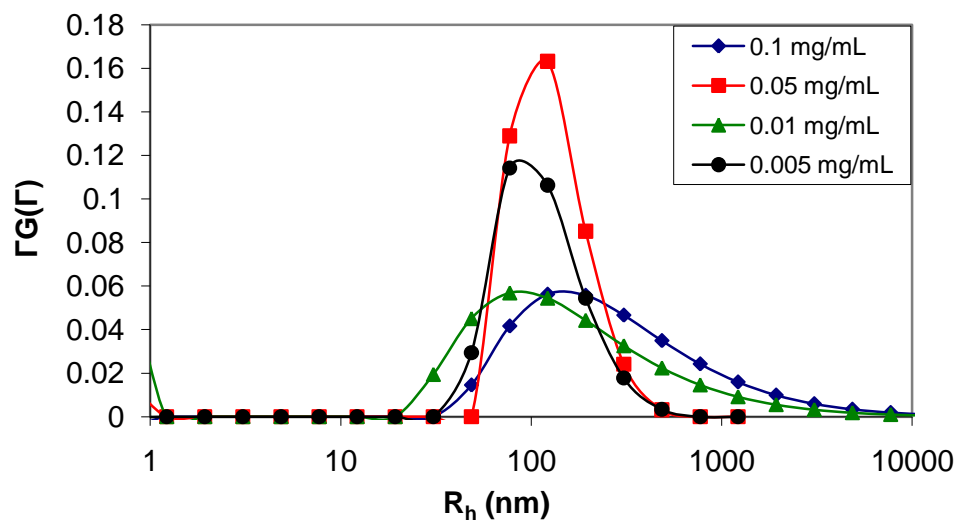
Figure 3.9 CONTIN analysis of DLS study on M13 sample solutions shows hydrodynamic radii distribution (by intensity) of M13 aggregates in solutions of various concentrations.

From the DLS studies it was concluded that aggregation of the M13 peptide occurred in the sample solutions. The average intensity of the signal and the average R_h value both decreased as the concentration of the peptide decreased (Fig. 3.10), which is consistent with concentration-dependent aggregation. Thus, at low concentrations, less aggregation occurs and smaller aggregates are formed in solution. Since the first two sets of ITC experiments were carried out at a higher peptide concentration than the DLS studies it is clear that aggregates were present. Therefore, the ITC data were skewed by the presence of peptide aggregates, whereas the BSI data was not because the experiments were performed at concentrations that were at least 5 orders of magnitude lower. Figure 3.11 shows the size distributions of low and high M13 concentrations corresponding to the concentrations used for the BSI and ITC experiments, respectively.

It is clear from this plot that an increase in M13 concentration results in large aggregates which were detrimental to the ITC results.
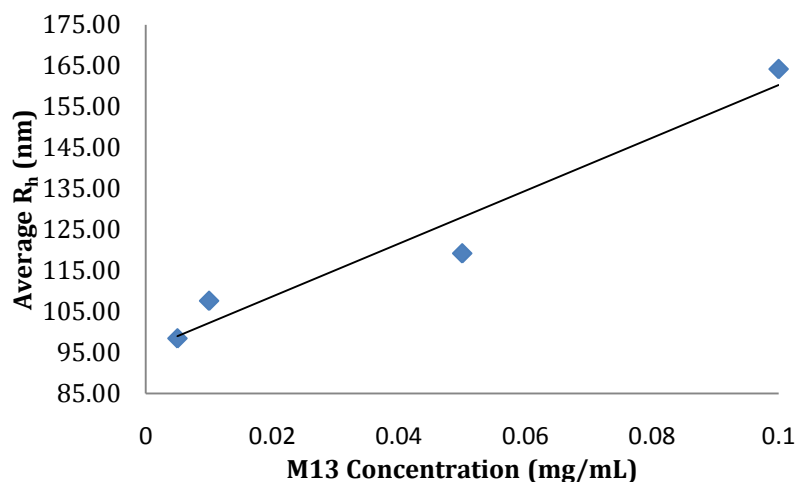
Figure 3.10 Plot of R_h vs. M13 concentration for samples of varying concentration. The linear relationship (r^2 = 0.95) between R_h and M13 concentration indicates a decrease in aggregate size with concentration.
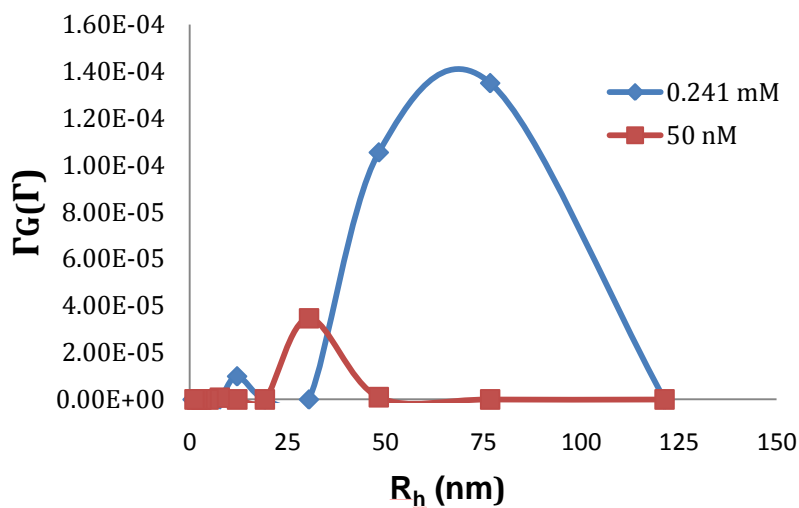
Figure 3.11 Hydrodynamic radii distribution profiles (by intensity) from DLS results carried out with low and high M13 concentrations corresponding to the maximum concentrations used for the BSI and ITC experiments, respectively.

3.3.4 CaM/CaN

The CaM/CaN binding interaction is the most complex of the binding pairs investigated in this study. Protein-protein binding studies are often difficult to undertake because of their size and numerous modes of interaction. CaN is a 77.8 kDa multifunctional, calcium-binding protein that binds Ca^{2+}-CaM with high specificity.[28] While the structure of CaM-CaN has never been elucidated, a peptide derived from the CaM binding region of CaN has been shown to induce large conformational changes in the Ca^{2+}-CaM structure (Fig. 3.12).[29]

Figure 3.12 Crystal structure of CaM bound to a CaN peptide shows a complex globular structure, requiring 4 Ca^{2+} ions bound to both CaM and the peptide for binding occur.[29]

The BSI experiments were carried out using a CaM concentration of 5 nM with CaN concentrations ranging from 5-50 nM.[6] A binding constant of 25.3 nM was calculated from fitting the binding curves and generating a plot of k_{obs} vs. concentration. The ITC experiments proved to be the most difficult of all of the CaM interactions investigated by this method. For each ITC trial, both proteins were dialyzed to ensure

identical pHs. Figure 3.13 shows the best isotherm obtained after numerous trials were performed. For this experiment, CaM was held in the sample cell at 9.3 μM while CaN was titrated in at 84.8 μM. A binding constant of 1.26 μM was calculated after fitting the binding isotherm. Several studies have been published using radioisotope and affinity chromatography, as well as steady-state and stopped-flow fluorescence, to find the binding constant of CaM/CaN interactions, ranging from 0.28 pM-16 nM. These values are only consistent with the BSI data and not the ITC data.[30-32]
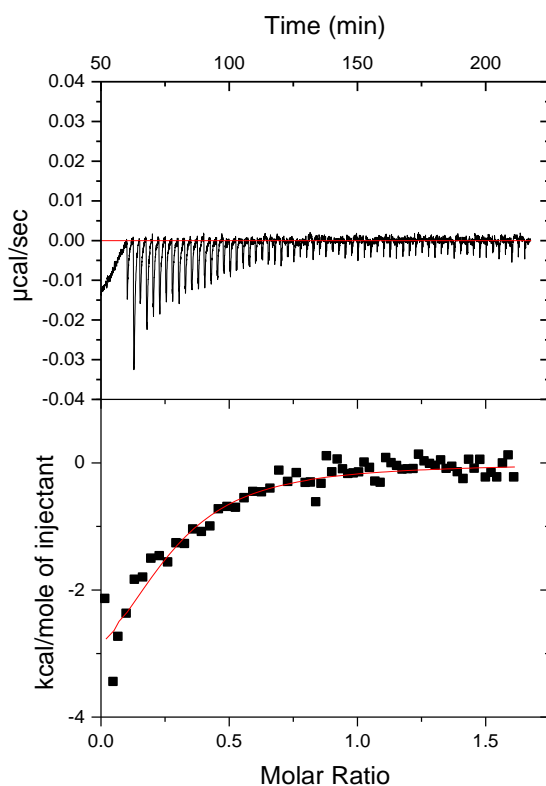
Figure 3.13 ITC data corresponding to CaM/CaN binding interactions. The integrated plot yielded a binding constant of 1.26 μM, ΔH of - 4293 ± 674.6 cal/mol, and ΔS of 12.6 cal/mol K.

The results from the ITC experiment do not agree with the published and accepted binding constant values of CaM/CaN binding. Although a binding event is clearly occurring, the binding constant is much lower than expected. This discrepancy may be due to the high CaN concentration necessary to generate measurable thermal changes. Experiments run with lower concentrations of CaM and CaN did not produce sufficient heat for reliable ITC measurement. High protein concentration can induce aggregation, especially if in the presence of misfolded CaN from reconstitution of the protein. This supposition is reasonable because the stoichiometry in the ITC experiment is far from the expected 1:1 molar ratio, indicating that there is less 'active' CaN present in solution to bind CaM. From these studies, it is clear that ITC is limited in its ability to measure the interaction between CaM and CaN whereas BSI can successfully monitor the interaction at concentrations that are relevant to physiological conditions.

3.4 Conclusion

The studies presented in this chapter highlighted the strengths and limitations of BSI and ITC. Since BSI can monitor binding with respect to time, the rate of the reaction can be determined, providing highly valuable information for the study and categorization of the kinetics of biochemical interactions. BSI utilizes microfluidic channels with small volumes allowing experiments to be performed with very little sample (~ 1 µL per trial), which is a huge advantage when working with expensive and difficult to isolate proteins. Additionally, BSI is very sensitive, allowing for experiments to be carried out at low concentrations. One problem with using high concentrations of proteins or peptides is the issue of aggregation. This issue was seen in the CaM/M13

peptide ITC experiment and possibly again in CaM/CaN binding. ITC required high concentrations of M13 in order to generate a clean isotherm and observe a binding event. However, as seen in the DLS and SLS results, aggregates are formed at high concentrations, which alter binding and result in large error in the calculation of the binding constant and stoichiometry of the reaction.

The kinetic analysis of CaM/Ca^{2+} demonstrated the limitations of BSI due to difficulties in fitting the data and accounting for 4 Ca^{2+} binding sites. ITC however, was able to accurately measure 4 Ca^{2+} bindings sites and determine the binding affinity for each site. One of the major advantages to ITC is that it can be used to obtain a complete thermodynamic profile and determine the number of binding sites. ITC is capable of measuring binding constants for each specific and nonspecific binding site, as was seen in the CaM/Ca^{2+} and CaM/Tfp experiments.

Disadvantages to using ITC include low-throughput analysis and the restrictions associated with measuring thermal changes. These include lack of sensitivity due to current technology and the background heat exchanged between side reactions (e.g. heats of dilution and hydrogen transfers from pH differences). ITC experiments require the exact same pH for the sample in the cell and the syringe. If the pH is slightly different, simple hydrogen transfers will occur with each injection, altering the thermodynamic data. In order to eliminate this problem the protein samples must be dialyzed prior to the experiment, which is not only time consuming but also risks a loss of sample. ITC also requires large volumes and thus more protein, which can become very costly when repeating experiments. Therefore, ITC is not practical for studying interactions of proteins that are expensive or difficult to isolate.

In summary, BSI is the method of choice when trying to determine the binding constant of a protein-ligand interaction. BSI uses very small volumes and has higher sensitivity than other techniques, allowing experiments to be carried out several times using only small amounts of valuable protein samples. Overall, BSI can be very useful for high-throughput assays and the determination of unknown binding constants. Conversely, ITC is the preferred method when a complete thermodynamic profile is desired. However, both ITC and BSI provide a clear advantage to other surface-immobilized and fluorescently modified techniques because of the ease of sample preparation and the ability to obtain information on a system without the risk of perturbation.

3.5 References

(1) Ince, R.; Narayanaswamy, R. *Analytica Chimica Acta* **2006***, 569*, 1-20.

(2) Tetala, K. K.; van Beek, T. A. *J. Sep. Sci.* **2010***, 33*, 422-438.

(3) Yazawa, M. *Methods Mol. Biol.* **2002***, 173*, 3-14.

(4) Ababou, A.; Ladbury, J. E. *J. Mol. Recognit.* **2007***, 20*, 4-14.

(5) Torres, F. E.; Kuhn, P.; De Bruyker, D.; Bell, A. G.; Wolkin, M. V.; Peeters, E.; Williamson, J. R.; Anderson, G. B.; Schmitz, G. P.; Recht, M. I.; Schweizer, S.; Scott, L. G.; Ho, J. H.; Elrod, S. A.; Schultz, P. G.; Lerner, R. A.; Bruce, R. H. *Proc. Natl. Acad. Sci. U. S. A.* **2004***, 101*, 9517-9522.

(6) Bornhop, D. J.; Latham, J. C.; Kussrow, A.; Markov, D. A.; Jones, R. D.; Sorensen, H. S. *Science* **2007***, 317*, 1732-1736.

(7) Daugherty, D. L.; Gellman, S. H. *J. Am. Chem. Soc.* **1999***, 121*, 4325-4333.

(8) Velazquez-Campoy, A.; Leavitt, S. A.; Freire, E. *Methods Mol. Biol.* **2004***, 261*, 35-54.

(9) Yap, K. L.; Ikura, M. *Handbook of Metalloproteins* **2004***, 3*, 447-458.

(10) Nelson, M. The EF-Hand Calcium-Binding Proteins Data Library. http://structbio.vanderbilt.edu/cabp_database/index.html. **1997**.

(11) Dutta, S.; Goodsell, D. S. RCSB Protein Data Bank. http://www.rcsb.org/pdb/static.do?p=education_discussion/molecule_of_the_month/pdb44_1.html. **2002**.

(12) Provencher, S. W. *Biophys. J.* **1976***, 1*6, 27-41.

(13) Cook, W. J.; Walter, L. J.; Walter, M. R. *Biochemistry* **1994***, 3*3, 15259-15265.

(14) Kuboniwa, H.; Tjandra, N.; Grzesiek, S.; Ren, H.; Klee, C. B.; Bax, A. *Nat. Struct. Biol.* **1995***,* 2, 768-776.

(15) Chattopadhyaya, R.; Meador, W. E.; Means, A. R.; Quiocho, F. A. *J. Mol. Biol.* **1992***, 228*, 1177-1192.

(16) Brokx, R. D.; Lopez, M. M.; Vogel, H. J.; Makhatadze, G. I. *J. Biol. Chem.* **2001***, 276*, 14083-14091.

(17) Gilli, R.; Lafitte, D.; Lopez, C.; Kilhoffer, M.; Makarov, A.; Briand, C.; Haiech, J. *Biochemistry* **1998***, 3*7, 5450-5456.

(18) Vandonselaar, M.; Hickie, R. A.; Quail, J. W.; Delbaere, L. T. *Nat. Struct. Biol.* **1994***,* 1, 795-801.

(19) Massom, L.; Lee, H.; Jarrett, H. W. *Biochemistry* **1990***, 29*, 671-681.

(20) Montigiani, S.; Neri, G.; Neri, P.; Neri, D. *J. Mol. Biol.* **199***6, 25*8, 6-13.

(21) Yao, Y.; Squier, T. C. *Biochemistry* **1996***, 35*, 6815-6827.

(22) Meador, W. E.; Means, A. R.; Quiocho, F. A. *Science* **1992***, 25*7, 1251-1255.

(23) Ikura, M.; Clore, G. M.; Gronenborn, A. M.; Zhu, G.; Klee, C. B.; Bax, A. *Science* **1992***, 25*6, 632-638.

(24) Blumenthal, D. K.; Charbonneau, H.; Edelman, A. M.; Hinds, T. R.; Rosenberg, G. B.; Storm, D. R.; Vincenzi, F. F.; Beavo, J. A.; Krebs, E. G. *Biochem. Biophys. Res. Commun.* **1988***, 15*6, 860-865.

(25) Torok, K.; Cowley, D. J.; Brandmeier, B. D.; Howell, S.; Aitken, A.; Trentham, D. R. *Biochemistry* **1998***, 3*7, 6188-6198.

(26) Torok, K.; Trentham, D. R. *Biochemistry* **1994***, 3*3, 12807-12820.

(27) Wintrode, P. L.; Privalov, P. L. *J. Mol. Biol.* **1997***, 26*6, 1050-1062.

(28) Klee, C. B.; Crouch, T. H.; Krinks, M. H. *Proc. Natl. Acad. Sci. U. S. A.* **1979***, 76*, 6270-6273.

(29) Ye, Q.; Li, X.; Wong, A.; Wei, Q.; Jia, Z. *Biochemistry* **2006***, 4*5, 738-745.

(30) Hubbard, M. J.; Klee, C. B. *J. Biol. Chem.* **1987***, 26*2, 15062-15070.

(31) Tallant, E. A.; Cheung, W. Y. *Arch. Biochem. Biophys.* **1984**, *232*, 269-279.

(32) Quintana, A. R.; Wang, D.; Forbes, J. E.; Waxham, M. N. *Biochem. Biophys. Res. Commun.* **2005**, *334*, 674-680.

Chapter 4

Comparison of free-solution versus surface-immobilized oligonucleotide hybridization using BSI

4.1 Introduction

DNA hybridization and stability are of major importance in many areas of research. Nucleic acid interactions with other nucleic acids and proteins are known to significantly impact both DNA hybridization and stability. To develop novel DNA-based diagnostics and therapeutics, nucleotide hybridization must be fully characterized and studied. While pursuing information on the nature of oligonucleotide hybridization one must take precautions to ensure that binding information obtained from a given technique is physiologically relevant. Hybridization assays are conventionally carried out using fluorescence energy transfer,[1] ITC,[2] circular dichroism (CD) spectroscopy,[3] absorption hyperchromicity, [4] wave sensing,[5] and SPR.[6] Although these techniques have vastly improved the study of nucleotide hybridization, most require either fluorescent labeling or surface immobilization for signal generation.

Fluorescent modification is often used in biological studies to track a molecule of interest. This modification is helpful for visualization but it can potentially interfere with the native conformation of the target molecule and hence alter binding energetics and stability.[7] Studies designed to determine the effects of fluorophore attachment on DNA duplex hybridization and stability have shown that the strand location and structure of the fluorophore are important factors to consider.[8-10] Moreira *et al.* carried out an extensive study on the stability of fluorescently labeled oligonucleotides and found that many

fluorophores stabilized the duplex by increasing the T_m and decreasing ΔG.[8] Additionally, Morrison and collaborators found that a fluorescein label has a significant effect on oligonucleotide hybridization equilibrium by subsequently decreasing ΔH and ΔS, in turn decreasing ΔG by 3.5 kcal/mol.[9] Although these studies have shown that fluorescent modification does not perturb DNA hybridization, it does impact the overall thermodynamics of duplex formation which must be considered when incorporating fluorophores into any study.

Similarly, surface immobilization can interfere with binding energy, especially if the binding site is in close proximity to the surface. Additionally, the chemical environment at the surface can change drastically due to surface immobilization. This is especially true for surface-immobilized DNA because of the negatively charged phosphate backbone. A study by Piunno *et al.* found that the charge-charge interactions at the single-stranded DNA (ssDNA) surface can change the local ionic strength, pH, and dielectric constant subsequently altering the thermodynamics of the hybridized double-stranded DNA (dsDNA).[11] Furthermore, the density of the immobilized ssDNA not only effects the charge density but it can be detrimental to hybridization assays due to steric effects, reducing the reproducibility of results.[12]

The most common method to interrogate duplex stability for surface-immobilized experiments is duplex melting with the surface-immobilized DNA compared to bulk solution.[11-15] While this is a good measure of stability, it cannot be used to determine the specific binding affinity of one oligonucleotide strand for another, nor does it reflect the conditions (i.e. low temperatures) in which these experiments are performed. Other work performed to address this problem has employed isotopic assays[16] and kinetic

66

hybridization studies[17] to analyze the impact of immobilization on DNA hybridization. These studies were useful in determining proper immobilization methods and addressing potential issues associated with dense packing of oligonucleotides, however, they were not able to quantify perturbation by comparison to results of a free-solution method. To date, it has been difficult to directly compare hybridization efficacies for surface-immobilized versus free-solution techniques since detection platforms are specifically designed for a single-sensing format. A method capable of examining this problem using a single experimental format would allow for a direct comparison between free-solution and surface-immobilized hybridization studies. The emergence of BSI as a versatile detection platform provides the link necessary to make such a comparison.[18-20]

It is our supposition that BSI can determine the affinity of several oligonucleotide hybridization systems to investigate the impact of fluorescent probes, surface immobilization, and mismatched base pairs on hybridization. In this chapter, BSI is used with an ITC and a UV-hyperchromicity benchmark to study the hybridization of a 30-base oligonucleotide probe strand (P_s) with five different 30mers. These included an unlabeled, perfectly complementary strand, a complementary 5'-labeled strand tagged with either cyanine-3 (Cy3) or fluorescein isothiocyanate (FITC), and two mismatched strands containing either a terminal CA/AC mismatch or an internal AG/GT mismatch. We hypothesize that BSI can successfully be used to quantify perturbations due to fluorescent labeling, surface immobilization, and mismatched base pairs. We expect that surface immobilization and an internal mismatch will have the most dramatic effect on oligonucleotide hybridization affinity while fluorescent labeling and a terminal mismatch will have modest impact on hybridization. Herein we show that BSI can be used to study

67

the impact of surface-immobilization and fluorophore labeling on DNA strand hybridization in a user-friendly format that is likely to be broadly applicable to a range of biomolecular interactions.

4.2 Materials & Methods

4.2.1 Oligonucleotide Preparation

All oligonucleotides were purchased salt-free with PAGE purification from BioSynthesis, Inc. The static probe strand (P_s) was derived from the myosin binding region of the mouse actin gene (5'-ACTCATCGTACTCCTGCTTGCTGATCCACA-3'). This strand was also tagged with a 5' biotin for the surface studies. The mismatch strands contained a two base terminal mismatch (5'-**CA**TGGATCAGCAAGCAGGAGTACGATGAGT-3') or a two base internal mismatch (5'- TGTGGATCAGCAAG**AG**GGAGTACGATGAGT-3'). The complementary strand (5'-TGTGGATCAGCAAGCAGGAGTACGATGAGT-3') was then left unlabeled or 5' labeled with either FITC or Cy3. The nonsense strand consisted of a random non-complementary sequence (5'- GTGGTACATGCAGCAGAGGTAGCATGAGTA-3'). The lyophilized DNA was reconstituted in PBS 0.05% Tween 20 buffer pH 7.4 to a stock solution of 100 μM and the concentration double checked with UV absorbance at 260 nm. The extinction coefficients at 260 nm were provided by BioSynthesis Inc.

68

4.2.2 BSI Channel Preparation

In order to prevent nonspecific DNA interactions with the glass surface for free-solution studies, the channel was silanized. Prior to silanization, the channel was cleaned by soaking in concentrated H_2SO_4 for 60 minutes followed by a MQ-H_2O rinse and dried with compressed air.   This was followed by a 30 minute soak with 10% KOH in methanol, and a rinse with MQ-H_2O. The channel was then filled with 2% 3-mercaptopropyltriethoxysilane (MEPTES, ordered from Sigma Aldrich) in toluene and allowed to stand without drying out for 60 minutes. The channel was then rinsed with toluene, methanol, and MQ-H_2O to complete the silanization procedure.

The channel was prepared for surface-immobilization experiments by cleaning thoroughly with a 60 minute H_2SO_4 soak followed by a 30 minute 10% KOH in methanol soak. After rinsing with MQ-H_2O and drying with compressed air, the channel was silanized with a 60 minute 2% MEPTES in toluene soak followed by a toluene, methanol, and H_2O rinse and air dried.   This step was followed by 1 mM N-(γ-maleimidobutyryloxy)succinimide ester (GMBS, ordered from Sigma Aldrich) in absolute ethanol for 30 min.   Once again, the channel was rinsed with deionized water and dried before soaking in an ExtrAvidin (from Sigma Aldrich) solution (1 mg/mL) overnight.   Having coated the channel with ExtrAvidin the biotinylated P_s oligonucleotide (1 mg/mL) was immobilized onto the surface by soaking for 60 minutes (Fig. 4.1).
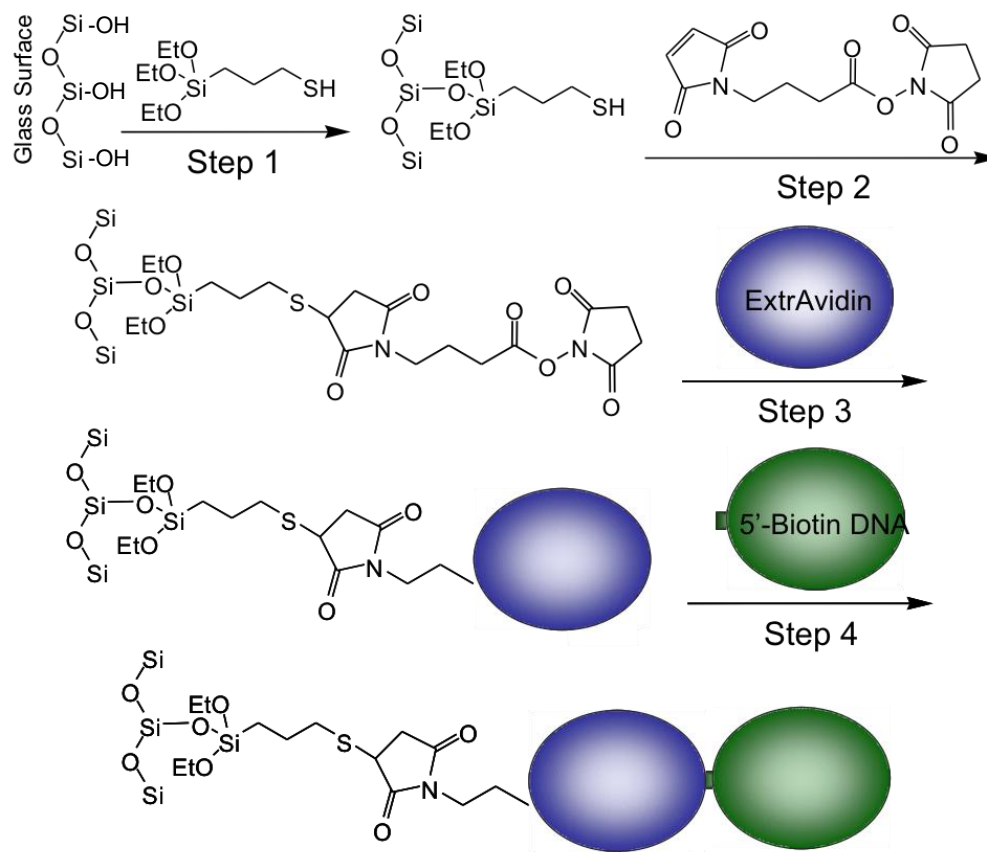
Figure 4.1 Schematic of biotin-Extravidin surface-immobilization procedure.

4.2.3 BSI Experimental Protocol

The HeNe laser and temperature controller were turned on an hour before the experiments were conducted to ensure equilibrium. Free-solution experiments were carried out by keeping P_s constant at 150 nM and varying its complementary or mismatched strand from 0-300 nM. The DNA samples were allowed to sit for several hours at room temperature prior to the experiment to allow for complete hybridization. Samples were introduced by pipetting 1 μL directly into the channel well using vacuum suction. Prior to each trial, buffer was rinsed through the channel until the signal

remained constant. Each trial consisted of a one minute recording of the signal at each concentration. The signal values from these trials were then averaged and plotted versus concentration. The final hybridization plot was obtained by subtracting out the blank, containing only 150 nM P_s, and taking the single stranded calibration into account. The corresponding curve was then fit to a one-site binding hyperbola model in Prism® to obtain K_D and standard error was determined in the curve fit analysis.

For the surface-immobilized BSI experiments, the single stranded oligomer was introduced into the prepared channel and the signal recorded for 1.5 minutes. Only the last 1000 data points were used in the average to ensure a uniform signal and avoid the signal change due to the hybridization event. After each hybridization event the channel was washed with 2 x 1μL 1M NaOH followed by 3 x 1μL MQ-H$_2$O to rinse away the previous strand. The next highest concentration was then added to the channel and the procedure repeated until all concentrations have been recorded. Data analysis was the same as for the free-solution since the signal average was recorded after hybridization occurred.

4.2.4 ITC Experimental Protocol

Experiments were carried out using a MicroCal VP-ITC. Before each experiment, the sample cell and syringe were cleaned with Contrad-70 and rinsed with MQ-H$_2$O and PBS with 0.05 % Tween 20 buffer. Prior to loading, solutions were degassed using a ThermoVac for 15 minutes. The reference cell was filled with thoroughly degassed MQ-H$_2$O and changed weekly. The sample cell was loaded with approximately 1.5 mL of 12.5 μM P_s oligomer and great care was needed to make sure no

air bubbles were introduced into the cell. The injection syringe was filled with 100 μM

of either the labeled, unlabeled, or mismatched strand and purged and refilled a couple of

times before proceeding to ensure a uniform sample. The temperature was kept at 21°C

and 5 μL injections were performed to a final volume of 250 μL. After a successful

experiment, the titrant was injected into buffer to obtain a heat of dilution. The heat of

dilution was then subtracted from the binding isotherm to obtain the final plot. This plot

was then fit using Origin® software to obtain K_D.

4.2.5 Measurement of Melting Temperature

Oligonucleotide melting temperature (T_m) experiments were carried out on a JASCO

CD Spectrophotometer. Samples were prepared by mixing equivolumes of 100 μM DNA

solutions and allowing them to hybridize for at least 1 hour. This solution was then

diluted to a final duplex DNA concentration of 5 μM. The temperature was increased

from 40-90 °C in 0.5 °C/minute increments and monitored at 260 nm to obtain a melting

profile (Fig. 4.2). T_m was calculated in Origin® (Microcal Version 5) as the derivative of

the melting curves and also by the baseline method.[21] Standard error was calculated from
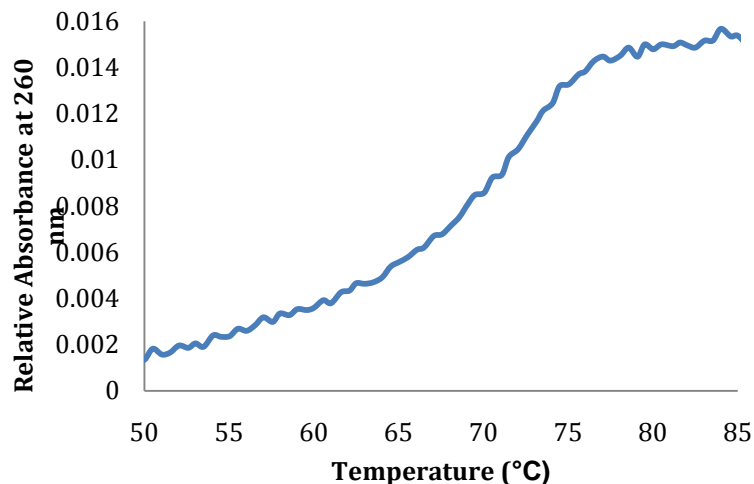
the average of 3 trials.

Figure 4.2 Representative melting profile of oligonucleotide absorbance hyperchromicity with increasing temperatures.

4.2.6 Fluorescence Microscopy

Fluorescence microscopy was employed to validate oligonucleotide immobilization and determine an effective washing procedure to remove the hybridized strand. All experiments were carried out on a Nikon Eclipse E800 microscope with a HBO 103/2 short arc mercury bulb. An excitation wavelength of 450-490 nm was used for the FITC (emission at 525 nm) while Cy3 was excited at a wavelength of 546 nm to emit at 568 nm. For these experiments, 200 nM FITC and Cy3 labeled oligonucleotides were used to illuminate the channel of a P_s modified channel and an unmodified negative control channel. Photos of the channels were used to compare the fluorescence intensity of the modified and unmodified channel with 1) 200 nM probe strand present, 2) empty channel after probe strand introduction and 3) buffer-filled channel after 3x1 µL buffer rinses. This experiment showed little fluorescence intensity for the negative control after the 200 nM target strand was removed from the channel and no intensity after buffer

rinses. However, the P_s-modified channel exhibited high fluorescence intensity with the empty channel and after buffer rinses, signifying a successful immobilization procedure. The next portion of these experiments was aimed at determining an appropriate wash procedure that effectively removed the complementary target strand while keeping P_s surface chemistry intact. Again this experiment was done by comparing the fluorescence intensity of photos before and after the wash procedure and repeating the measurements in the same channel to ensure P_s immobilization. Several wash procedures were evaluated including, concentrated urea, guanidinium hydrochloride, heated 50% dimethyl sulfoxide (DMSO):H_2O, and several concentrations of NaOH in H_2O. After all of these experiments were examined, the best wash procedure was determined to be washes with 2 x 1μL 1M NaOH followed by 3 x 1 μL MQ-H_2O. The effectiveness of this procedure was confirmed by the absence of fluorescence after 200 nM oligonucleotide introduction and washing. This procedure kept the surface intact as shown by a similar fluorescence after the re-introduction of 200 nM oligonucleotide even after buffer rinses.

4.2.7 Data Analysis

End-point determination of K_D is ideal since all measurements are taken after the binding complex is already formed. The law of mass action provides equation 1:

$$[R \bullet L]_\infty = \frac{[R]_0 \cdot [L]_0}{[L]_0 + K_D} \tag{1}$$

where $[R]_0$ is the initial macromolecule concentration, $[L]_0$ is the initial ligand concentration, and $[R \cdot L]_\infty$ equals the receptor-ligand concentration at equilibrium. The

data was fit in Prism$^{\circledR}$ using the one site binding function to elucidate K_D from a plot of signal vs. $[L]_0$.

4.3 Results & Discussion

4.3.1 Free-solution oligonucleotide hybridization and stability studies

Initiation of the free-solution BSI oligonucleotide experiments began with a duplex calibration to determine an appropriate concentration range that provides an adequate fringe shift when compared to buffer alone. For this experiment, the unlabeled strand was mixed with an equimolar complementary probe strand (P_s), allowed to hybridize, and serially diluted to a range of duplex concentrations from 0-200 nM (Fig. 4.3). 150 nM was chosen as the constant strand concentration based on the magnitude of the signal shift and comparability to surface-immobilized studies. Additionally, all of the steady-state, free-solution BSI experiments were performed in silanized channels to prevent non-specific oligonucleotide absorption to the surface. Non-specific absorption was noted by poor reproducibility in trials run without channel silanization, due to increasing DNA absorption onto the surface as the concentration was increased.
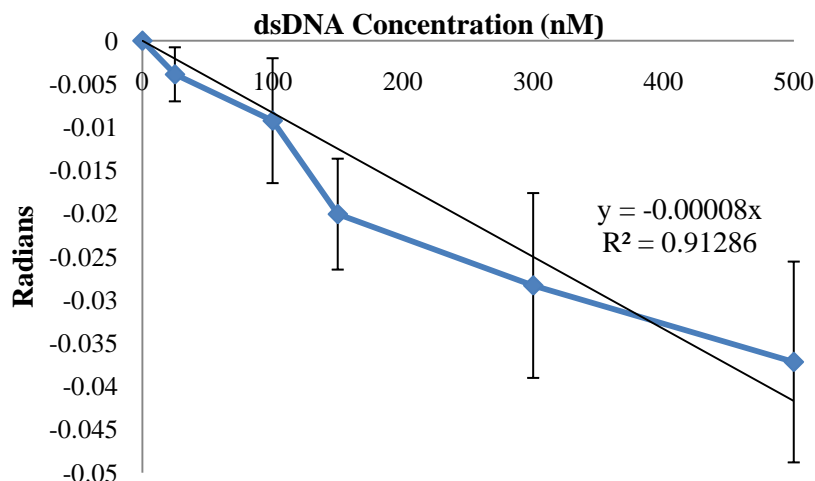
Figure 4.3 Free-solution BSI of unlabeled oligonucleotide duplex calibration shows that as the duplex concentration increases the radian shift decreases.

After an appropriate concentration range was determined for the free-solution BSI experiments, a single-stranded oligonucleotide calibration was performed to assess the signal shift from the single strand alone. This calibration, shown in Figure 4.4, provides a small linear increase due to increasing single strand concentration. This change is minimal when compared to the unlabeled oligonucleotide hybridization curve (Fig. 4.6) but must be taken into consideration for the final hybridization binding curve. These calibration curves were carried out for each strand and considered negligible or subtracted from the hybridization data to obtain the final oligonucleotide hybridization binding curve. The hybridization experiment was run by mixing 300 nM P_s with equal volume of serially-diluted complimentary or mismatched strands ranging from 0-600 nM. These samples were allowed to hybridize at room temperature before being introduced into the channel and recording the signal for 60 seconds. The averaged signal from each sample was then normalized by subtracting out the blank (containing 150 nM P_s in

buffer) and the calibration data, and plot versus ssDNA concentration (Fig. 4.5). These curves were then fit to a one-site binding hyperbola to obtain K_D.[18]
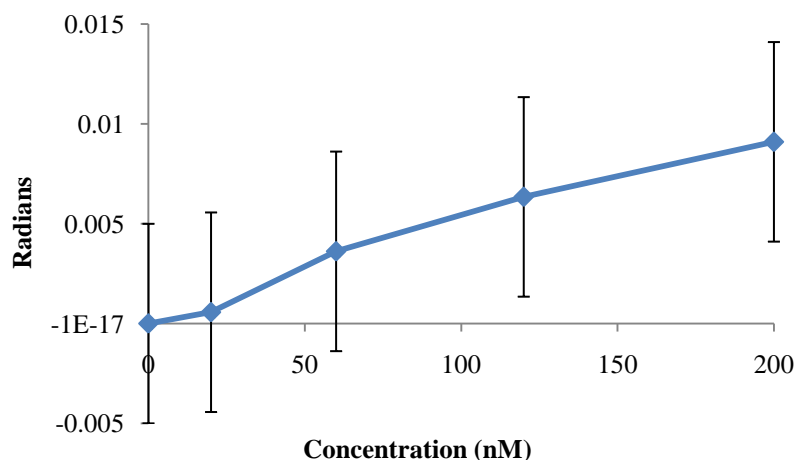

Figure 4.4 Single stranded unlabeled oligonucleotide calibration curve.

The free-solution BSI oligonucleotide hybridization experiments shown graphically in Figure 4.5 (individual binding curves in Fig. 4.6 - 4.11) and numerically in Table 4.1 provide interesting results. The presence of either fluorescent tag provides a modest stabilization of the duplex as shown by a lower K_D. These results are in agreement with previously published reports that show both 5'-Cy3[8] and FITC[9] lead to duplex stabilization with both labels significantly lowering ΔG. Furthermore, Norman *et. al*. have shown that when the Cy3 fluorophore in a 5'-labeled duplex is positioned on the end of the helix, it mimics the addition of another base pair, thus increasing duplex stability.[22] In comparison to the perfect complement, the terminal CA/AC mismatch has a negligible effect on duplex stability whereas the internal AG/GT mismatch has a deleterious impact on DNA hybridization. These results are consistent with previous

reports showing that stable terminal mismatches have a negligible impact on hybridization whereas internal mismatches significantly perturb hybridization.[23, 24]
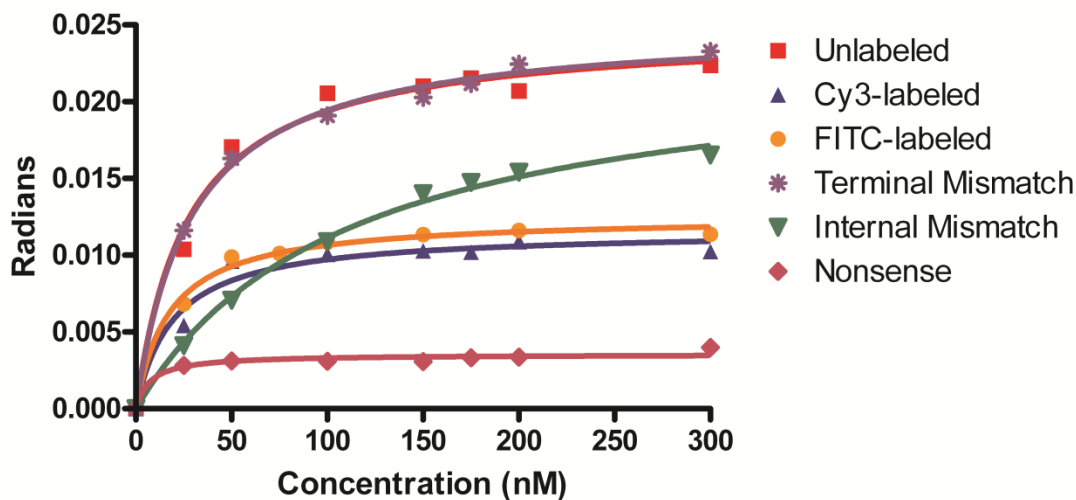

Figure 4.5 Free-solution BSI binding curves. Average plots of oligonucleotide hybridization at equilibrium with a constant probe strand (P_s) oligomer concentration of 150 nM and a varied concentration (0-300 nM) of unlabeled (■), Cy3-labeled (▲), FITC-labeled (●), terminal (*) or internal mismatched(▼), or nonsense strand(♦). (See Table 4.1 for corresponding K_D values)
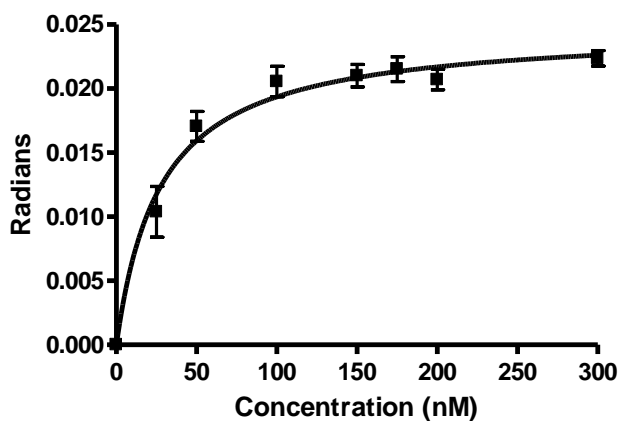

Figure 4.6 Free-solution BSI of unlabeled oligonucleotide hybridization with error bars from 7 trials. Curve fitting provided a K_D of 27.5 ± 4.7 nM with an R^2 of 0.9867.

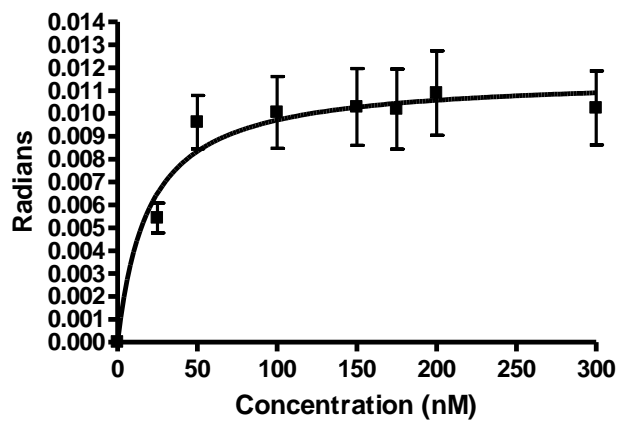**Figure 4.7** Free-solution BSI of Cy3-labeled oligonucleotide hybridization with error bars from 7 trials. Curve fitting provided a K_D of 19.6 ± 5.8 nM with an R^2 of 0.965.

Figure 4.8 Free-solution BSI of FITC-labeled oligonucleotide hybridization with error bars from 7 trials. Curve fitting provided a K_D of 17.4 ± 2.9 nM with an R^2 of 0.9896.

Figure 4.9 Free-solution BSI of terminal mismatched oligonucleotide hybridization with error bars from 7 trials. Curve fitting provided a K_D of 28.9 ± 2.4 nM with an R^2 of 0.9966.
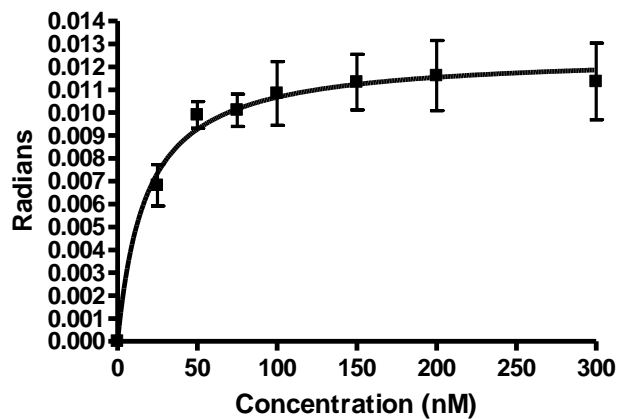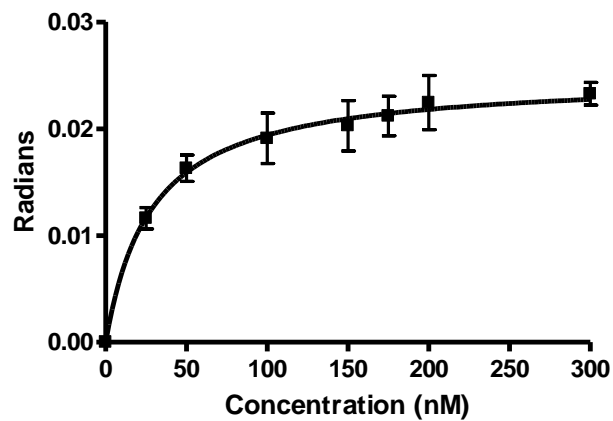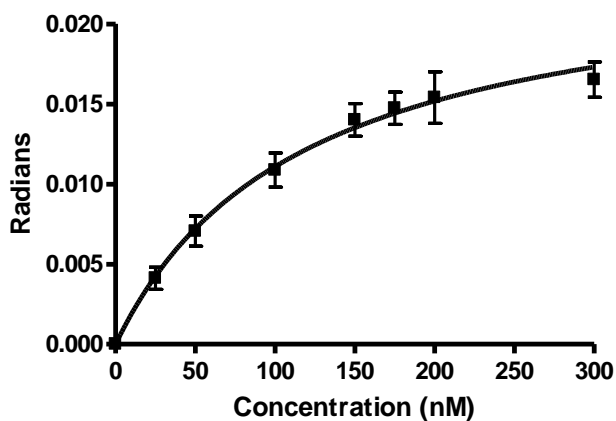

Figure 4.10 Free-solution BSI of internal mismatched oligonucleotide hybridization with error bars from 10 trials. Curve fitting provided a K_D of 110.4 ± 11.6 nM with an R^2 of 0.996.
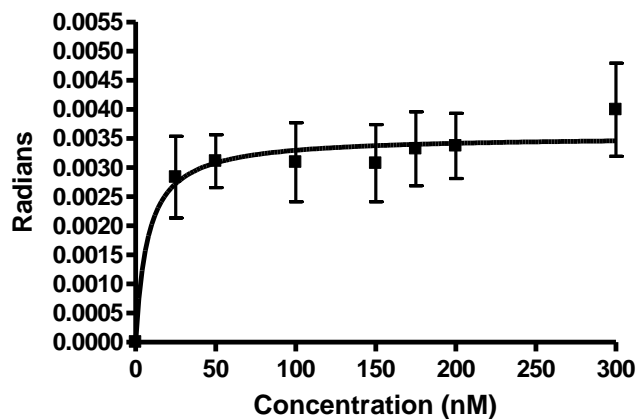
Figure 4.11 Free-solution BSI of nonsense oligonucleotide hybridization with error bars from 7 trials. Data show a slight increase in signal due to an increase in oligonucleotide concentration, however the signal shift is negligible in comparison to complementary oligonucleotide hybridization. Curve fit analysis provided a poor fit with an r^2 value of 0.33.

Table 4.1 K_D values and standard error of free-solution BSI, surface-immobilized BSI, and ITC with corresponding melting temperature (T_m) values

DNA strand	Free-Solution BSI K_D (nM)[a]	Surface-Immobilized BSI K_D (nM)[a]	ITC K_D (nM)	$T_m{}^b$ (°C)	$T_m{}^c$ (°C)
Unlabeled	27.5 ± 4.7	66.1 ± 8.4	38.8 ± 4.3	74.4 ± 0.3	72.2
Cy3-labeled	19.6 ± 5.8	41.7 ± 6.3	17.2 ± 1.5	74.1 ± 0.1	-
FITC-labeled	17.4 ± 2.9	45.6 ± 7.7	10.6 ± 1.8	75.2 ± 0.5	-
Terminal Mismatch	28.9 ± 2.4	60.7 ± 7.9	-	73.1 ± 0.3	71.8
Internal Mismatch	110.4 ± 11.6	132.5 ± 16.6	-	67.5 ± 0.2	66.7

[a]Curve fits were carried out on an average plot from at least 5 separate trials to ensure reproducibility [b]Experimental T_m from absorbance hyperchromicity [c]Calculated T_m from DINAMelt two-state hybridization model.[25]

ITC was employed to validate the BSI free-solution results. The K_D values from these experiments are included in Table 4.1 with binding curves shown in Figures 4.12 through 4.14. The K_D values from the ITC results were within the standard deviation of the free-solution BSI, therefore confirming the utility of free-solution BSI. The relative binding affinity for each oligonucleotide was confirmed using ITC, with the slight variations in the binding constant due to differences in the concentration used for ITC versus BSI. Unfortunately the ITC results for both of the mismatched oligonucleotides were irreproducible. Several mismatched ITC experiments were carried out but there was no correlation between the trials. The variability in the mismatched ITC results is attributed to different conformational structures that can be formed during mismatch hybridization,[26, 27] thus disrupting the equilibrium throughout the course of the experiment.

Figure 4.12 Final ITC plot for unlabeled oligonucleotide hybridization. Curve fitting with a one-site binding model provided a K_D of 38.8 ± 4.3 nM, ΔH of -195 ± 1.2 kcal/mol, and ΔS of -627 ± 49 cal/mol K.

Figure 4.13 Final ITC plot for Cy3-labeled oligonucleotide hybridization. Curve fitting with a one-site binding model provided a K_D of 17.2 ± 1.5 nM, ΔH of -187 ± 1.4 kcal/mol, and ΔS of -599 ± 52 cal/mol K.
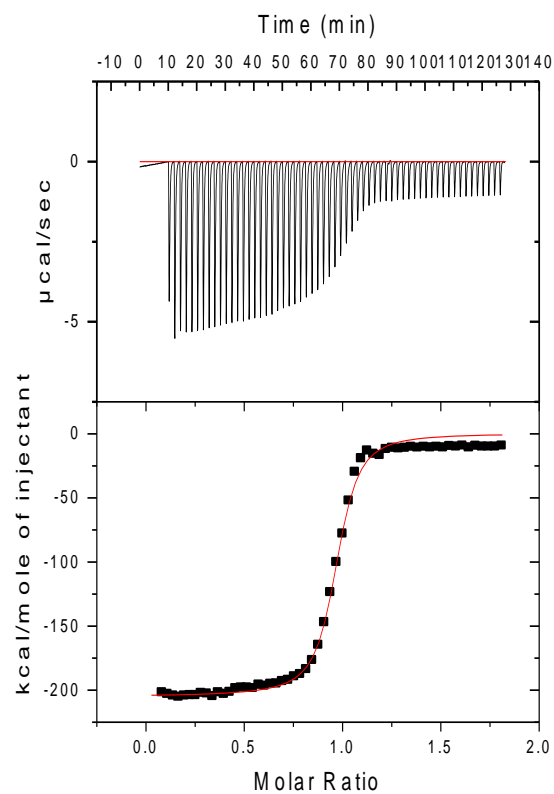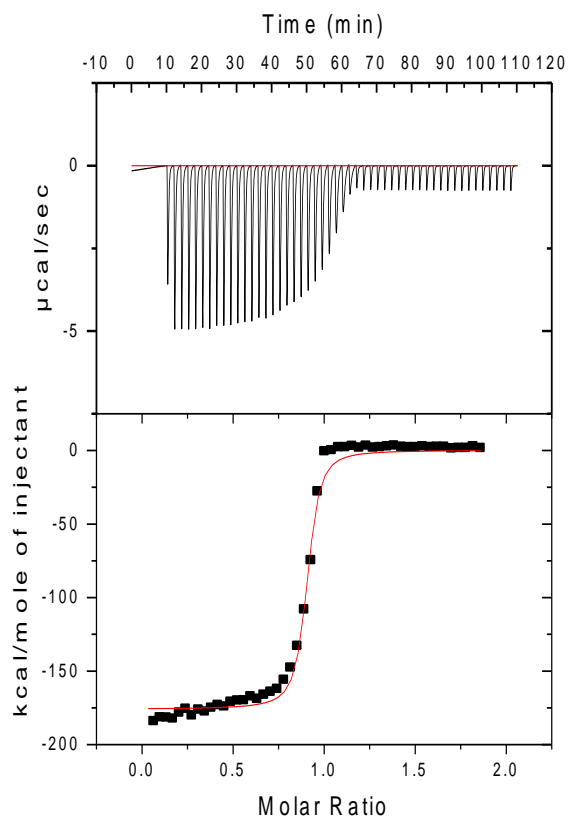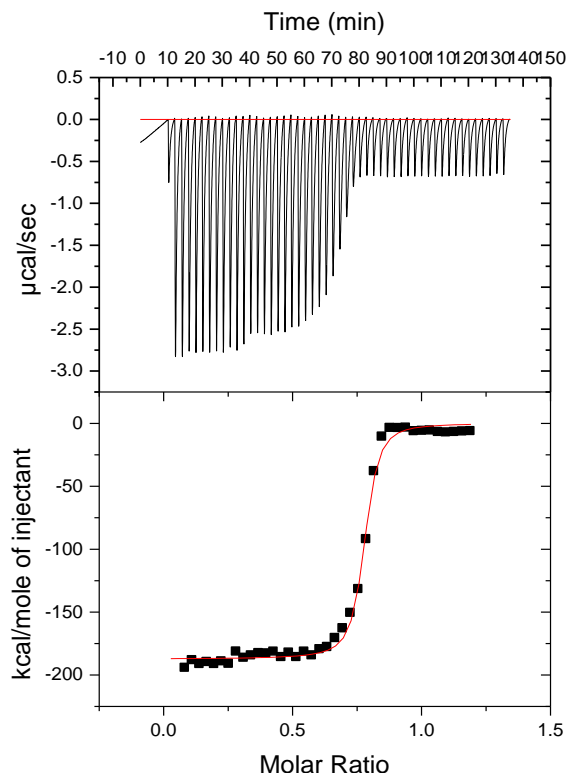
Figure 4.14 Final ITC plot for FITC-labeled oligonucleotide hybridization. Curve fitting with a one-site binding model provided a K_D of 10.6 ± 1.8 nM, ΔH of -188 ± 1.3 kcal/mol, and ΔS of -602 ± 2 cal/mol K.

Melting studies were carried out to obtain the T_m to compare the BSI free-solution data with a widely used method for determining duplex stability (Fig. 4.15 and Table 4.1). It is important to note that direct comparison between T_m and K_D (ΔG) can be inaccurate when assuming a two-state model for oligomers over 14 bases long.[28] As a consequence, the K_D of a duplex at room temperature may not correlate with T_m. Although the Cy3 and FITC labels lower the K_D of hybridization as determined by BSI, their impact on duplex melting is small and within experimental error as shown by the relatively small change in T_m. Studies on mismatches show lower melting temperatures

than the perfect complement with a modest decrease in T_m for the terminal mismatch and a significantly lower T_m for the internal mismatch. Nearest neighbor calculations used to estimate the T_m for the complementary strand and mismatches correlate well with the experimentally determined T_m values.[25] Comparison of data obtained from BSI are consistent with T_m values with the terminal mismatch showing a slightly lower T_m and slightly higher K_D in comparison to the perfect complement and the internal mismatch with a T_m five degrees lower than the perfect complement.
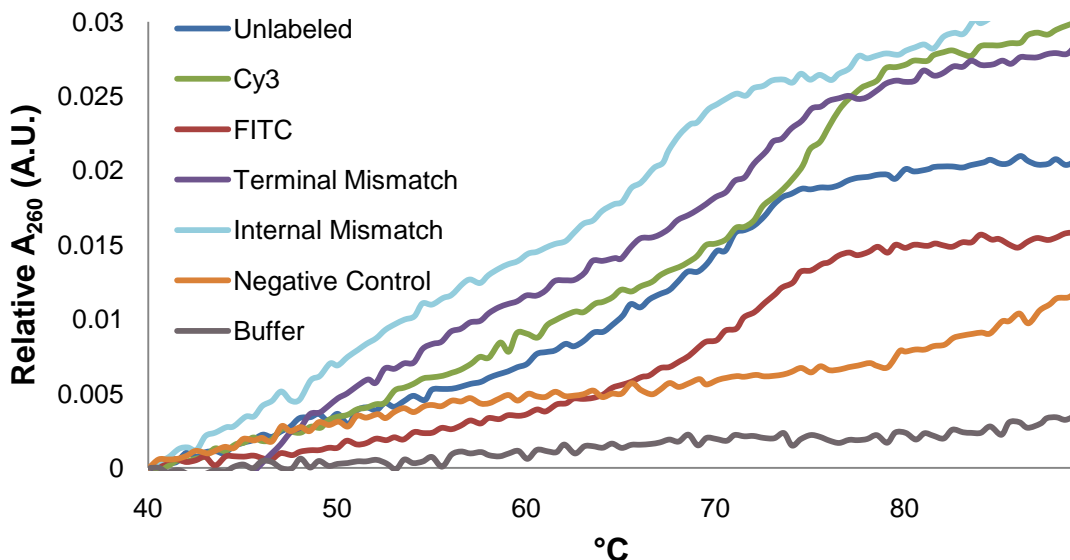
Figure 4.15 Absorbance hyperchromicity melting profiles of labeled, unlabeled, mismatched, and negative control oligonucleotides. Individual T_m values can be found in Table 4.1.

Calculations were carried out to correlate the T_m values to the BSI and ITC results. The Gibbs free energy equation (eqn 2) shows the relationship between K_a, ΔH, and ΔS. The K_a value is taken from the free-solution BSI values ($1/K_D$) at 298K.

$$\Delta G° = -RT\ln K_a = \Delta H° - T\Delta S°\tag{2}$$

Equation 2 can be re-written (eqn 3) which will produce a straight line when plot as of ln(K_D) vs. $1/T_m$ (Fig 4.16).

$$lnK_a = -\frac{\Delta H^\circ}{R \cdot 298K} + \frac{\Delta H^\circ}{R \cdot T_m} \tag{3}$$

Analysis of the linear relationship in Figure 4.16 produces ΔH° values of -230.4 kJ/mol and -189.8 kJ/mol from the slope and y-intercept, respectively.
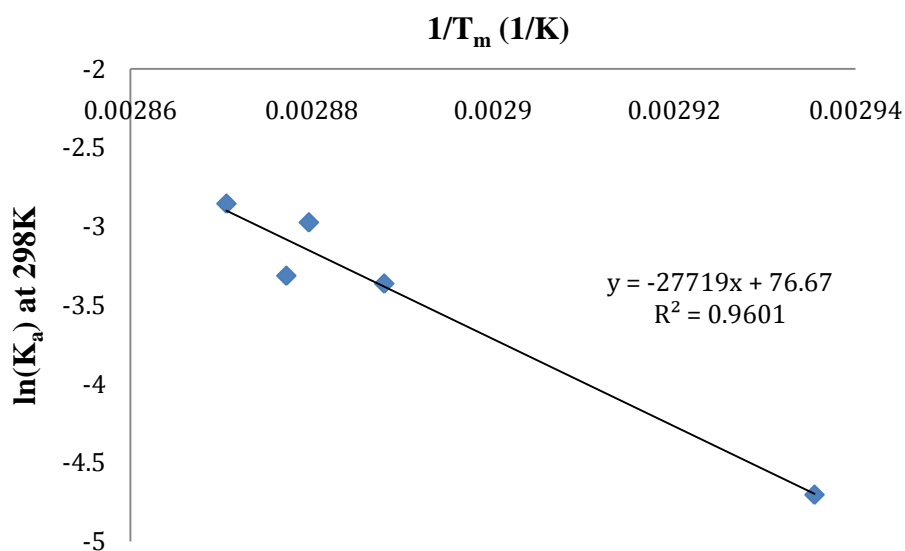
Figure 4.16 Relationship between ln(K_a) and $1/T_m$ for each oligonucleotide duplex used to determine the ΔH via equation 3.

4.3.2 Surface-immobilized BSI oligonucleotide hybridization

Next, the impact of surface immobilization on hybridization was examined. Surface-immobilized BSI experiments were carried out by immobilizing ExtrAvidin to the glass surface and reacting with the biotinylated P_s oligonucleotide. The lowest concentration of the target strand was then introduced into the channel and the signal recorded for 1.5 minutes. After the first 40 seconds the signal leveled out, signifying the

hybridization was complete (Fig. 4.17).   However, only the last 30 seconds (approximately 1000 data points) were used in the average to ensure the system was at equilibrium. It is also important to note that the unlabeled concentration in Figure 4.17 is the lowest concentration used for these studies, therefore all other concentrations equilibrate faster.   After each hybridization event, the channel was washed with 2 x 1µL 1M NaOH followed by 3 x 1µL MQ-H$_2$O to rinse away the previous strand. Subsequent experiments of increasing concentration of DNA were performed using an identical procedure.
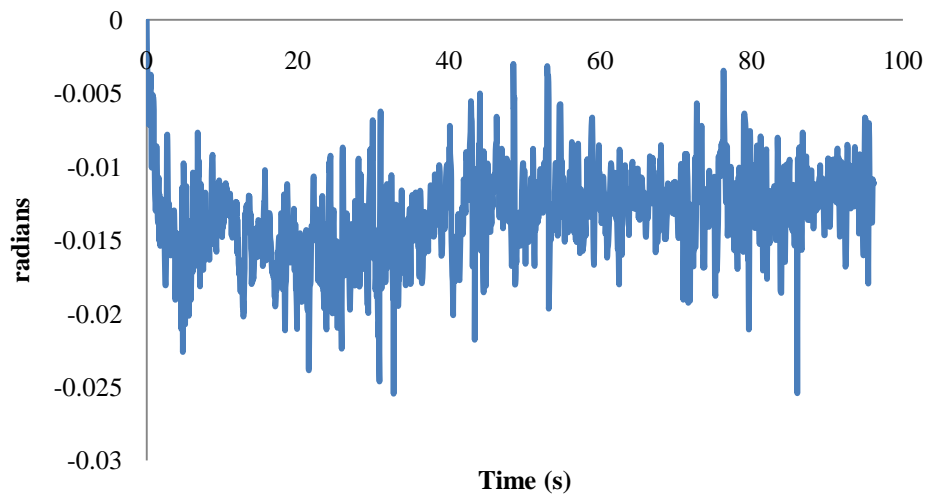
Figure 4.17 Normalized BSI signal versus time for the hybridization of 10 nM unlabeled to the surface-immobilized complementary strand. The data shows equilibration by 40 seconds with only the last 30 seconds used for the average in steady-state analysis.

The immobilization and wash procedure was validated by fluorescence microscopy with the use of the Cy3- and FITC-labeled oligonucleotides to ensure proper P$_s$ immobilization and target strand removal without perturbing the surface preparation (Fig. 4.18). For this experiment the channel was prepared to immobilize the P$_s$ strand and

200 nM of either Cy3- or FITC-labeled complementary oligonucleotides were introduced into the channel. Bright fluorescence intensity after buffer rinsing verified immobilization when compared to a negative control with no fluorescence intensity in an unmodified channel. An appropriate wash procedure was then determined by analyzing fluorescence intensity before and after the hybridization and washes. The optimal method is consecutive rinses of 2 x 1µL 1M NaOH followed by 3 x 1µL MQ-H$_2$O. A lack of fluorescence intensity after 200 nM oligonucleotide introduction and washing confirmed the effectiveness of this protocol. Additionally, this procedure kept the surface intact as shown by similar fluorescence intensity after the re-introduction of 200 nM oligonucleotide even after buffer rinses
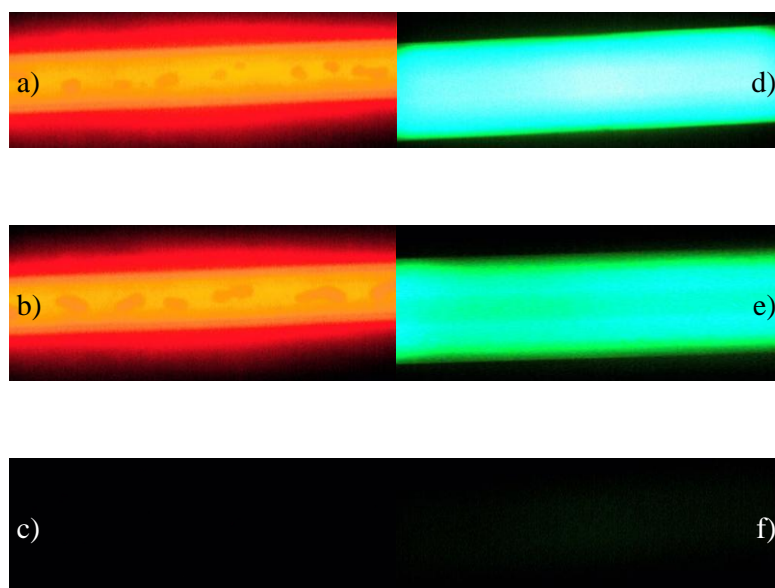
Figure 4.18 Fluorescence microscopy pictures of surface-immobilized oligonucleotide hybridization. a) Empty channel after 200 nM Cy3-labeled oligonucleotide introduction b) Empty channel after 200 nM Cy3 and 5 x 1 µL buffer rinse c) Empty channel after Cy3, buffer rinse, and wash procedure d) Filled channel with 200 nM FITC-labeled oligonucleotide taken after a previously performed wash procedure e) Buffer filled channel after 5 x 1 µL buffer rinse f) Buffer filled channel after FITC, buffer rinse, and wash procedure.

The binding curves were normalized by subtracting the buffer signal from the sample signals and plotted versus concentration of DNA (Fig. 4.19, with individual binding curves in Fig. 4.20-4.25). Data analysis of the equilibrium was carried out in the same manner as the free-solution experiments, using a one-site binding hyperbola. These plots show a clear saturation by 200 nM with the exception of the internal mismatch which required a slightly higher concentration to reach saturation. The internal mismatch also provided a marked signal increase in comparison to the other strands. It is possible that the presence of an internal mismatch skews the conformation of the duplex generating a greater signal shift. Smith and coworkers found that one-base bulges neighboring a mismatch can be present in several conformations, which can be easily interconverted.[26] It is our hypothesis that various conformations surrounding the internal two-base mismatch can influence the waters of hydration and thus lead to a greater radian shift when compared to complementary strands.
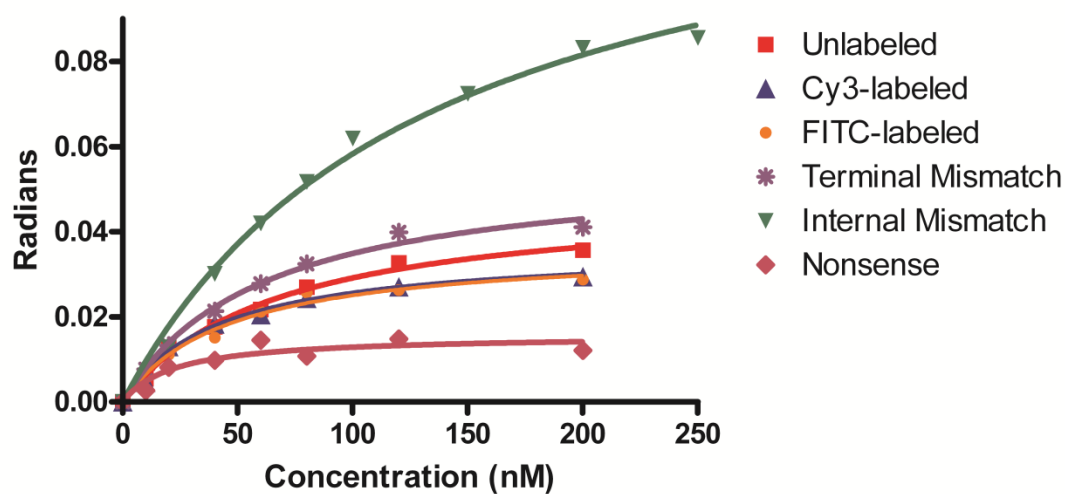
Figure 4.19 Surface-immobilized BSI binding curves. 5 trial average plots of hybridized unlabeled (■), Cy3-labeled (▲), FITC-labeled (●), terminal mismatch (*), internal mismatch (▼), and nonsense (♦) oligonucleotides ranging from 0-250 nM. (See Table 4.1 for corresponding K_D values)

Figure 4.20 Surface-immobilized BSI of unlabeled oligonucleotide hybridization with error bars from 6 trials. Curve fitting provided a K_D of 66.1 ± 8.4 nM with an R^2 of 0.9927.

Figure 4.21 Surface-immobilized BSI of Cy3-labeled oligonucleotide hybridization with error bars from 4 trials. Curve fitting provided a K_D of 41.7 ± 6.3 nM with an R^2 of 0.9885.
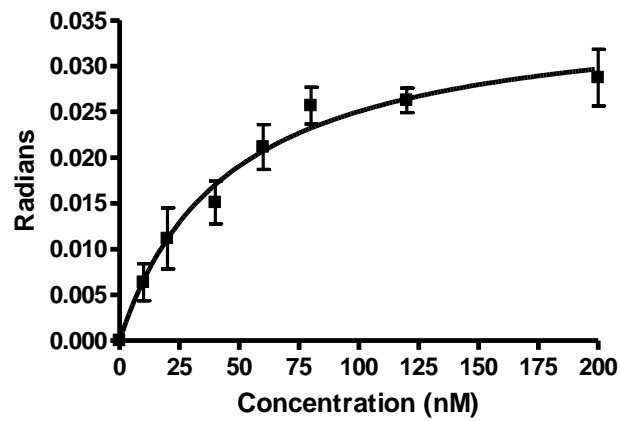
Figure 4.22 Surface-immobilized BSI of FITC-labeled oligonucleotide hybridization with error bars from 5 trials. Curve fitting provided a K_D of 45.6 ± 7.7 nM with an R^2 of 0.9854.
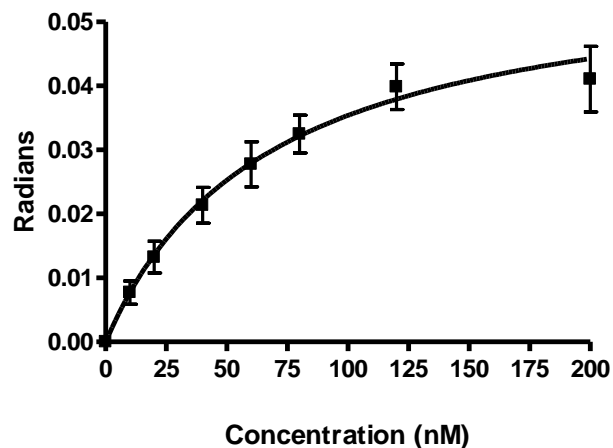
Figure 4.23 Surface-immobilized BSI of terminal mismatched oligonucleotide hybridization with error bars from 6 trials. Curve fitting provided a K_D of 60.7 ± 7.9 nM with an R^2 of 0.9922.
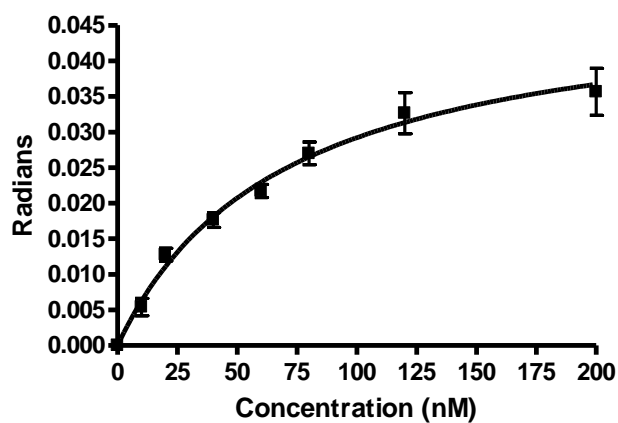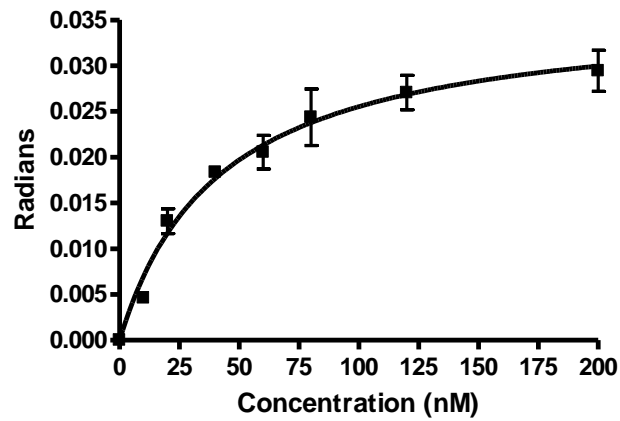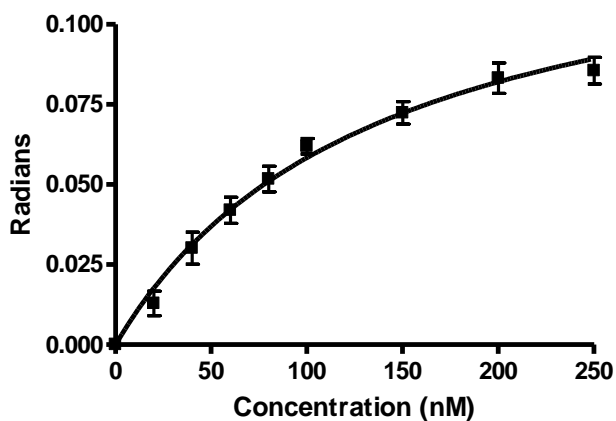

Figure 4.24 Surface-immobilized BSI of internal mismatched oligonucleotide hybridization with error bars from 7 trials. Curve fitting provided a K_D of 132.5 ± 16.6 nM with an R^2 of 0.9929.
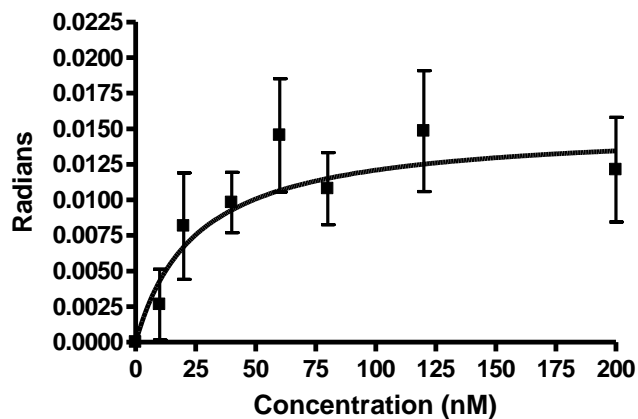
Figure 4.25 Surface-immobilized BSI of nonsense oligonucleotide hybridization with error bars from 6 trials. Data show a slight increase in signal due to an increase in oligonucleotide concentration, however the signal shift is negligible in comparison to complementary oligonucleotide hybridization. Curve fit analysis provided a poor fit with an r^2 value of 0.44.
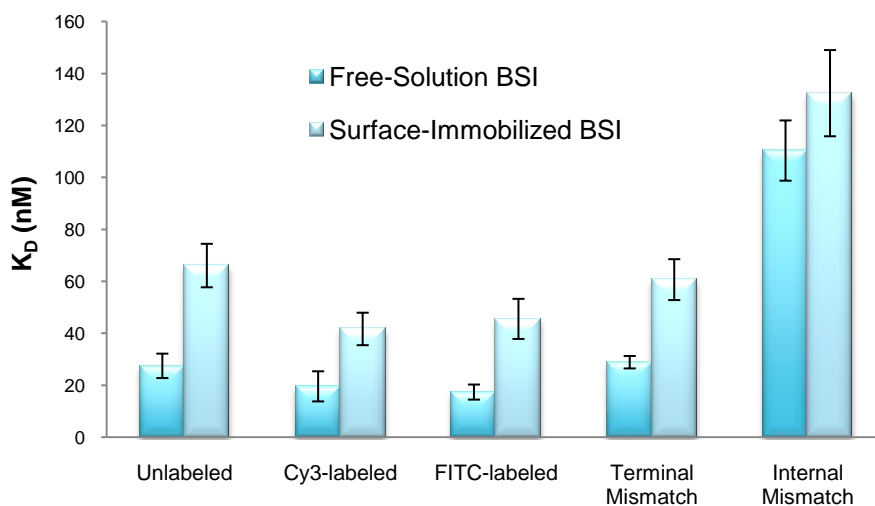
Figure 4.26 Graphical representation of free-solution vs. surface-immobilized oligonucleotide hybridization.

94

Results from these experiments show a significant perturbation in the hybridization affinity for surface-bound versus free-solution oligonucleotides (Table 4.1). These perturbations result in a drastic increase in K_D values by nearly 50% when compared to free-solution values (Fig. 4.26). It is important to note that while the surface-immobilized K_D values are substantially higher than free-solution, the relative order of stability of each pair remains the same. This finding suggests that although the absolute K_D values are perturbed in the surface-immobilized experiments, the trend in relative affinities remains the same. Comparison of free-solution and surface-immobilized BSI data show that the surface-bound experiments generate a greater signal shift. This observation is most likely due to differences in P_s concentration and potential variations in the dielectric constant[11] at the interface due to surface immobilization. Additionally, calculations were carried out with the surface-immobilized K_D values to correlate to the T_m values (refer to equation 3 and Fig 4.16). The ΔH° values found using this method were much lower (-133 and -105 kJ/mol) signifying a clear perturbation due to surface tethering.

4.4 Conclusion

Overall, these studies demonstrate that BSI provides a convenient approach for the study of DNA hybridization in free-solution and surface-immobilized formats. Results from these experiments show that: (1) A terminal fluorophore has a modest impact on DNA hybridization, (2) BSI can be used to distinguish between a perfect complement and a two-base-pair mismatch with an internal mismatch significantly

destabilizing the duplex, and (3) Surface immobilization significantly perturbs hybridization by as much as 50%.

The influence of terminal fluorophores and a two-base-pair terminal mismatch was shown to have a negligible or modest impact on hybridization of a 30-mer whereas a two-base-pair internal mismatch significantly destabilizes the duplex. The detection of mismatched base pairs is critical in biochemical research and medical diagnosis as medicine becomes more personalized. For example, single nucleotide polymorphisms (SNP) are very prevalent genetic mutations that can lead to disease. The detection of such mutations can be used for disease prevention, diagnosis, and prognosis. We have shown that BSI can detect a two-base internal mismatch, thus potentially providing another alternative to the detection of genetic mutations.

For the first time, a direct comparison of surface-immobilized and free-solution hybridization was carried out using the same technique. Comparison of both formats shows that surface immobilization significantly perturbs hybridization, altering K_D values by as much as 50%. While these results are very important, these experiments were only carried out with one surface-tethering technique. In practice, there are numerous methods used to immobilize DNA onto a surface, so it would be useful to extend this study to other surface-immobilizing protocols. The versatility of BSI allows both free-solution and surface-immobilized formats using a single-sensing platform, providing a simple and effective way to determine perturbations due to surface immobilization. This unique feature of BSI allows for direct comparison of both methods which can be easily adapted across multiple disciplines in the scientific community to determine perturbations due to surface-tethering.

4.5 References

(1) Ratilainen, T.; Holmen, A.; Tuite, E.; Haaima, G.; Christensen, L.; Nielsen, P. E.; Norden, B. *Biochemistry* **1998**, *37*, 12331-12342.

(2) Plum, G. E.; Breslauer, K. J. *Curr. Opin. Struct. Biol.* **1995**, *5*, 682-690.

(3) Marky, L. A.; Kallenbach, N. R.; McDonough, K. A.; Seeman, N. C.; Breslauer, K. J. *Biopolymers* **1987**, *26*, 1621-1634.

(4) Montrichok, A.; Gruner, G.; Zocchi, G. *Europhys. Lett.* **2003**, *62*, 452-458.

(5) Hradetzky, D.; Mueller, C.; Reinecke, H. *J. Opt. A: Pure Appl. Opt.* **2006**, *8*, S360-S364.

(6) Kim, D. K.; Kerman, K.; Saito, M.; Sathuluri, R. R.; Endo, T.; Yamamura, S.; Kwon, Y. S.; Tamiya, E. *Anal. Chem.* **2007**, *79*, 1855-1864.

(7) Daugherty, D. L.; Gellman, S. H. *J. Am. Chem. Soc.* **1999**, *121*, 4325-4333.

(8) Moreira, B. G.; You, Y.; Behlke, M. A.; Owczarzy, R. *Biochem. Biophys. Res. Commun.* **2005**, *327*, 473-484.

(9) Morrison, L. E.; Stols, L. M. *Biochemistry* **1993**, *32*, 3095-3104.

(10) Randolph, J. B.; Waggoner, A. S. *Nucleic Acids Res.* **1997**, *25*, 2923-2929.

(11) Piunno, P. A. E.; Watterson, J.; Wust, C. C.; Krull, U. J. *Analytica Chimica Acta* **1999**, *400*, 73-89.

(12) Watterson, J. H.; Piunno, P. A. E.; Wust, C. C.; Krull, U. J. *Langmuir* **2000**, *16*, 4984-4992.

(13) Stevens, P. W.; Henry, M. R.; Kelso, D. M. *Nucleic Acids Res.* **1999**, *27*, 1719-1727.

(14) Fotin, A. V.; Drobyshev, A. L.; Proudnikov, D. Y.; Perov, A. N.; Mirzabekov, A. D. *Nucleic Acids Res.* **1998**, *26*, 1515-1521.

(15) Wick, L. M.; Rouillard, J. M.; Whittam, T. S.; Gulari, E.; Tiedje, J. M.; Hashsham, S. A. *Nucleic Acids Res.* **2006**, *34*, e26.

(16) Shchepinov, M. S.; Case-Green, S. C.; Southern, E. M. *Nucleic Acids Res.* **1997***, 25*, 1155-1161.

(17) Peterson, A. W.; Heaton, R. J.; Georgiadis, R. M. *Nucleic Acids Res.* **2001***, 29*, 5163-5168.

(18) Bornhop, D. J.; Latham, J. C.; Kussrow, A.; Markov, D. A.; Jones, R. D.; Sorensen, H. S. *Science* **2007***, 317*, 1732-1736.

(19) Latham, J. C.; Stein, R. A.; Bornhop, D. J.; McHaourab, H. S. *Anal. Chem.* **2009***, 81*, 1865-1871.

(20) Kussrow, A.; Kaltgrad, E.; Wolfenden, M. L.; Cloninger, M. J.; Finn, M. G.; Bornhop, D. J. *Anal. Chem.* **2009***, 81*, 4889-4897.

(21) Breslauer, K. J. *Methods Mol. Biol.* **1994***, 26*, 347-372.

(22) Norman, D. G.; Grainger, R. J.; Uhrin, D.; Lilley, D. M. *Biochemistry* **2000***, 39*, 6317-6324.

(23) SantaLucia, J.,Jr; Hicks, D. *Annu. Rev. Biophys. Biomol. Struct.* **2004***, 33*, 415-440.

(24) Fish, D. J.; Horne, M. T.; Brewood, G. P.; Goodarzi, J. P.; Alemayehu, S.; Bhandiwad, A.; Searles, R. P.; Benight, A. S. *Nucleic Acids Res.* **2007***, 35*, 7197-7208.

(25) Markham, N. R.; Zuker, M. *Nucleic Acids Res.* **2005***, 33*, W577-81.

(26) Smith, A. L.; Cekan, P.; Brewood, G. P.; Okonogi, T. M.; Alemayehu, S.; Hustedt, E. J.; Benight, A. S.; Sigurdsson, S. T.; Robinson, B. H. *J Phys Chem B* **2009***, 113*, 2664-2675.

(27) Prive, G. G.; Heinemann, U.; Chandrasegaran, S.; Kan, L. S.; Kopka, M. L.; Dickerson, R. E. *Science* **1987***, 238*, 498-504.

(28) Mergny, J. L.; Lacroix, L. *Oligonucleotides* **2003***, 13*, 515-537.

Chapter 5

A novel approach to the study of small molecule, hydrogen-bonding interactions using back-scattering interferometry
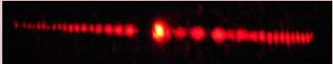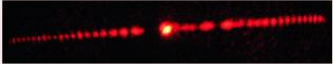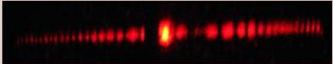
5.1 Introduction

Intermolecular interactions, especially those involving hydrogen bonds, drive the structure and function of macromolecules that catalyze reactions responsible for maintaining living systems.[1] In organic chemistry, hydrogen bonding partners have been utilized as the basis for approaches used to drive crystal formation, molecular recognition and catalysis.[2] Traditionally hydrogen bonding interactions are studied using isotope incorporation,[3, 4] NMR,[5] UV-Vis spectroscopy,[6] fluorescence,[7] and calorimetry.[8, 9] While these tools are widely used to characterize molecular interactions that arise through the formation of hydrogen bonds, they often require high substrate concentrations and volumes. Given the synthetic effort required to produce the components for the study of systems that utilize hydrogen bonds for recognition and catalysis, it is desirable to be able to study interactions using small quantities of substrates. Additionally, many of these systems have high affinity interactions with slow kinetics that cannot be studied using present techniques, such as ITC.[10] Recently back-scattering interferometry (BSI) has been shown to effectively determine the binding affinity of several biomolecular interactions ranging from interactions with proteins[11-13] to DNA-DNA hybridization.[14] The key features of BSI that make it appealing for the study of intermolecular interactions are the small sample sizes (pL to µL range), concentrations (nM to µM) and ability to carry out experiments without pre-functionalization or surface immobilization

of one of the binding partners.[11] To date, BSI has been employed in aqueous systems where one or more of the components are macromolecules. Given the importance of hydrogen bonding in non-aqueous media, we posed the following questions: 1) Can BSI be used to study hydrogen bonding in non-aqueous media? 2) What are the limits of detection in a non-aqueous environment when the binding partners are small molecules? 3) Can BSI be used to distinguish between similar hydrogen bonding partners? Herein we show that BSI can be used to study the interaction of diphenyl ureas and thioureas with benzoate in acetonitrile (MeCN) at concentrations several orders of magnitude lower than other commonly utilized techniques.

   To extend the use of BSI to other media, the solvent of choice must generate a high contrast fringe pattern in the glass chip. The fringe pattern is produced by constructive and destructive interference due to the refraction of light in different media (refer to Fig 1.4). If the RI of the solvent is similar to that of the substrate (i.e. glass) then the light will encounter minimal refraction when it passes through channel producing less interference of the light resulting in a poor fringe pattern. Therefore, the RI of the solvent must be different from the RI of glass in order to obtain a satisfactory fringe pattern that extends well beyond the centroid Table 5.1 lists the refractive indices of glass and several commonly employed solvents, many of which produce fringe patterns that meet the requirements of BSI analysis. The fringe patterns below exemplify the importance of solvent RI on the ability to produce high contrast fringe patterns. For example, dimethylsulfoxide (DMSO), has a RI fairly close to that of glass, resulting in a fringe pattern that does not extend beyond 2-3 fringes past the centroid. Since Fourier transform analysis typically utilizes fringes 4-8, these solvents are not compatible with

BSI in glass chips. However, one possible alternative could be the use of high refractive index, transparent coatings such as TiO_2.

Table 5.1 Refractive index of several solvents at 25 °C.[15]

Solvent	n_D	Fringe Pattern
Methanol	1.326	
Water	1.332	
Acetonitrile	1.342	
Acetone	1.357	
Tetrahydrofuran	1.404	
Dichloromethane	1.424	
Chloroform	1.444	
Dimethylsulfoxide	1.476	
Glass	1.517	n/a

To determine if this technique can be extended to studies in organic solvents, we examined the complexation of tetramethylammonium benzoate (TMAB) with 1,3-diphenyl urea (DPU), 1,3-diphenylthiourea (DPTU), 1,3-bis(p-nitrophenyl)urea (DNPU), and 1,3-bis(p-nitrophenyl)thiourea (DNPTU) in MeCN (Fig 5.1). MeCN was chosen as the solvent for this system because it has a refractive index fairly close to water and it generates a high contrast fringe pattern similar to water (Table 5.1). Additionally, all of

the substrates were soluble in MeCN, allowing for sufficient concentrations (low mM range) necessary for ITC analysis. Throughout the course of this study, BSI was found to be an efficient method for the study of small molecule interactions, especially when compared to other free-solution techniques such as calorimetry.
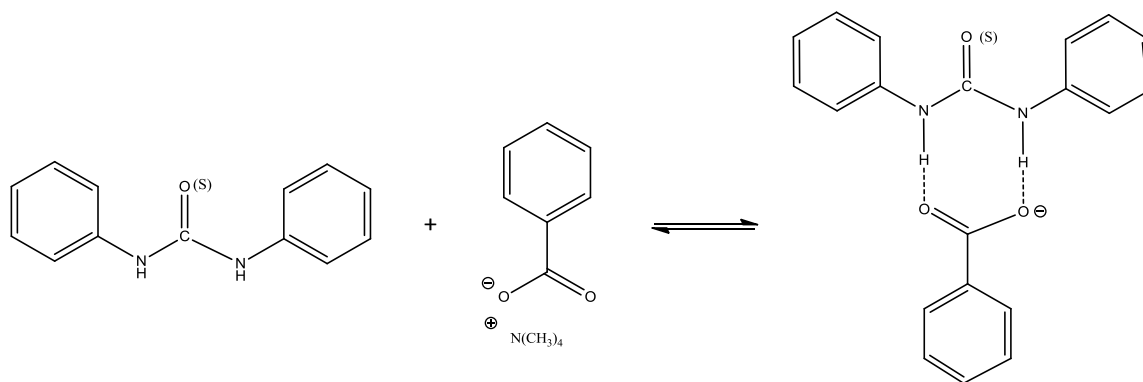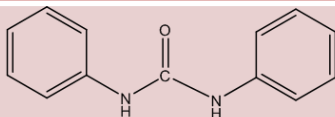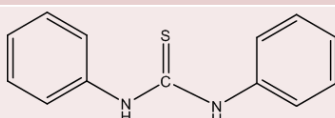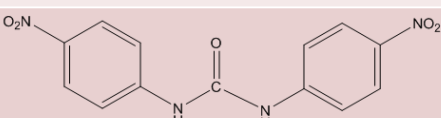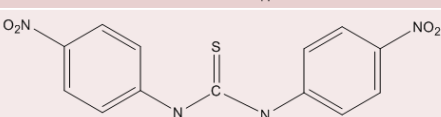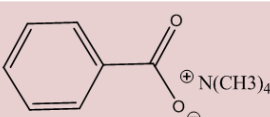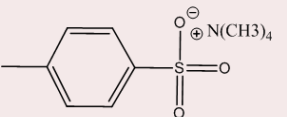
Figure 5.1 Structural representation of DPU or DPTU binding to TMAB. DNPU and DNPTU contain *para*-substituted nitro groups on both phenyl rings of urea/thiourea.

Urea and thiourea have been widely studied in molecular recognition because of their ability to form strong hydrogen bonds.[16, 17] Hydrogen bonding through urea and thiourea derivatives is used to recognize carboxylic acids, sulfonic acids, and nitrates.[18-20] Ureas and thioureas also act as acid catalysts in a variety of organic reactions including the Diels-Alder reaction and Claisen rearrangement.[21-23] In addition, these catalysts are very useful in diastereo- and enantioselective reactions.[3] As a result, the strength of the interaction between substrate and catalyst is important information for a synthetic chemist intending to utilize such transformations. The results discussed below demonstrate how BSI can be used to determine the affinity of small molecule

interactions on a microscale with commonly employed urea and thiourea derivatives (Table 5.2).

Table 5.2 Chemical name, abbreviation, and structure of hydrogen bonding partners.

Chemical Name	Abbreviation	Structure
Diphenylurea	DPU	
Diphenylthiourea	DPTU	
1,3-Bis(*p*-nitrophenyl) urea	DNPU	
1,3-Bis(*p*-nitrophenyl) thiourea	DNPTU	
Tetramethylammonium benzoate	TMAB	
Tetramethylammonium *p*-toluene sulfonate	TMAS	

5.2 Materials & Methods

5.2.1 Synthesis and Preparation

DPU, DPTU, benzoic acid, tetramethylammonium hydroxide were purchased from Sigma-Aldrich. TMAB was prepared by acid-base titration of benzoic acid and tetramethylammonium hydroxide in methanol followed by drying under high-vacuum.

The purity was verified with NMR (see section 5.5 for spectral data). DNPU and DNPTU were synthesized according to previously published procedures[23] from the reaction of *p*-nitroaniline with 4-nitrophenyl isocyanate and 4-nitrophenyl isothiocyanate, respectively. These syntheses were carried out with a 10mmol scale of equimolar concentrations of *p*-nitroaniline and either 4-nitrophenyl isocyanate or 4-nitrophenyl isothiocyanate. The reactions were performed in 15 mL benzene and flushed with N_2 throughout the reaction. Synthesis of DNPTU required refluxing overnight whereas DNPU formed within 3 hours. The crude products were recrystallized in aliquots from ethanol due to limited solubility. Purified DNPU/DNPTU were then dried under reduced pressure and analyzed with NMR (See Section 5.5). TMAS was synthesized by titrating *p*-toluene sulfonic acid with tetramethylammonium hydroxide in MeCN. Intermolecular association experiments were carried out in anhydrous MeCN.

5.2.2 BSI Experimental Protocol

The HeNe laser and temperature-controller were turned on at least an hour before the experiments were conducted to ensure equilibrium. Steady-state experiments were carried out by holding one binding partner (urea or thiourea) at a constant concentration while varying the concentration of the other (TMAB). These concentrations depended on the binding strength of the binding partners with higher affinity interactions requiring lower concentrations and vice versa. The samples were mixed and allowed to reach equilibrium (generally allowing the solution to stand for several hours) prior to running the experiment. The experiment for TMAB-DNPU/DNPTU required silanization of the channel prior to the experiment because the DNPU/DNPTU had a high affinity for

hydrogen bonds and interacted with the unmodified glass surface. Each channel was silanized by carrying out the following procedure: 1) 60 minute soak with concentrated H_2SO_4 2) 30 minute soak with 10% KOH in methanol 3) 60 minute soak with 2% MEPTES (3-mercaptopropyltriethoxysilane) in toluene. Steps 2 & 3 above involve volatile solvents; therefore the solutions must be replaced every few minutes to prevent drying out of the channels. Samples were introduced by pipetting 1 µL directly into the channel well and using vacuum suction (refer to Fig 2.2). Prior to each trial, MeCN was rinsed through the channel until the fourier transform and corresponding signal remained constant. Each trial consisted of a 45 second recording of the signal at each concentration. The signal values from these trials were then averaged and plot versus concentration. The calibration curve of the varied ligand was then subtracted from the binding data to generate the final plot.

5.2.3 ITC Experimental Protocol

Intermolecular binding experiments were carried out for all systems using a MicroCal VP-ITC. Before each experiment, the sample cell and syringe were cleaned and thoroughly rinsed with MeCN. Prior to loading, solutions were degassed using a ThermoVac for 8 minutes. The reference cell was filled with thoroughly degassed MeCN and changed every week. The sample cell was loaded with approximately 1.5 mL of either the urea or thiourea derivatives at 0.5 mM for DPU/DPTU and 0.2 mM for DNPU/DNPTU. The injection syringe was filled with 5 mM TMAB for interactions with DPU/DPTU and 2 mM for interactions with DNPU/DNPTU. The ITC experiments required higher concentrations for the interaction of DPU with TMAS, performed with

1mM DPU in the sample cell and 10mM TMAS in the syringe. For all ITC experiments, the temperature was kept at 25ºC and titrations were performed with 8 µL injections. After a successful experiment, the ligand was injected into MeCN to obtain a heat of dilution. The heat of dilution was then subtracted from the binding isotherm to obtain the final plot. This plot was then fit using Origin software to obtain the stoichiometry, K_a, ΔH, and ΔS. The corresponding K_D was calculated as $1/K_a$.

5.2.4 Ellipsometry Experimental Protocol

DPU-TMAB binding experiments were carried out on the *J.A. Woollam* variable angle spectroscopic ellipsometer (VASE) using a 60° liquid prism cell and measuring ψ and Δ and at 633 nm. The η values were calculated from ψ and Δ using WVASE software. For these experiments, samples were prepared similar to BSI experiments with one binding pair (DPU) held constant at 25 µM and TMAB varied from 0-200 µM. The η value from the zero point (25 µM DPU) was then subtracted from the η values of each subsequent data point to obtain a relative η value. The calibration data of TMAB-only was then subtracted from the binding data to obtain the final relative η binding plot. This plot was then fit to a one-site binding hyperbola to obtain K_D.

5.2.5 BSI & Ellipsometry Data Analysis

End-point determination of K_D was carried out as described earlier (Chapter 1.3.5). For these experiments the calibration of the varied ligand is subtracted from the binding data to obtain the final plot of signal vs. ligand concentration. This curve is fit in Prism$^®$ using the one-site binding hyperbola function to obtain K_D.

5.3 Results & Discussion

5.3.1 Study of TMAB Complexation to Urea and Thiourea Derivatives using BSI

Initially end-point BSI experiments of TMAB interaction with DPU and DPTU in MeCN were performed. For these experiments DPU and DPTU were held constant at 10 µM while TMAB was varied from 5-60 µM. BSI experiments were conducted using the procedure outlined in section 5.2.2. The zero point of DPU/DPTU only and the TMAB-only calibration curve (Fig. 5.2) were subtracted from the binding data to obtain the final binding curve. Figures 5.3 and 5.4 show the BSI plot and curve-fit of DPU and DPTU complexation with TMAB. The BSI signals level out at the high concentration of TMAB, showing a saturation binding curve that can be fit to a one-site binding hyperbola to obtain K_D values. Both DPU and DPTU have similar affinity for TMAB with K_D values of 18.5 and 23.2 µM, respectively (Table 5.3).
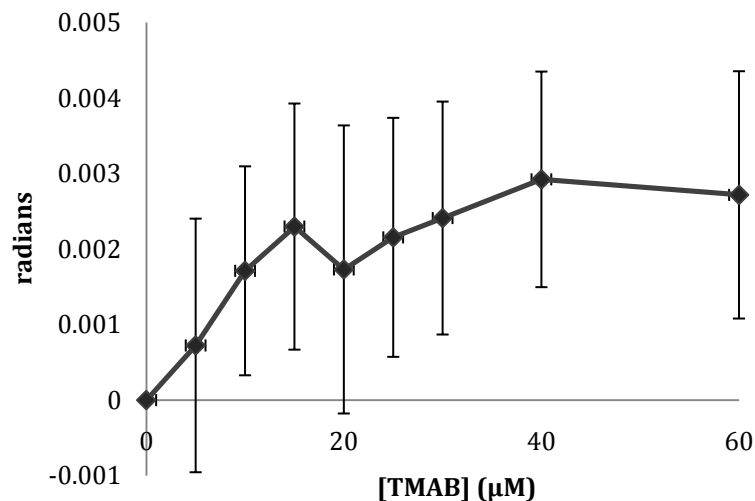
Figure 5.2 TMAB-only calibration 5 trial average plot with TMAB varied in from 0-60 μM. This plot shows a modest increase in signal with increasing TMAB concentration, which is much smaller than the binding signal generated for TMAB binding assays (Fig. 5.3-5.6). The error bars seen in this plot are large because the signal generated is below the effective detection limit of BSI (< 0.005 radians).

Figure 5.3 Steady-state BSI data of 10 μM DPU complexed to TMAB ranging from 0-60 μM in MeCN. Curve fitting to a one-site binding hyperbola yielded a K_D of 18.56 ± 4.46 μM with an R^2 of 0.97.

Figure 5.4 Steady-state BSI data of 10 µM DPTU complexed to TMAB ranging from 5-60 µM in MeCN. Curve fitting to a one-site binding hyperbola yielded a K_D of 23.20 ± 4.55 µM with an r^2 of 0.98.

Table 5.3 K_D values from BSI and ITC and experiments

	BSI	ITC
TMAB Complexation	K_D (µM)	K_D (µM)
DPU	18.56 ± 4.46	21.75 ± 6.04
DPTU	23.20 ± 4.55	27.43 ± 3.72
DNPU	0.54 ± 0.08	1.26 ± 0.06
DNPTU	0.42 ± 0.08	1.18 ± 0.17
TMAS-DPU	146 ± 40	356 ± 27

Next, a higher affinity interaction was examined to test the lower limits of BSI as an analytical tool for small molecule interactions. These experiments were carried out on a similar system with TMAB but the DPU and DPTU were modified to include *para*-substituted nitro groups on both phenyl rings. Experimental and theoretical studies have shown that electron withdrawing groups have a strong effect on molecular recognition of urea and thiourea due to changes in charge distribution and molecular dipole.[23, 24] Therefore, the nitro groups of DNPU and DNPTU are expected to increase the hydrogen

bonding affinity for the benzoate oxygens. BSI experiments were carried out at lower concentrations with DNPU/DNPTU held constant at 1 µM and TMAB varied from 0.5-10 µM. Again, final binding curves were obtained after subtracting out the TMAB-only data. The binding affinity for both DNPU and DNPTU were similar (Table 5.3) with K_D values of 0.54 and 0.42 µM, respectively. As expected, the data obtained show the enhanced binding of DNPU and DNPTU to TMAB due to the presence of the *p*-NO$_2$ groups. The data in Table 5.3 and subsequent binding curves (Fig. 5.5 & 5.6) show similar radian shifts and binding saturation with R^2 values of 0.99.
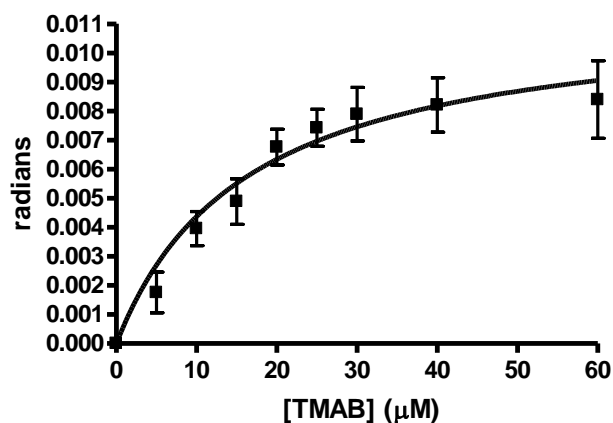

Figure 5.5 Steady-state BSI data of 1 µM DNPU complexed to TMAB ranging from 0.5-10 µM in MeCN. Curve fitting to a one-site binding hyperbola yielded a K_D of 0.54 ± 0.08 µM with an r^2 of 0.99.
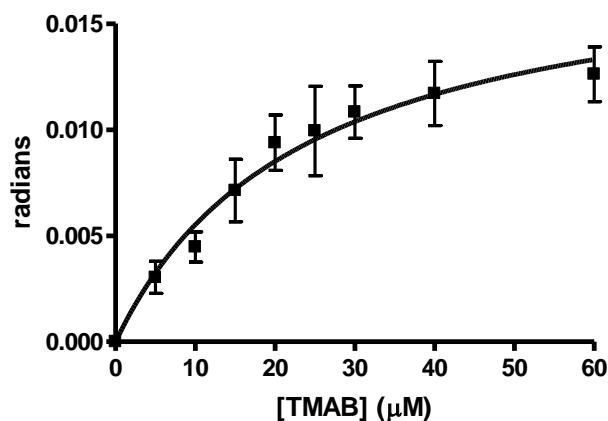
Figure 5.6 Steady-state BSI data of 1 µM DNPTU complexed to TMAB ranging from 0.25-10 µM in MeCN. Curve fitting to a one-site binding hyperbola yielded a K_D of 0.42 ± 0.08 µM with an r^2 of 0.99.

It is important to note that BSI detects specific binding interactions in a concentration dependent manner. To illustrate this point, experimental results were compared for DPU-TMAB and DPU-TMAS interactions. TMAS is not expected to have a strong affinity for DPU as demonstrated by the lower pK_b for benzoate (10) vs. benzenesulfonate (20).[16] For this experiment, BSI data was generated for DPU-TMAB and DPU-TMAS interactions under the same conditions. Given the low affinity for DPU-TMAS, performing a BSI experiment under the same conditions as the DPU-TMAB experiment should produce very different results. As expected, Fig. 5.7 shows the negligible signal shift due to DPU-TMAS complexation whereas DPU-TMAB generates a large signal shift that saturates at much lower concentrations.
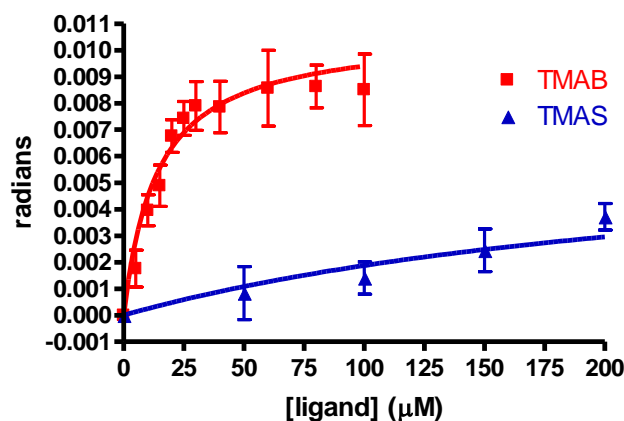
Figure 5.7 Steady-state BSI data of DPU complexed to TMAB (■) and TMAS (▲). The large signal shift for TMAB compared to TMAS shows that BSI detects specific binding and not a non-specific interaction.

The interaction between DPU and TMAS was examined further in order to test the limits of BSI. Initial BSI experiments showed very little TMAS binding at low concentrations of DPU (Fig. 5.7). However, the signal does increase as the concentration of TMAS increases, suggesting some binding is occurring but the affinity is too low to be detected under these conditions. Therefore, analogous experiments were carried out at higher concentrations with DPU held constant at 50 μM and TMAS ranging from 0-600 μM. These experiments produced a saturating binding curve that was fit to obtain a K_D of 0.146 ± 0.04 mM (Fig. 5.8). This value seems reasonable because previously reported dissociation binding constants between sulfonate and (thio)urea derivatives ranged from $0.006 - 22.2$ mM, with the lower values attributed to the prescence of electron withdrawing groups on the (thio)urea derivatives.[16, 24] Comparison of results to the previous BSI experiments shows that the DPU-TMAS interaction produces less binding

signal, thus increasing the noise and error of the data. This decrease in signal is attributed to the high concentrations of TMAS.
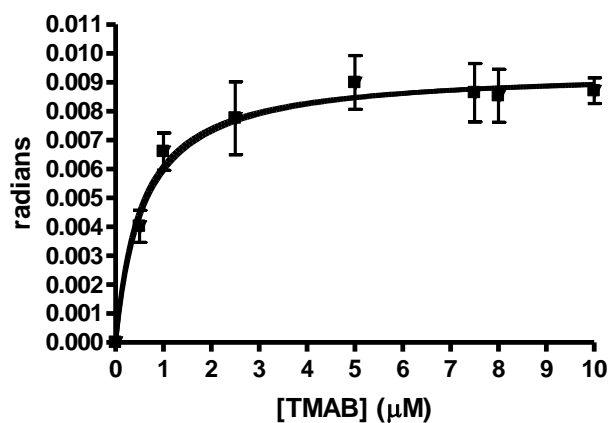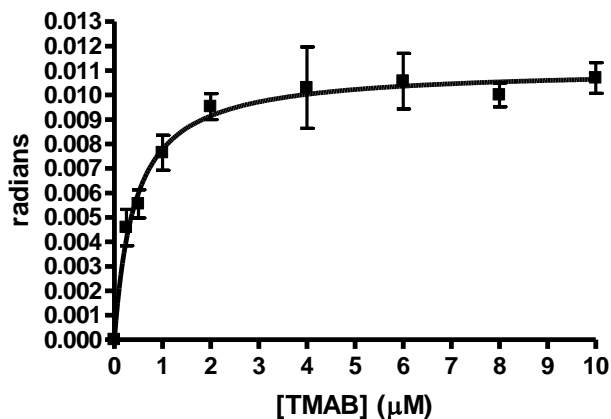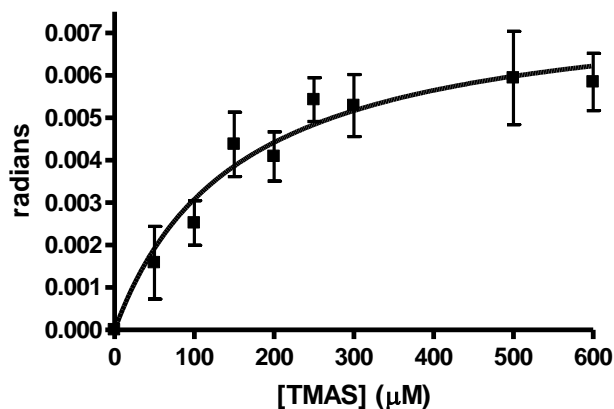

Figure 5.8 Steady-state BSI data of 50 μM DPU complexed to TMAS ranging from 50-600 μM in MeCN. Curve fitting to a one-site binding hyperbola yielded a K_D of 0.146 ± 0.04 mM with an r^2 of 0.95.

5.3.2 Benchmarking with ITC and Ellipsometry

To benchmark the BSI studies, isothermal titration calorimetry (ITC) experiments were performed. Initial experiments were carried out with 5 mM TMAB titrated into the sample cell containing 0.5 mM DPU or DPTU in MeCN at 25 ˚C. Next, the interaction of TMAB with either DNPU or DNPTU was investigated using ITC. As with the BSI studies, these experiments were run at slightly lower concentrations than the TMAB-DPU/DPTU ITC experiments, with 2 mM TMAB titrated into 0.2 mM of either DNPU or DNPTU. The results from these experiments are shown graphically in Figures 5.10-5.13 and numerically in Table 5.4. Results show DPU has a slightly higher affinity for TMAB than DPTU, with respective dissociative binding constants of 21.7 and 27.4 μM. The

opposite trend was seen for TMAB interaction with DNPU and DNPTU, with DNPTU having a slightly lower K_D of 1.2 µM and DNPU with a K_D of 1.4 µM. The BSI K_D values are all within experimental error of the ITC data and exhibit the same trends.

Table 5.4 K_D values and thermodynamic data from ITC experiments.

TMAB Complexation	K_D (µM)	n	ΔH (kcal/mol)	ΔS (cal/mol K)
DPU	21.75 ± 6.04	0.91 ± 0.02	-5.98 ± 0.64	1.55 ± 2.29
DPTU	27.43 ± 3.72	0.96 ± 0.03	-6.56 ± 0.22	-1.09 ± 0.85
DNPU	1.26 ± 0.06	1.06 ± 0.09	-6.43 ± 0.39	5.44 ± 1.31
DNPTU	1.18 ± 0.17	0.96 ± 0.02	-2.59 ± 0.24	18.48 ± 0.93
TMAS-DPU	356.2 ± 27.6	0.81 ± 0.02	-1.39 ± 0.04	11.15 ± 0.27

The ITC data also provide insight into the thermodynamics for each of the binding pairs. The presence of the electron withdrawing nitro groups not only affects the overall binding affinity but also impacts the enthalpic and entropic contributions of the interaction. In the case of DPU and DPTU, the largely negative enthalpy values and neutral entropy values, indicate that the interaction with TMAB is enthalpically driven. Additionally, despite the difference in pKa's for DPU (19.5) and DPTU (13.5) their thermodynamic values are nearly equal.[25] Conversely, entropic variables play more of a role for the interaction of TMAB with DNPU and DNPTU, with substantial differences seen between the urea and thiourea derivatives. The positive entropy values are most likely due to solvation of (thio)urea which is displaced upon TMAB binding, thus increasing the disorder in the system (Fig. 5.9). It is interesting to note that the differences in the enthalpic and entropic contributions of urea and thiourea become more pronounced when electron-withdrawing groups are introduced. While the pKa's of

DNPU and DNPTU have never been reported, DNPTU is expected to be more acidic giving rise to a higher propensity to interact with the solvent than DNPU, leading to a higher entropy value.
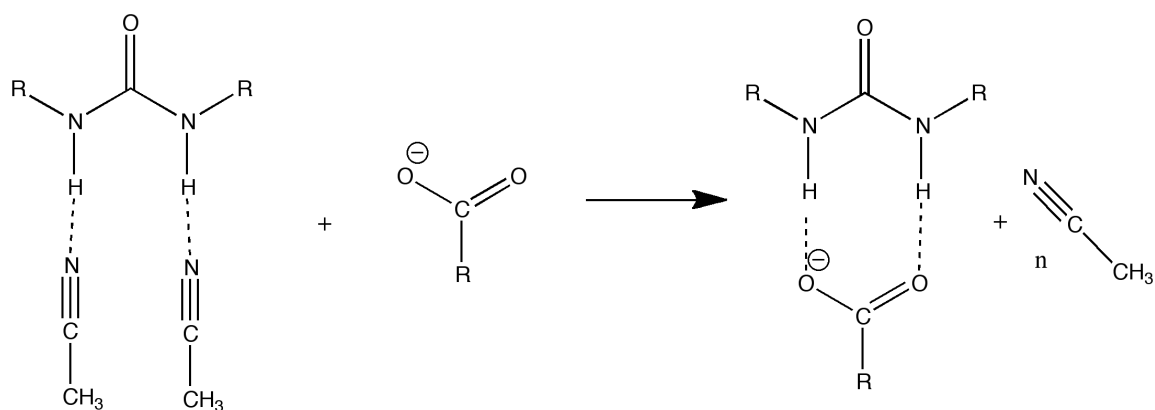
Figure 5.9 Hydrogen bonding between analytes and MeCN lead to solvation effects that impact the entropy of the interaction.

Figure 5.10 ITC data for DPU-TMAB binding with 5 mM TMAB titrated into 0.5 mM DPU at 25 °C. Average data provided a K_D of 21.75 ± 6.04 μM, ΔH of -5.98 ± 0.64 kcal/mol, ΔS of 1.55 ± 2.29 cal/mol K, and a stoichiometry of 0.91 ± 0.02.

Figure 5.11 ITC data for DPTU-TMAB binding with 5 mM TMAB titrated into 0.5 mM DPTU at 25 °C. Average data provided a K_D of 27.43 ± 3.72 μM, ΔH of -6.56 ± 0.22 kcal/mol, ΔS of -1.09 ± 0.85 cal/mol K, and a stoichiometry of 0.96 ± 0.03.

Figure 5.12 ITC data for DNPU-TMAB binding with 2 mM TMAB titrated into 0.2 mM DNPU at 25 °C. Average data provided a K_D of 1.26 ± 0.01 µM, ΔH of -6.43 ± 0.39 kcal/mol, ΔS of 5.44 ± 1.31 cal/mol K, and a stoichiometry of 1.06 ± 0.09.

Figure 5.13 ITC data for DNPTU-TMAB binding with 2 mM TMAB titrated into 0.2 mM DNPTU at 25 °C. Average data provided a K_D of 1.18 ± 0.17 μM, ΔH of -2.59 ± 0.24 kcal/mol, ΔS of 18.48 ± 0.93 cal/mol K, and a stoichiometry of 0.97 ± 0.02.

The interaction between DPU and TMAS was also benchmarked with ITC. The ITC experiments were carried out with DPU in the cell at 1 mM and TMAS titrated in at 10 mM (Fig. 5.14). Results from this experiment correlate with BSI, although the average K_D value from ITC is higher at 0.343 mM compared to 0.146 mM obtained with BSI. The DPU-TMAS BSI experiments effectively place a limit on the utility of BSI to detect low affinity interactions. The DPU-TMAS interaction is not strong enough to be

studied at low concentrations. Subsequently, the concentration-dependent calibration curve has a significant impact on monitoring the binding signal. Thermodynamically, this interaction is entropically driven, as seen by the high positive entropy value. Again, this is most likely due to solvation effects and self-association of DPU since it was 2x more concentrated than the previous ITC experiments.

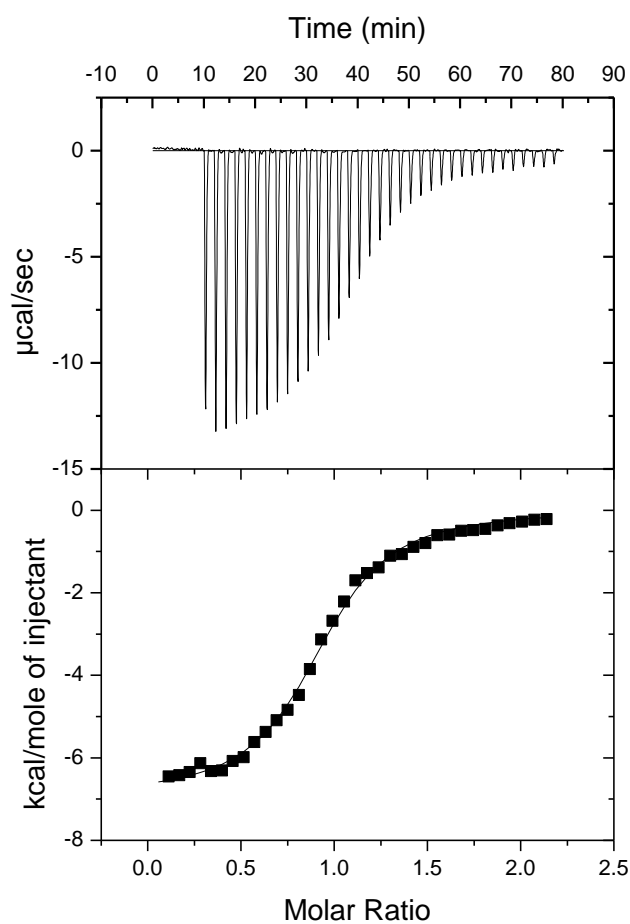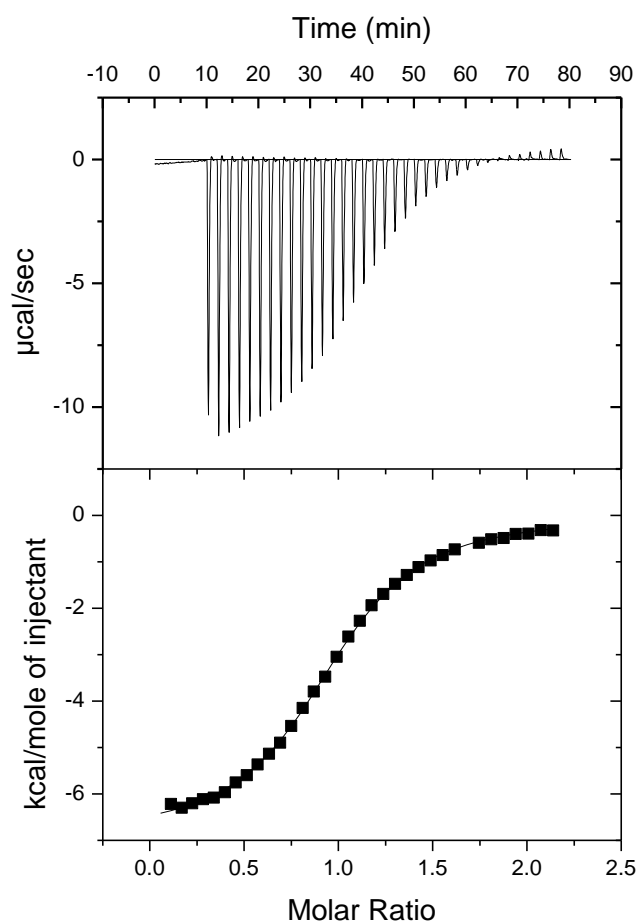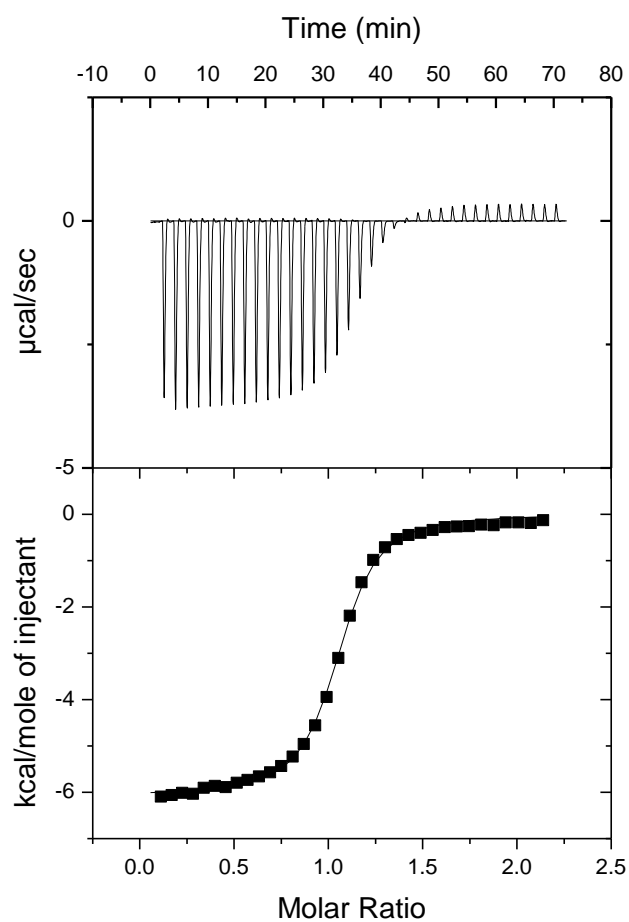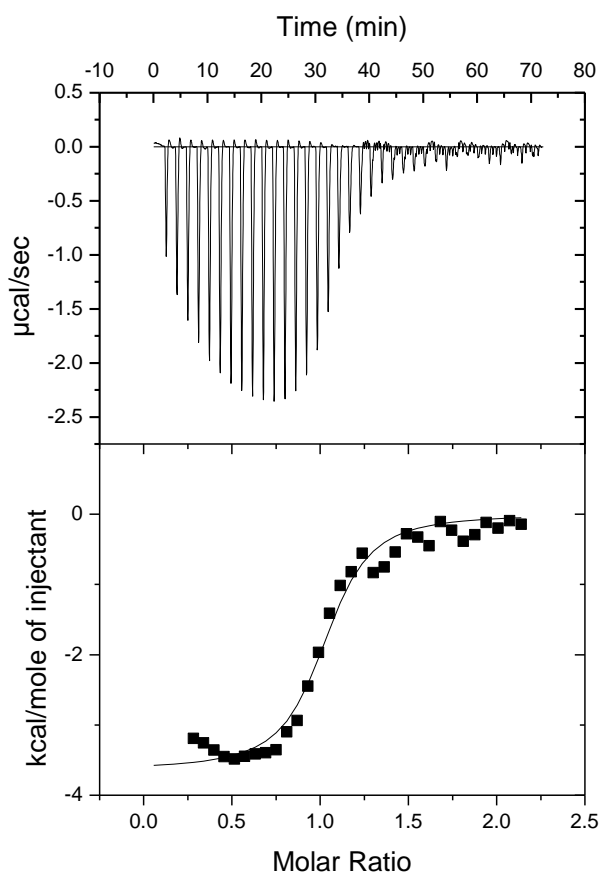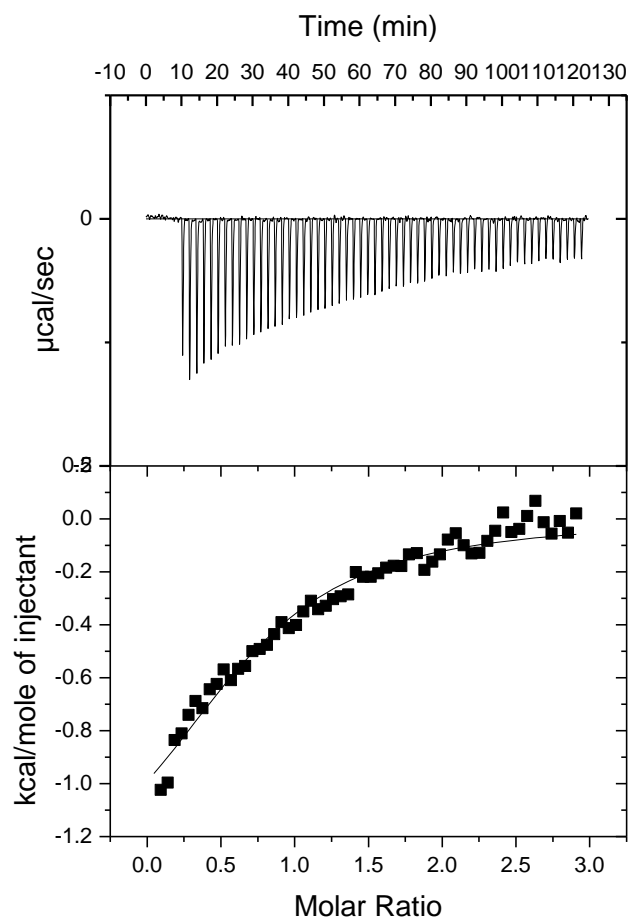**Figure 5.14** ITC data for DPU-TMAS binding with 10 mM TMAS titrated into 1 mM DPU at 25 °C. Average data provided a K_D of 0.356 ± 0.027 mM, ΔH of -1.39 ± 0.04 kcal/mol, ΔS of 11.15 ± 0.27 cal/mol K, and a stoichiometry of 0.82 ± 0.02.

Spectroscopic ellipsometry experiments were carried out for the DPU-TMAB interaction to relate the BSI signal shift to changes in RI. These experiments were performed using a 60° liquid prism cell and the refractive index was calculated at 633 nm, the same wavelength used in the BSI experiments. In order to obtain significant changes in the refractive index, the concentrations of the binding pairs were increased, with DPU held constant at 25 µM and TMAB varied from 25-200 µM. The final binding data was obtained by subtracting out the zero point of 25 µM DPU from the binding data and then subtracting out the subsequent refractive index calibration curve of the varying concentration of TMAB. Analysis of the ellipsometry data was analogous to BSI since the experiments were performed at steady-state and also measured the change in refractive index. Figure 5.14 shows the ellipsometry average plot with the curve fit obtaining a K_D value of 19.40 ± 6.23 µM. The ellipsometry data correlate with the BSI K_D values, providing further evidence that the BSI signal shift is related to variations in refractive index during complex formation.
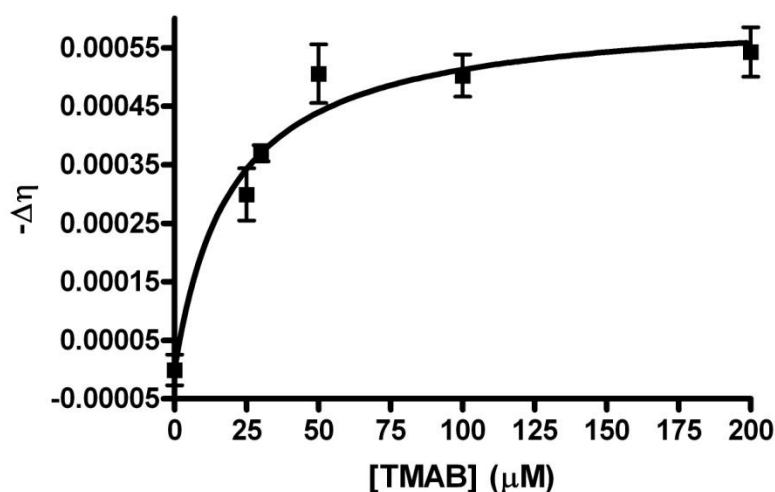
Figure 5.15 Plot of ellipsometry refractive index measurements at 633nm. The relative refractive index of equilibrated samples containing 25 µM DPU and 0-200 µM TMAB show a saturation binding curve. Curve fitting to a one-site binding hyperbola yielded a K_D of 19.40 ± 6.23 µM with an R^2 of 0.97.

5.4 Conclusion

In conclusion, the present study demonstrates the applicability of BSI as a tool for studying small molecule interaction in non-aqueous solvents. Not only is BSI able to recognize the formation of just two hydrogen bonds, but it can also distinguish between TMAB complexation with DPU/DPTU and DNPU/DNPTU with an affinity difference of more than one order of magnitude. These experiments helped to elucidate the lower limits of BSI as an analytical tool for screening small molecule interactions. BSI was able to detect complex formation between DPU and TMAS, however these experiments required fairly high concentrations (up to 0.6 mM TMAS) due to the low affinity of the interaction. For this experiment, the signal change attributed to the increasing concentration of TMAS began to impact the binding signal. Therefore, low affinity interactions, with K_D values in the mM range, may present some issues for studying small

molecule interactions using BSI. On the other hand, high affinity interactions, such as TMAB-DNPU, did not face these problems since the interaction was detectable at much lower concentrations (up to 10 μM DNPU).

BSI experiments have the advantage of using smaller volumes and lower concentrations than ITC and ellipsometry. The microfluidic channel used in these BSI experiments has a cross-sectional area of 3600 μm^2 that, when interrogated by a 100 μm diameter laser, provides an optical probe volume of ca. 360 pL. At the lowest concentrations used in these experiments, BSI is able to detect an interaction between ca. 325.2 million molecules. When compared to the concentrations and volumes used for ITC and ellipsometry, BSI is 6 orders of magnitude more sensitive than ITC and 8 orders of magnitude more than ellipsometry. This sensitivity makes BSI interaction-efficient, with the ability to detect a relatively small number of discreet binding events when compared to other free-solution techniques. The simple, user-friendly design of BSI provides a technique by which organic chemists can develop interaction-dependent reactions by following a change in refractive index.

5.5 Spectral Data
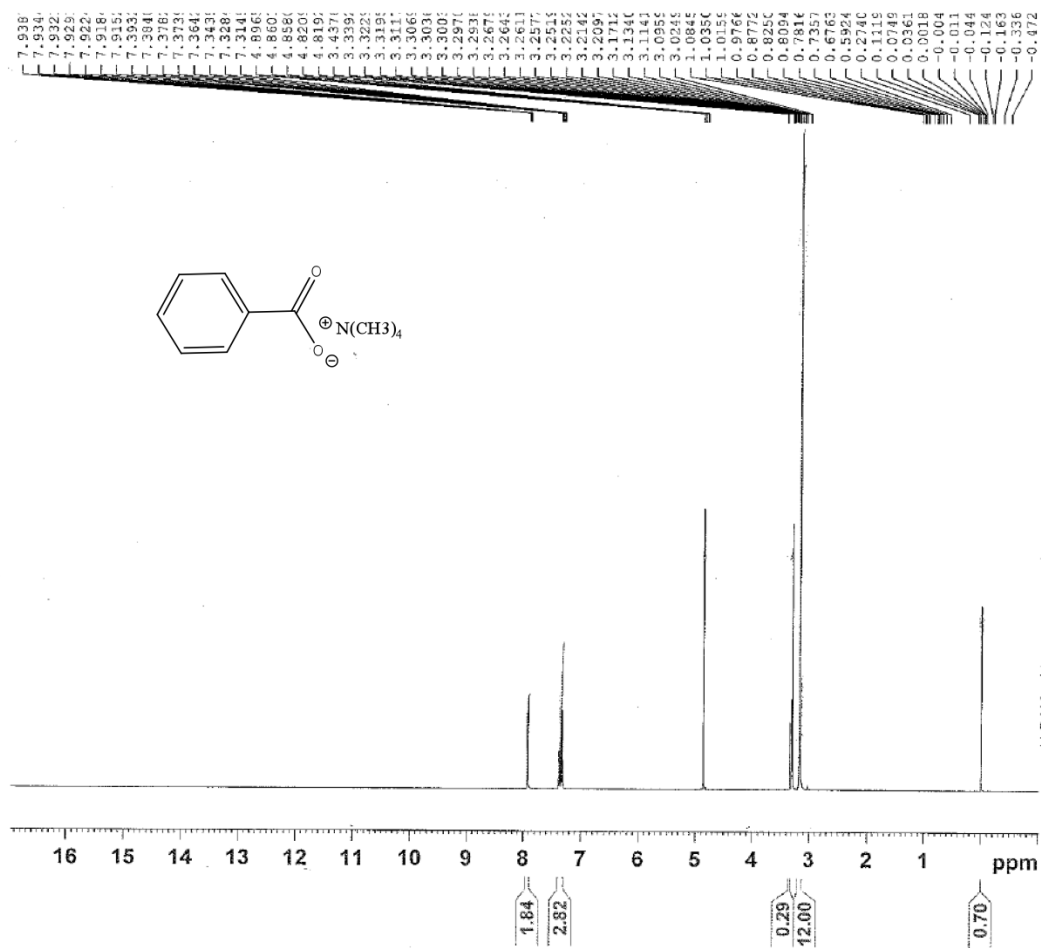
Figure 5.16 TMAB ^{1}H-NMR (MeOH-d$_4$, 500MHz) δ 3.15 (s, 12H), 7.34 (m, 3H), 7.92 (d, 2H). White solid.
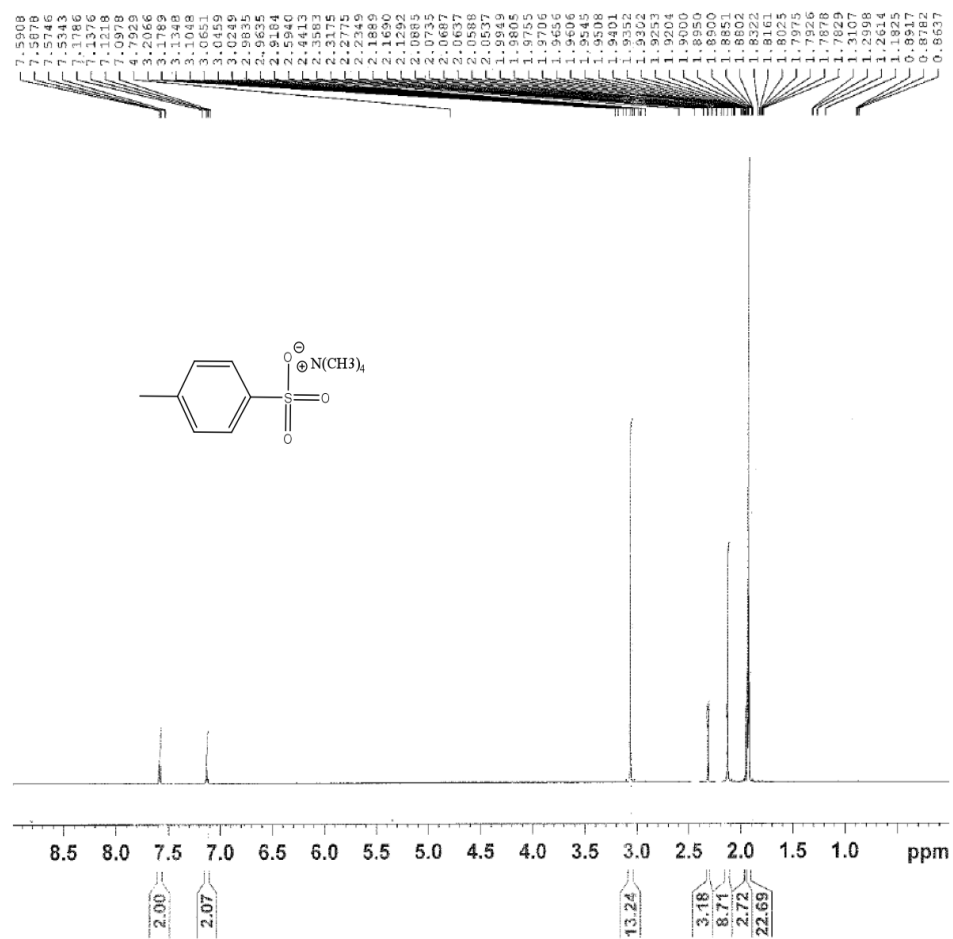
Figure 5.17 TMAS ^{1}H-NMR (MeCN-d$_3$, 500 MHz) δ 2.27 (s, 3H), 3.06 (s, 12H), 7.13 (d, 2H), 7.57 (d, 2H). White solid.
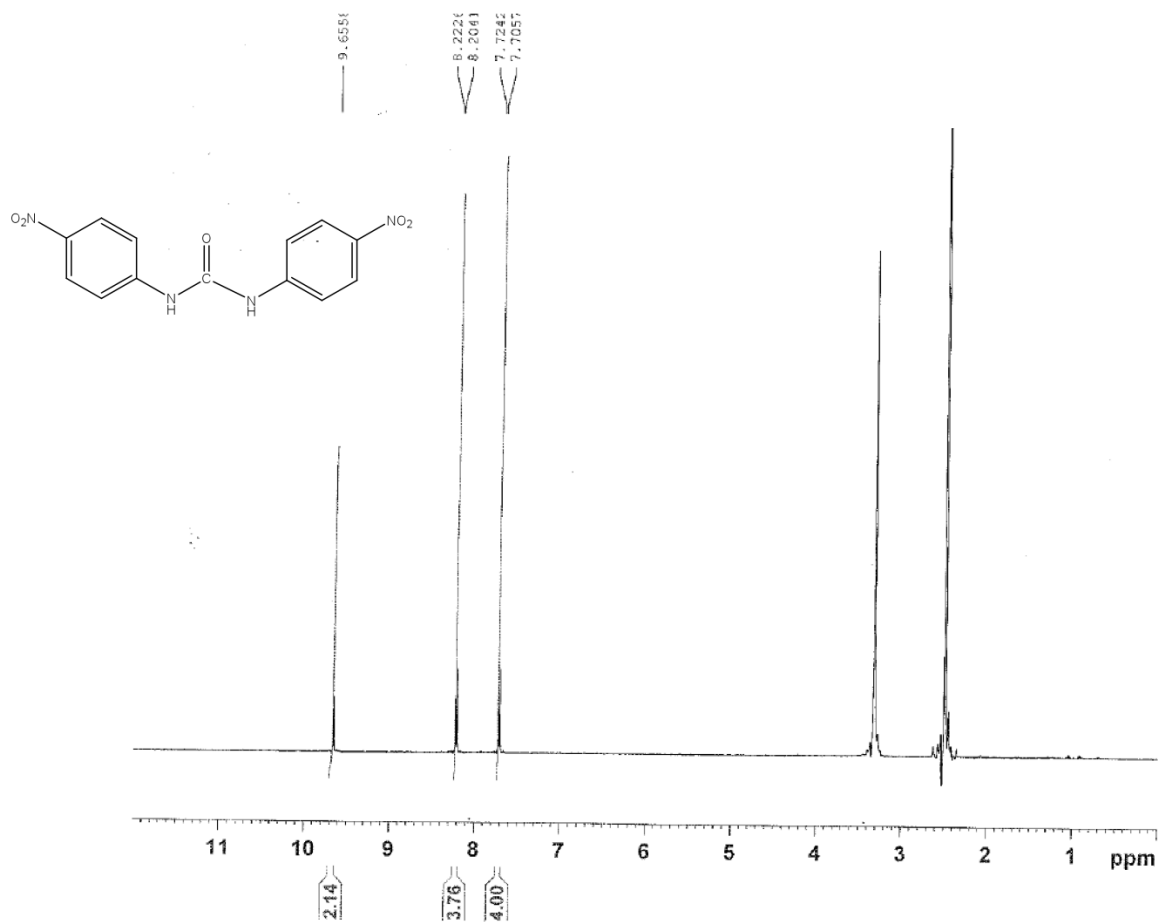
Figure 5.18 DNPU ^{1}H-NMR (DMSO-d_6, 500 MHz) δ 7.71 (d, 4H), 8.21 (d, 4H), 9.65 (s, 2H). Yellow solid.
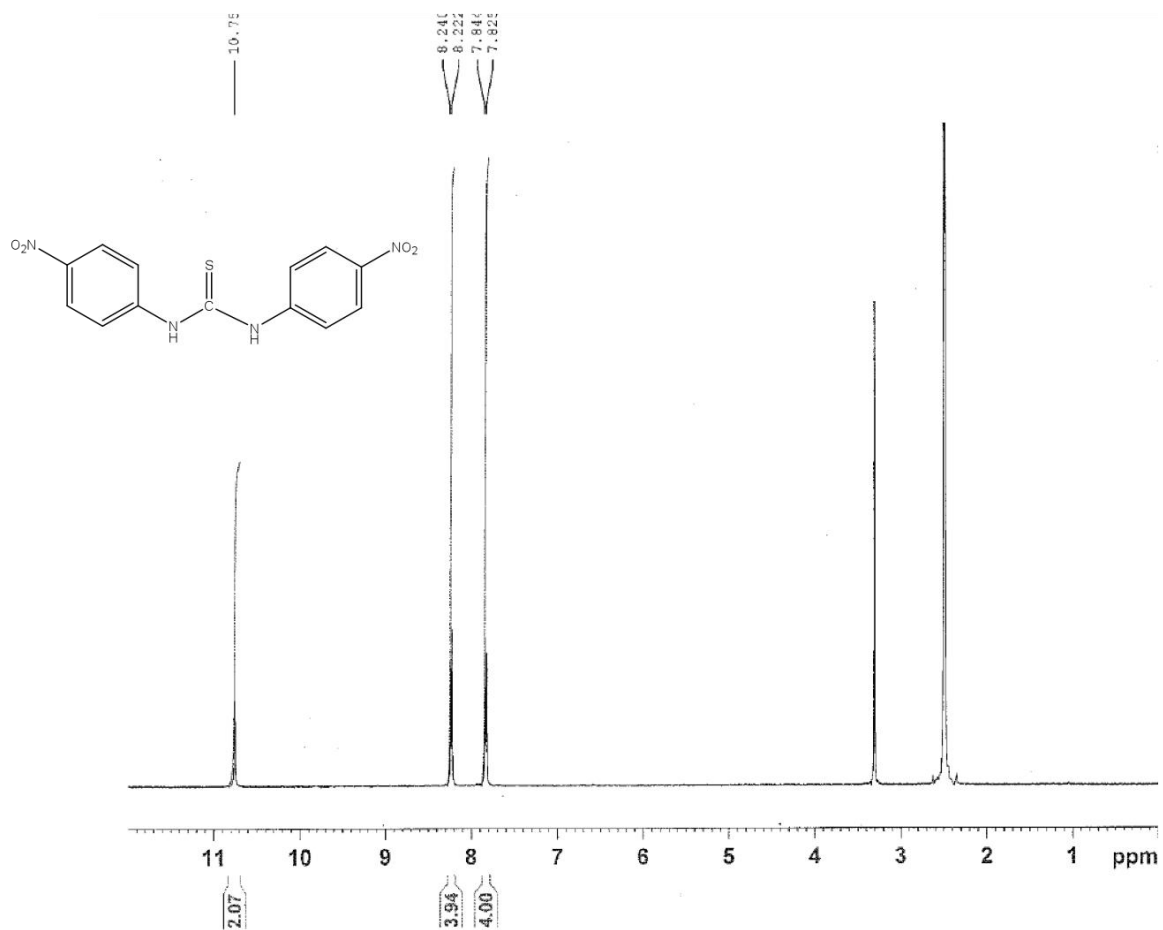
Figure 5.19 DNPTU ^{1}H-NMR (DMSO-d$_6$, 500 MHz) δ 7.83 (d, 4H), 8.23 (d, 4H), 10.75 (s, 2H). Yellow solid.

5.6 References

(1) Taylor, M. S.; Jacobsen, E. N. *Angew. Chem. Int. Ed Engl.* **2006***, 45*, 1520-1543.

(2) Hunter, C. A. *Angew. Chem. Int. Ed Engl.* **2004***, 43*, 5310-5324.

(3) Brown, A. R.; Kuo, W. H.; Jacobsen, E. N. *J. Am. Chem. Soc.* **2010***, 132*, 9286-9288.

(4) Zotova, N.; Broadbelt, L. J.; Armstrong, A.; Blackmond, D. G. *Bioorg. Med. Chem. Lett.* **2009***, 19*, 3934-3937.

(5) Tarkanyi, G.; Kiraly, P.; Varga, S.; Vakulya, B.; Soos, T. *Chemistry* **2008***, 14*, 6078-6086.

(6) Noziere, B.; Cordova, A. *J Phys Chem A* **2008***, 112*, 2827-2837.

(7) Hoang, L.; Bahmanyar, S.; Houk, K. N.; List, B. *J. Am. Chem. Soc.* **2003***, 125*, 16-17.

(8) Jadhav, V. D.; Schmidtchen, F. P. *J. Org. Chem.* **2008***, 73*, 1077-1087.

(9) Solomonov, B. N.; Novikov, V. B. *J. Phys. Org. Chem* **2007***, 21*, 2-13.

(10) Sanford, A. R.; Yuan, L.; Feng, W.; Yamato, K.; Flowers, R. A.; Gong, B. *Chem. Commun. (Camb)* **2005***, 37*, 4720-4722.

(11) Bornhop, D. J.; Latham, J. C.; Kussrow, A.; Markov, D. A.; Jones, R. D.; Sorensen, H. S. *Science* **2007***, 317*, 1732-1736.

(12) Latham, J. C.; Stein, R. A.; Bornhop, D. J.; McHaourab, H. S. *Anal. Chem.* **2009***, 81*, 1865-1871.

(13) Kussrow, A.; Kaltgrad, E.; Wolfenden, M. L.; Cloninger, M. J.; Finn, M. G.; Bornhop, D. J. *Anal. Chem.* **2009***, 81*, 4889-4897.

(14) Pesciotta, E. N.; Bornhop, D. J.; Flowers, R. A., II *Chem. Asian J.* **2011***, 6*, 70-73.

(15) Weast, R. C., Ed.; In *Handbook of Chemistry and Physics;* CRC Press: Cleveland, Ohio, **1975**, 56th Ed.

(16) Kelly, T. R.; Kim, M. K. *J. Am. Chem. Soc.* **1994***, 116*, 7072-7080.

(17) Schmidtchen, F. P.; Berger, M. *Chem. Rev.* **1997***, 97*, 1609-1646.

(18) Takemoto, Y. *Org. Biomol. Chem.* **2005***, 3*, 4299-4306.

(19) Werner, F.; Schneider, H. *Helv. Chim. Acta* **2000***, 83*, 465-478.

(20) Smith, P. J.; Reddington, M. V.; Wilcox, C. S. *Tet. Lett.* **1992***, 33*, 6085-6088.

(21) Kelly, T. R.; Meghani, P.; Ekkundim, V. S. *Tet. Lett.* **1990***, 31*, 3381-3384.

(22) Etter, M. C. *Acc. Chem. Res.* **1990***, 23*, 120-126.

(23) Etter, M. C.; Urbancyzk-Lipowska, Z.; Zia-Ebrahimi, M.; Panunto, T. W. *J. Am. Chem. Soc.* **1990***, 112*, 8415-8426.

(24) Wilcox, C. S.; Kim, E.; Romano, D.; Kuo, L. H.; Burt, A. L.; Curran, D. P. *Tetrahedron* **1995***, 51*, 621-634.

(25) Bordwell, F. G.; Algrim, D. J.; Harrelson, J. A. J. *J. Am. Chem. Soc.* **1988***, 110*, 5903-5904.

Chapter 6

Conclusions and Future Work

The importance of studying molecular interactions in a free-solution, label free manner cannot be understated. When characterizing bio-molecular interactions, it is critical to maintain physiologically relevant conditions to gain insight into the native state of the interaction. Common modifications such as fluorescent labeling or surface tethering can alter the energetics and affinity of an interaction. Free-solution techniques such as ITC eliminate this problem, however, they often require large volumes and concentrations that are not practical for the study of biological samples. BSI provides a missing link in current analytical instrumentation by enabling the study of interactions in a label-free, free-solution manner while utilizing low concentrations and small volumes.

The work discussed in this dissertation illustrates the broad applicability of BSI to study a wide variety of intermolecular interactions via changes in RI. RI analysis is often used as a detector for analytical instrumentation such as high performance liquid chromatography and capillary electrophoresis. RI detection is advantageous because it is universal in nature, however often lacks sensitivity due to small changes in ambient temperature, pressure, and flow rates.[1] To overcome these issues, BSI utilizes a multi-pass configuration to increase the detection limit while still working with nanoscale detection volumes.[2] Additionally, BSI can be configured to include a reference that can be subtracted from the sample data to eliminate the noise from temperature fluctuations, pressure changes, and variable flow rates.[3] Furthermore, the studies described herein show the potential for RI analysis to be used as a universal signal for detecting molecular

binding events. BSI instrumentation enabled the quantification of binding affinities for several systems including protein-ligand interactions, oligonucleotide hybridization, and small molecule hydrogen bonding events in non-aqueous media. Undoubtedly, there are a countless number of interaction systems to be studied and while this thesis only discussed a few, the broad scope through which BSI can quantify intermolecular interactions make universal sensing through RI detection feasible.

6.1 Origin of BSI Signal

Where does the binding signal come from? It is clear that the BSI signal is responsive to changes in RI, but what causes the shift in RI when two molecules bind? This underlying question is intrinsically present in all of the BSI experiments and does not have a simple answer. Previously Bornhop and coworkers postulated that this shift in RI is a result of changes in molecular structure,[4] dipole moment, polarizability,[5] conformation, and solvation[6] that occur during an interaction due to the formation of new species.[7] To correlate these parameters to RI changes and experimental results, we looked at the direction of the radian shift from various binding and non-binding analytes. When running a glycerol calibration with BSI, the signal shifts in the negative direction as the concentration of glycerol increases (Fig 1.10). Therefore as the optical density or RI of the solution increases, the BSI signal gets more negative. The direction of the signal shift is specific for each instrument and depends on the orientation of the CCD camera. Since different analytes vary in optical density, the calibration of different analytes should all go in the same direction but have varying slopes. To verify this relationship, aqueous BSI calibrations were carried out with ethanol, hydrochloric acid,

131

urea, and glycerol (Fig. 6.1). There is a linear relationship between the slope of different

BSI calibrations (change in radians with concentration) and the optical density (change in

RI with concentration), shown in Figure 6.2. With these experiments it is possible to test

the hypothesis that BSI binding signal arises from a change in optical density, likely to

arise from a change in the solvation state when binding occurs.
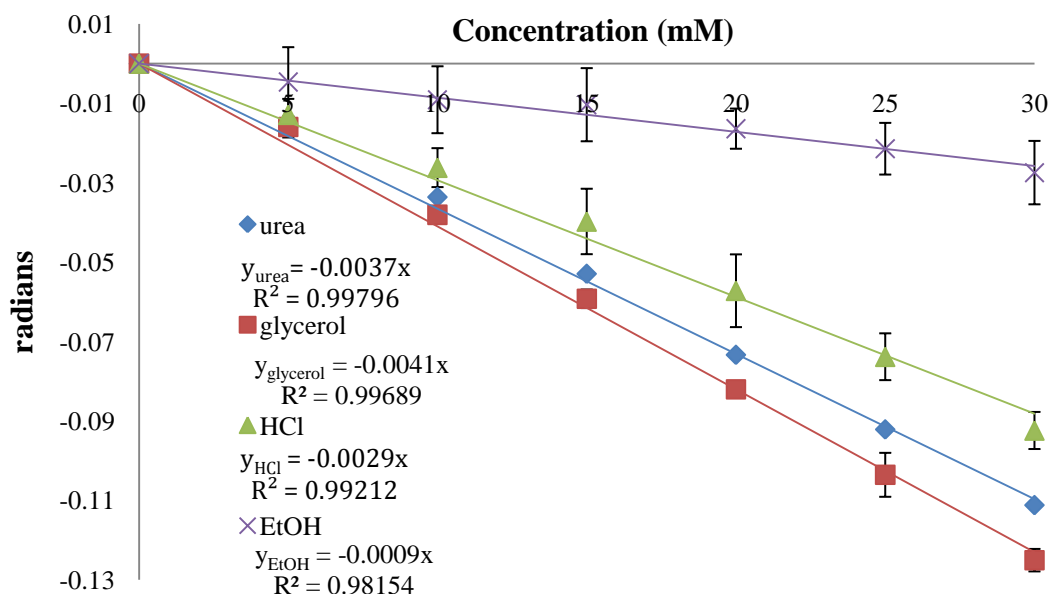
Figure 6.1 BSI aqueous calibration curves of analytes with varying optical density.
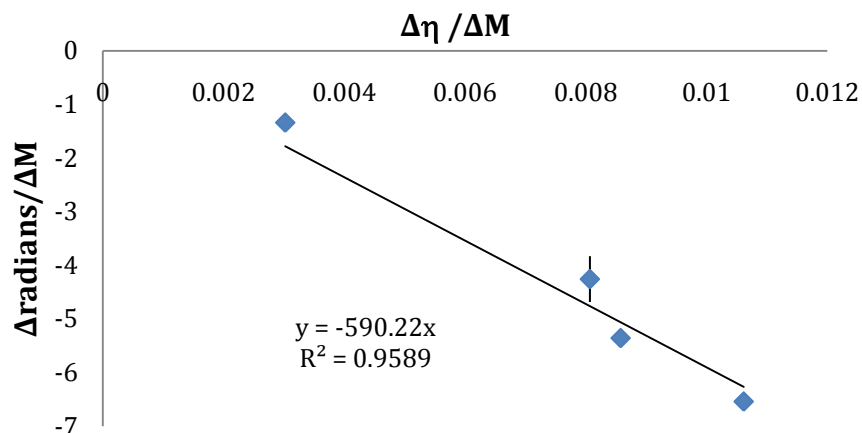
Figure 6.2 Change in BSI signal versus change in RI with concentration. This plot shows that the BSI signal gets more negative as the RI of the solution increases. Each data point corresponds to the calibration curves found in Figure 6.1.

Comparison of the aqueous calibration data with the olignucleotide hybridization experiments provides some interesting observations. When running a calibration curve of the unlabeled duplex at increasing concentration, the shift was negative (Fig. 4.3), similar to the expected direction of a calibration as seen in Figure 6.1. Conversely, the free-solution hybridization experiments exhibit BSI shifts in the positive direction (Fig 4.5). The single strand calibration produced a negligible BSI signal shift very close to zero, however, this also produced positive radian shifts (Fig. 4.4). So, what does this mean? The negative shift observed for the duplex calibration indicates an increase in optical density due to increasing dsDNA concentration. A positive radian shift due to binding is consistent with a decrease in optical density that can arise from a decrease in polarizability, conformational changes, and displacement of water molecules. Additionally, we hypothesize that the positive shift for the ssDNA calibration could be due to self-association and induced conformational changes due to increasing oligomer

133

concentration. Recently, Saraf and coworkers examined the difference in RI of ssDNA and dsDNA immobilized onto a silica surface using ellipsometry.[8] In this study, the RI of a dsDNA-modified surface was 5% larger than the ssDNA-modified surface. Interestingly, they found that this increase in RI was 20% smaller than the expected change due to doubling the molecular weight. The authors concluded that this is due to a decrease in polarizability of nucleotides in the duplex form, which is consistent with our findings.

While investigating molecular binding in non-aqueous solvents, a similar phenomenon was observed. Both the binding assay and ligand calibration produced positive radian shifts (Fig. 5.2 & 5.3). These results are consistent with the ellipsometry data generated for the DPU-TMAB system. In the ellipsometry experiments the data produced negative $\Delta\eta$ values, just as expected given the positive radian shift from BSI (Fig. 5.14). Additionally, the ITC results provide insight into the thermodynamics of the non-aqueous system. For both DPU and DPTU, the entropic contribution was near zero, indicating that solvation is playing a role in the overall thermodynamics of the interaction. While several factors can contribute to the RI shift seen during an intermolecular interaction, it is clear that a decrease in optical density from changes in polarizability, conformation, and solvation are contributing factors.

6.2 Concluding Remarks

This project initially began out of the need for instrumentation with the ability to study intermolecular interaction in label-free, free-solution manner using microscale sample quantities. BSI has fulfilled this mission, allowing the quantification of binding

interactions over a wide range of systems. Chapter 3 exemplified the dynamic range of BSI. CaM was used as a model system to benchmark BSI studies because it binds to a wide variety of ligands, with a large range of affinities. Through this study, BSI was able to detect interactions with K_D's spanning 4 orders of magnitude from low nM to a mid μM range. These experiments helped elucidate the advantages and disadvantages of BSI through comparison with ITC. BSI has the advantages of high sensitivity, the potential to obtain kinetic data, and ease of sample preparation (i.e. no dialysis required). ITC, on the other hand, requires larger volumes and higher concentrations but provides more information on the interaction, yielding a complete thermodynamic profile. Additionally, the CaM/M13 ITC experiments exemplified the importance of carrying out experiments with physiologically relevant concentrations because of erroneous data obtained at high peptide concentrations.

One unique feature of BSI is the ability to study binding events in free-solution as well as in a surface-immobilized format. Similar microscale instrumentation, such as SPR, requires tethering of the analyte to the surface to generate a binding signal. While this method works very well, surface preparation is often time consuming, costly, and there is always a risk of binding perturbation due to surface immobilization. Moreover, there is no straightforward method to determine the impact of surface tethering on binding affinity other than extrapolation to other techniques. Chapter 4 discussed this issue in detail in regards to oligonucleotide hybridization in surface-immobilized and free-solution formats. Using BSI, the impact of surface immobilization using traditional biotin-avidin chemistry was directly quantified. Comparison of surface-bound and free-solution hybridization showed duplex destabilization due to surface immobilization;

increasing K_D values by nearly 50%. Future work in this area includes comparison of free-solution versus surface-immobilized hybridization at a much broader scope, by incorporating several surface preparations such as immobilization through hexahistidine tail-nitrilotriacetic acid binding,[9] aminodecan-1-ene modified silicon surface coupled with a thiolated oligonucleotide,[10] and many others.[11]

Another goal for the oligonucleotide hybridization experiments was to investigate the impact of fluorescent labeling on duplex affinity. This study utilized the advantage of BSI to study interactions in a label-free manner. Results from these experiments showed a modest impact of two commonly employed fluorophores, Cy3 and FITC, on oligonucleotide hybridization. Attaching these probes to the 5' end of one oligomer stabilized the duplex as seen by an increase in T_m and a decrease in K_D values when compared to an unlabeled strand.

The final objective for the DNA hybridization experiments was to determine if BSI analysis was sensitive to two-base mismatches located on one oligonucleotide strand. The detection of mismatched base pairs is an important area in medical diagnostics and genetic screening. When investigating perturbations due to two-base mismatches, it was clear that mismatches located in the middle of the strand severely disrupted duplex hybridization whereas those located on the end had minimal impact. The K_D and T_m values for the complementary and terminal mismatch were nearly the same while the internal mismatch increased the K_D by nearly 4 times and lowered the T_m by 5.5 °C.

The detection of mismatches, specifically single nucleotide polymorphisms (SNP), is of vital importance in disease detection and determination of individual drug

response.[12, 13] An SNP is a substitution, deletion, or insertion of a single base in the genome.[14] SNP's comprise approximately 90% of genetic mutations, occurring in one out of every thousand bases.[15] Given the importance of SNP's, it would be beneficial to test the application of BSI for SNP detection. Currently, more experiments are being performed to detect different types of SNP using BSI. Initially, an internal single-base mismatch and deletion were investigated using the same 30mer as previously described. Preliminary results from these experiments show very small differences between the perfect compliment and SNP duplexes. It is likely that the perturbations due to these SNPs are negligible because of they are stabilized by 29 nucleotide base pairs. Future work involves testing smaller oligomers containing 20 base pairs for SNP detection. Much of the SNP detection found in the literature is carried out with 15-20mer strands, so this is a reasonable next step. These experiments will be carried out in both free-solution and surface-immobilized formats to further investigate the larger signal shift that arose from the internal mismatch.

Chapter 5 demonstrates the applicability of BSI as a tool for studying small molecule interactions in non-aqueous solvents. Not only was BSI able to recognize the formation of just two hydrogen bonds, but it also distinguished between TMAB complexation with DPU/DPTU and DNPU/DNPTU with an affinity difference of more than one order of magnitude. These experiments helped to elucidate the lower limits of BSI as an analytical tool for screening small molecule interactions. BSI was able to detect complex formation between DPU and TMAS, however these experiments required fairly high concentrations (up to 0.6 mM TMAS) due to the low affinity of the interaction. For this experiment, the signal change attributed to the increasing

concentration of TMAS began to impact the binding signal. Therefore, low affinity interactions, with K_D values in the mM range, may present some issues for studying small molecule interactions using BSI. On the other hand, these problems were not encountered with high affinity interactions, such as TMAB-DNPU, because the interaction was detectable at much lower concentrations (up to 10 µM DNPU).

BSI experiments have the advantage of using smaller volumes and lower concentrations than ITC and ellipsometry. The microfluidic channel used in these BSI experiments has a cross-sectional area of 3600 µm^2 that, when interrogated by a 100 µm diameter laser, provides an optical probe volume of ca. 360 pL. At the lowest concentrations used in the non-aqueous experiments, BSI is able to detect an interaction between ca. 325.2 million molecules and even fewer molecules for higher affinity interactions between biomolecules. When compared to the concentrations and volumes used for ITC and ellipsometry, BSI is 6 orders of magnitude more sensitive than ITC and 8 orders of magnitude more than ellipsometry. This sensitivity makes BSI interaction-efficient, with the ability to detect a relatively small number of discreet binding events when compared to other free-solution techniques. The simple, user-friendly design of BSI provides a technique to study a range of interactions including but not limited to protein-protein, protein-ligand, oligonucleotide hybridization, and small molecules in aqueous and non-aqueous media. The universal sensing platform of BSI provides the potential to improve molecular detection by supplying a free-solution, label-free approach to study intermolecular interactions.

6.3 References

(1) Skoog, D. A.; West, D. M.; Holler, F. J.; Crouch, S. R., Eds.; In *Fundamentals of Analytical Chemistry;* Brooks/Cole, Thomson Learning, Inc.: Bangalore, **2004**, pp 1051.

(2) Wang, Z.; Swinney, K.; Bornhop, D. J. *Electrophoresis* **2003***, 24*, 865-873.

(3) Wang, Z.; Bornhop, D. J. *Anal. Chem.* **2005***, 77*, 7872-7877.

(4) Elkashef, H. *Opt. Mater.* **1997***, 8*, 175-183.

(5) Maroulis, G.; Xenides, D.; Hohm, U.; Loose, A. *J. Chem. Phys.* **2001***, 115*, 7957-7967.

(6) Sota, H.; Hasegawa, Y.; Iwakura, M. *Anal. Chem.* **1998***, 70*, 2019-2024.

(7) Bornhop, D. J.; Latham, J. C.; Kussrow, A.; Markov, D. A.; Jones, R. D.; Sorensen, H. S. *Science* **2007***, 317*, 1732-1736.

(8) Elhadj, S.; Singh, G.; Saraf, R. F. *Langmuir* **2004***, 20*, 5539-5543.

(9) Bilitewski, U. *Anal. Chim. Acta* **2006***, 568*, 232-247.

(10) Strother, T.; Hamers, R. J.; Smith, L. M. *Nucleic Acids Res.* **2000***, 28*, 3535-3541.

(11) Heise, C.; Bier, F. F. *Immobilisation of Dna on Chips II* **2005***, 261*, 1-25.

(12) Xiao, Y.; Plakos, K. J.; Lou, X.; White, R. J.; Qian, J.; Plaxco, K. W.; Soh, H. T. *Angew. Chem. Int. Ed Engl.* **2009***, 48*, 4354-4358.

(13) Weinshilboum, R. In *Genomic Medicine;* Guttmacher, A. E., Collins, F. S. and Drazen, J. M., Eds.; The Johns Hopkins University Press: Baltimore, **2004**, pp 41-53.

(14) Thein, S. L.; Wallace, R. B. In *Human Genetic Diseases;* Davies, K. E., Ed.; IRL Press Limited: Oxford, **1986**, pp 33-50.

(15) Wang, Z.; Moult, J. *Hum. Mutat.* **2001***, 17*, 263-270.

Esther N. Pesciotta
Curriculum Vitae

CONTACT INFORMATION

181 Mercer St. Apt 10B   enp3@lehigh.edu
Somerville, NJ 08876   (732) 995-2776

EDUCATION

Ph.D., Chemistry, Lehigh University, Bethlehem, PA   March 2011
   Dissertation: "Back-scattering Interferometry: A robust tool for the analysis of
   intermolecular interactions"
   Advisor: Professor Robert A. Flowers II

B.S., Biochemistry, Lehigh University, Bethlehem, PA (GPA 3.77/4.00)   2005
   The American Institute of Chemists Foundation Award
   Robert F. Wolfe '40 Academic Scholarship, Lehigh University, 2004-2005

Wake Forest University, Winston-Salem, NC (GPA 3.60/4.00)   2001 – 2003
   Academic Grant, Wake Forest University, 2001-2003

RESEARCH EXPERIENCE

Graduate Research   2005 – 2011
Department of Chemistry, Lehigh University

- Launched collaborative project with Vanderbilt University to enhance development
  of back-scattering interferometer (BSI) instrumentation

- Built group's interferometer and validated results with isothermal titration
  calorimetry (ITC)

- Analyzed and quantified intermolecular interactions involving several biochemical
  and organic systems, including various protein interactions, hydrogen bonding of
  small molecules, and other systems

- Investigated impact of surface-immobilization on oligonucleotide hybridization to
  quantify a perturbation of nearly 50% due to surface tethering

- Extended applications of BSI to include DNA mismatched base pair detection and
  interactions in non-aqueous media

Undergraduate Research   2004 – 2005
Department of Chemistry, Lehigh University

- Developed reaction protocol to synthesize Samarium reductants using sonochemistry, reducing synthesis time from hours to minutes

- Enhanced yield and procedure to synthesize Samarium Diiodide in several solvents

Undergraduate Research   2002 – 2003
Department of Chemistry, Wake Forest University

- Utilized microwave technology to enhance slow reactions of activated benzene rings

TEACHING EXPERIENCE

Guest Lecture, Lehigh University   Spring 2011

- Presented a literature review of RNAi for lecture in Medicinal & Pharmaceutical Chemistry

Teaching Assistant, Lehigh University   2005 – 2011

- Assisted in laboratory sessions, tutored, and engaged undergraduate students in Organic Chemistry I & II and General Chemistry II

Teacher Development Program, Lehigh University   2008 – 2009

- Learned tools and expanded my knowledge on becoming an effective teacher and mentor

SKILLS

Laboratory Techniques: ITC, BSI, UV-VIS Spectroscopy, Fluorescence Spectroscopy, Fluorescence Microscopy, Column Chromatography, GC, GC/MS, NMR, Liquid Prism Ellipsometry

Computer: Origin, GraphPad Prism, ChemDraw, MS-Word/Excel/Powerpoint

PUBLICATIONS

1) **E. N. Pesciotta**, D. J. Bornhop, R. A. Flowers II, "Back-scattering interferometry: A versatile platform for the study of free-solution vs. surface-immobilized hybridization" *Chemistry-an Asian Journal*, 6, 70-73, (2011).

2) **E. N. Pesciotta**, D. J. Bornhop, R. A. Flowers II, "Back-scattering interferometry: an alternative approach for the study of hydrogen bonding interactions in organic solvents" *Organic Letters*, manuscript in press.

3) J. A. Teprovich, P. K. S. Antharjanam, P. Edamana, **E. N. Pesciotta**, R. A. Flowers II, "Generation of Sm-II reductants using high intensity ultrasound" *European Journal of Inorganic Chemistry*, 32, 5015-5019, (2008).

PATENT APPLICATIONS

R. A. Flowers II, D. J. Bornhop, **E. N. Pesciotta** "Methods, systems, and compositions for DNA analysis and sequence mismatch detection using back-scattering interferometry", U.S. Patent Application No. 61392890, October 2010.

D. J. Bornhop, R. A. Flowers II, **E. N. Pesciotta** "Nonaqueous backscattering interferometric methods" US Patent Application, February 2011.

PRESENTATIONS

E. N. Pesciotta, D. J. Bornhop, R. A. Flowers II "Comparison of free-solution DNA hybridization using isothermal titration calorimetry and back-scattering Interferometry" 237th ACS National Meeting, Salt Lake City, UT, March 2009.

E. N. Pesciotta "Sonochemical synthesis of Samarium reductants" Invited presentation for research master class with Nobel laureate Alan Heeger, Lehigh University, April 2005.

AFFILIATIONS

American Chemical Society